Integrated dynamical models of down-the-hole percussive drilling

A DISSERTATION SUBMITTED TO

THE FACULTY OF THE GRADUATE SCHOOL
OF THE UNIVERSITY OF MINNESOTA

AND TO

THE FACULTÉ DES SCIENCES APPLIQUÉES
OF THE UNIVERSITÉ DE LIÈGE
BY

Alexandre F.B.E. Depouhon

IN PARTIAL FULFILLMENT OF THE REQUIREMENTS
FOR THE DEGREES OF

Doctor of Philosophy (Civil Engineering)
Doctor in Applied Sciences

Co-advisers
Vincent Denoël, Emmanuel Detournay

July, 2014

Examining committee

Prof. Vincent DENOËL (Co-adviser)
Université de Liège, University of Minnesota

Prof. Emmanuel DETOURNAY (Co-adviser)
University of Minnesota

Prof. Bojan GUZINA
University of Minnesota

Prof. Mihailo JOVANOVIC
University of Minnesota

Prof. Ludovic NOELS
Université de Liège

Prof. Jean-Philippe PONTHOT (President)
Université de Liège

Prof. Nathan van de WOUW
Technische Universiteit Eindhoven

Acknowledgements

Let me start this note by thanking the funding authorities that have made this work possible (in alphabetical order): CSIRO, Itasca Consulting Group, Université de Liège, University of Minnesota.

Then continue by acknowledging the members of the examining committee that, as they read these letters, are about to dive in this manuscript, unless they have started by reading the conclusions. Hopefully, they and you, the reader, will come to appreciate these underground matters that are, yet, far from being solved. The deeper you dig, the more question marks you find.

Of importance were my encounters with Dr. Markku Keskiniva (Sandvik Mining and Construction) and Jaime Aros (DrillCo Tools) who introduced me to the industrial aspects of percussive drilling and brought me to the field. I would like to thank them for their warm and caring welcome.

This is also the place for an address to my supporting (co-)advisers: the Gurus. Beyond shaping me as a person and as a researcher, you have given me complete liberty and freedom as to the conduct of this thesis. This has enabled me to attend to my needing ones when the intricate path of life requested an absolute change of direction. I value this very much and thank you for that.

Even though most of this thesis was remotely conducted, interactions with the clans at ULg and UMN were always good. Surely, our friendship will remain intact throughout the years.

Special thanks go to the proofreading team that had to work against the clock.

As a final note, I would like to thank my parents and my beloved one for their dedicated support, especially during the final month of the thesis.

The Farm Boy is gone, replaced by Papa.

Abstract

Due to the overall process complexity, studies about percussive drilling usually focus on a limited set of the (sub)processes underlying it, *e.g.*, the hammer thermodynamics or the interaction between the bit and the rock. Following this paradigm, the assessment of the process performance is typically performed by considering a single percussive activation and a single interaction cycle between the bit and the rock, from arbitrary initial conditions.

The need for an integrated approach to evaluate drilling performance, based on the dynamical interaction of the (sub)processes underlying drilling, is evident. Such an approach requires simplified models, however, as the computational cost associated with full scale models is simply unbearable.

In this thesis, three dynamical integrated models are proposed and a preliminary analysis is conducted for a reference configuration and around it. The models couple three modules that represent: (*i*) the dynamics of the mechanical system, (*ii*) the interaction between the bit and the rock, and (*iii*) the activation of the mechanical system. For each module, simple representations are considered; of particular importance is the bit/rock interaction model which is a generalization to repeated interactions of experimental evidence observed for a single interaction.

In the first model, the dynamics of a rigid bit is cast into a drifting oscillator and the activation modeled as a periodic impulsive force. The second and third models account for the dynamics of the piston and the activation results from the impact of the piston on the bit. They are respectively based on elastic and rigid representations of the two bodies. In the rigid model, analytical results of wave propagation in thin rods are used to represent the contact interaction between the piston and the bit. In the elastic model, wave propagation is resolved.

Their preliminary analysis has revealed the occurrence of complex dynamical responses in the space of parameters. Expected trends are recovered around a reference configuration corresponding to a low-size hammer, with an increase of the rate of penetration with the feed force and the percussive frequency. An important sensitivity of the rate of penetration to the latter parameter is uncovered. Interestingly, our analyses

show that when the activation period has the same order of magnitude as the timescale associated with the bit/rock interaction, a lower power consumption is observed, indicating a possible resonance phenomenon in the drilling system. Also, the predictions of the rigid model are shown to be in good agreement with the ones of the elastic model, in the explored range of parameters.

Given the piecewise linear nature of the proposed models, dedicated numerical tools have been developed to conduct their analysis. As such, the thesis proposes a high-order time integration scheme for linear structural dynamics as well as a novel framework to evaluate the accuracy of such schemes, and a root-solving module to perform event-detection, for coupling with event-driven integration strategies. Specific to the framework is the account for both structural damping and external forcing in the evaluation of the scheme order of accuracy. Specific to the root-solving module is the forcing of event occurrence in the localization procedure.

Résumé

Devant l'importante complexité du processus de forage à percussion, les études s'y rapportant considèrent généralement un ensemble limité des (sous-)processus qui l'engendrent, *e.g.*, la thermodynamique du marteau ou encore l'interaction entre la roche et la tête de forage. Selon cette approche, l'évaluation de la performance du processus est typiquement réalisée en ne considérant qu'une seule activation percussive et une seule interaction à l'interface roche/outil, depuis des conditions initiales arbitrairement choisies.

Le besoin d'une approche intégrée pour l'évaluation de la performance du forage, basée sur les interactions dynamiques des sous-processus sous-jacents, est évident. Cependant, une telle approche nécessite des modèles simplifés car l'effort de calcul associé à des modèles complets rend l'approche difficile voire impossible.

Dans cette thèse, trois modèles dynamiques intrégrés sont proposés et une analyse préliminaire est réalisée, pour et autour d'une configuration de référence. Les modèles couplent trois modules qui représentent: (*i*) la dynamique du système mécanique, (*ii*) l'interaction entre la roche et la tête de forage, et (*iii*) l'activation du système mécanique. Pour chaque module, des représentations simples sont considérées; la généralisation à des interactions successives de la loi d'interaction entre la roche et la tête de forage, sur base de résultats expérimentaux relatifs à des interactions uniques, revêt une importance particulière.

Dans le premier modèle, la dynamique d'une tête de forage rigide est modélisée sous forme d'un oscillateur dérivant soumis à une activation impulsive et périodique. Dans les second et troisième modèles, la dynamique du piston est prise en compte et l'activation percussive est le résultat de sa collision avec la tête de forage. Ces deux modèles sont basés sur des représentations élastique et rigide des deux corps. Dans le modèle rigide, des résultats analytiques relatifs à la propagation d'onde dans les barres élancées sont utilisés pour représenter le contact entre le piston et la tête de forage. Dans le modèle élastique, la propagation d'onde est résolue.

L'analyse préliminaire des réponses à long terme des modèles a révélé l'existence de comportements dynamiques complexes dans l'espace des paramètres. Les tendances

attendues autour d'une configuration de référence correspondant à un marteau de petite taille sont prédites, notamment, une augmentation de la vitesse de pénétration moyenne lorsque la charge statique ou la fréquence d'activation sont augmentées. De manière intéressante, nos analyses montrent que lorsque la période d'activation est de l'ordre de l'échelle de temps associée à l'interaction roche/tête de forage, la puissance consommée par le forage est réduite; ceci indique un possible phénomène de résonance dans le système de forage. Elles montrent également une bonne corrélation entre les prédictions des modèles élastique et rigide, dans les gammes de paramètres qui ont été explorées.

Étant donné la nature linéaire par morceaux des modèles proposés, des outils numériques dédies ont été développés pour mener leur analyse. Ainsi, cette thèse propose également un schéma d'intégration haute précision et inconditionnellement stable pour application en dynamique des structures ainsi qu'un nouveau cadre pour l'analyse de la précision de tels schémas, et un module pour la détection d'événements requise par les stratégies d'intégration orientées événements. Le cadre proposé permet la prise en compte des termes d'amortissement stucturel et de chargement extérieur dans l'analyse de la précision du schéma d'intégration, tandis que le module de détection d'événements force leur réalisation durant le processus de localisation. Ces deux aspects sont novateurs.

Contents

List of Tables

List of Figures

Chapter 1

Introduction

"Make everything as simple as possible, but not simpler."

A. Einstein

1.1 Down-the-hole percussive drilling

Many industrial processes rely on the impulsive loading of a first body in contact with a second one to achieve the penetration of the former in the latter, *e.g.*, cutting and indentation. Among these, we find down-the-hole (DTH) percussive drilling, where penetration is achieved by the repeated application of a large impulsive force to a continuously rotating drill bit. Specific to this technology, which originates in the late 1940's with the first patent filed in 1952 by Belgian A. Stenuick [1], is the location of the hammer on top of the drill bit, as depicted in the sketch of Figure 1.1. The impulsive loading force is generated by the impact of a piston (hammer, typically pneumatically-operated but other technologies exist as well) on a shank adapter (anvil). The kinetic energy conveyed by the piston is transformed into compressive stress waves upon contact with the adapter, waves that propagate through the drill bit down to the rock, leading to the bit penetration by indentation, crushing, and chipping of the rock [2]. The fluid driving the piston is carried to the hammer inside the drill pipes and exhausted through the drill bit, enabling the flushing of the rock debris to the surface, through the annulus between the borehole wall and the drillstring.

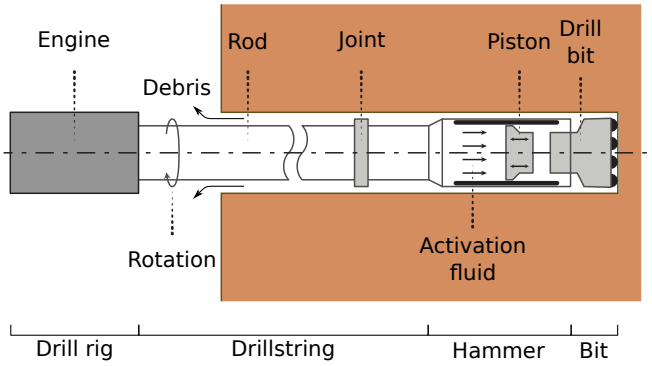

Figure 1.1: Schematic of a DTH percussive drilling system (not to scale).

Achieving higher rates of penetration and straighter holes than conventional rotary drilling in hard rock formations, the technology has found widespread usage in mining (exploration as well as drill-and-blast applications), water well and geothermal drilling, shallow oil and gas, and more [3]. Benefiting from the many improvements of the manufacturing industry and the gathering of know-how through experiments, mechanical designs have evolved significantly from their early-days ancestors to a maturity stage far ahead of today's theoretical understanding of the drilling process as a whole [4]. This knowledge lag is the consequence of the complicated physics underlying the process of drilling. It lies, indeed, at the confluence of several engineering disciplines such as mechanics of rock fragmentation, structural dynamics and thermodynamics, notably, and constitutes a significant modeling challenge, even with the current computational means.

A question that remains open to the scientific community is the identification of the root cause(s) of the experimentally-demonstrated existence of optimal control configurations when drilling (see Figure 1.2); that is, the existence of control parameter sets for which the average rate of penetration, the most important performance indicator, can be maximized. For a given DTH hammer, these parameters are the feed force (vertical force applied on top of the drillstring), the engine torque, and the activation fluid parameters, *e.g.*, the pressure of the air driving the piston. Such an optimal configuration is typically referred to as a *sweet spot*.

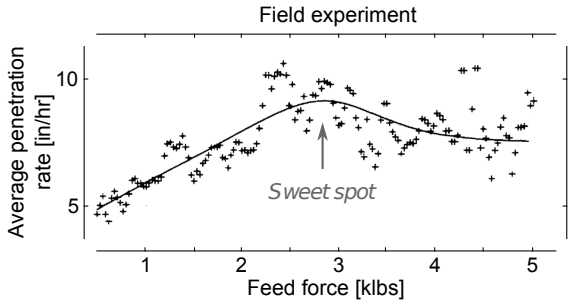

Figure 1.2: Existence of an optimal drilling configuration. Feed force influence on drilling performance (average rate of penetration). Experimental results from field measurements at Little Stobie Mine, Ontario, Canada. Adapted from Amjad [5].

In the remainder of the text, it is assumed that percussive drilling refers to DTH percussive drilling. The acronym DTH is dropped for legibility.

1.2 Integrated model

Percussive drilling can be interpreted as the interaction of several (sub)processes. From that perspective, it seems reasonable to model the drilling process in an integrated way, by coupling modules that govern the dynamics of the interacting (sub)processes. The choice of the modules and their complexity is where the art of the modeler comes into play.

In the present work, we have decided to model the drilling process as the interaction of three modules describing: (*i*) the interaction between the bit and the rock, (*ii*) the percussive activation and (*iii*) the axial dynamics of the mechanical system; see Figure 1.3. This choice is driven by our belief that these (sub)processes play a first-order role on the process dynamics and our desire to keep the model as simple as possible, with a limited number of degrees of freedom and parameters. Accordingly, the angular motion of the system as well as the flushing of the debris are not accounted for.

Following different sets of assumptions, three integrated models, with varying degrees of complexity, are proposed and analyzed in this thesis. A single degree of freedom oscillator interacting with a simplified representation of the penetration process, under a periodic impulsive activation, is first considered; it assumes that the bit behaves as

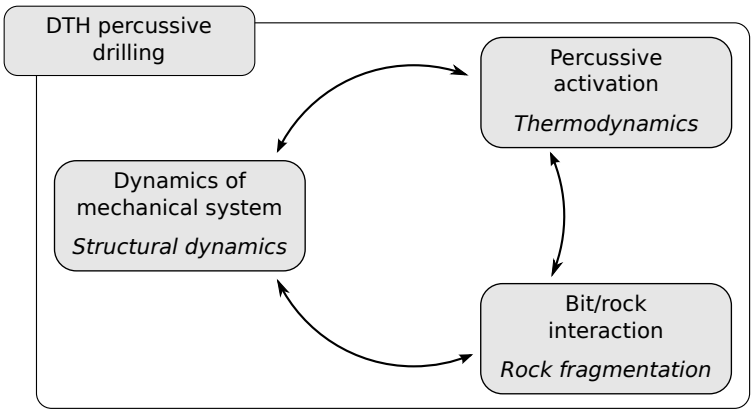

Figure 1.3: Integrated dynamical model of percussive drilling. The drilling process behavior results from the interaction of three (sub)processes, namely the dynamics of the mechanical system, the percussive activation and the bit/rock interaction.

a rigid body and that the percussive activation is independent of its motion. Then the assumption of periodic percussive activation is relaxed by resolving the piston dynamics, still using a simplified representation of the penetration process. Two models are proposed: an elastic one and a rigid one. The elastic model resolves all the timescales present in the process model and naturally accounts for the wave propagation in the mechanical system. The rigid model is based on an assumption of timescale separation between the bit motion and faster processes such as wave propagation. The piston/bit impacts are modeled by exploiting analytical wave propagation results. In that sense, the model can be seen as a multiscale formulation.

1.3 Literature review

Even though the integrated modeling of percussive drilling comes as an evidence, it has to be noted that, to the exception of [6], previous works focused on the (sub)processes; researchers addressed the modeling problem from the point of view of their field of expertise. This has provided valuable knowledge as to each of the studied (sub)processes underlying percussive drilling but not fulfilled the need for a proper process model. From that perspective, the present work is to be viewed as exploratory and is expected to serve as a stepping stone towards the advanced and consistent modeling of percussive drilling.

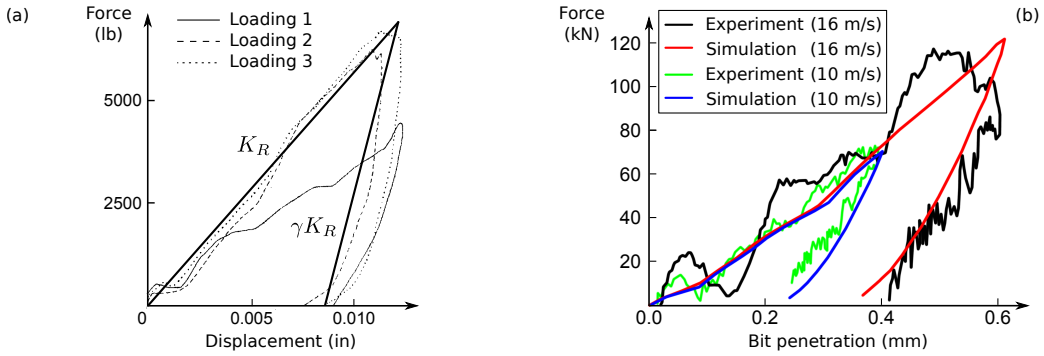

Figure 1.4: Dynamic indentation results, in Indiana limestone (a) and Kuru granite (b), confirm the bilinear characteristic of the force/penetration response and its limited rate-dependency. Adapted from [11] and [12], respectively.

We now provide a brief account of the results available in the literature, as these serve as the basis for the development of the integrated models that we propose.

The understanding of the mechanisms controlling bit penetration is key to modeling percussive drilling, particularly the interaction of the bit with the rock. Two groups, at the University of Minnesota and at the Luleå University of Technology, pioneered research in that direction. Experiments confirmed that penetration follows from a cascade of crushing and chipping phases [7]. They also revealed that the relation between the bit/rock interaction force and the bit penetration into the rock (referred to as force/penetration relation or bit/rock interaction law in the following) is not significantly dependent on the impact velocity of the indenter [8, 9]. Furthermore, this relation can be approximated by a bilinear model; that is, two stiffness parameters characterize the loading and unloading of the rock interface, with the unloading stiffness being larger than the loading one [10]. The bilinear trend is illustrated in Figure 1.4, which reproduces experimental and numerical results of dynamic indentation in Indiana limestone (plot (a), from [11]) and in Kuru granite (plot (b), from [12]).

These global observations—the force/penetration response is nothing else than a global representation of a local interaction process—have recently been confirmed by use of advanced numerical modeling, both at the single indenter/rock interaction level and at the bit/rock one; see Figure 1.5 and [13, 14, 15, 16], for instance.

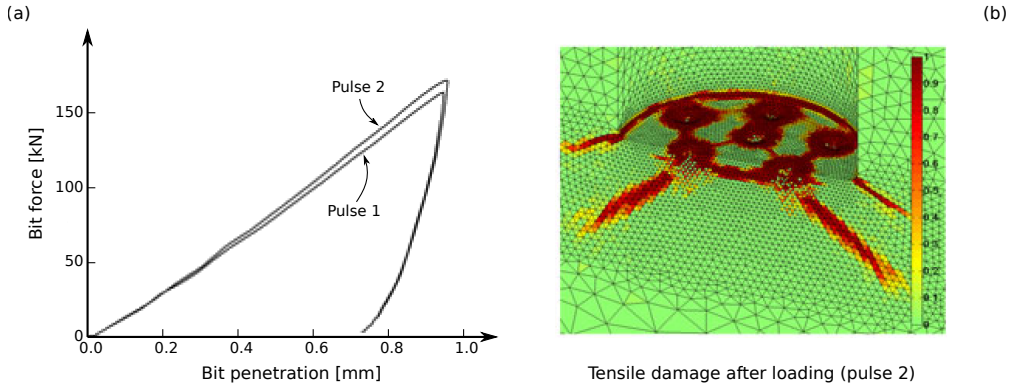

Figure 1.5: (a) – Prediction of the force/penetration characteristic corresponding to the impact of a rigid bit on heterogeneous rock; two loadings with identical impulse but different duration are considered. (b) – Representation of the damage ensuing the bit penetration in the rock medium. Adapted from [16].

Most works addressing drilling performance are concerned with the transfer of energy from the drilling system to the bit/rock interaction process for a single percussive activation; that is, how much penetration is achieved by a single blow. Several approaches have been followed in this perspective. In [2, 17, 18, 19], analytical expressions are derived on the basis of theoretical wave propagation considerations, and on assuming a bilinear bit/rock interaction model, as well as a closed bit/rock interface at the arrival of the incoming stress wave generated by the percussive activation. In these works, the shape of the stress pulse is arbitrarily chosen. Relaxation of these assumptions has been made by way of numerical analyses. The simulation approach proposed by Lundberg [20, 21] accounts for the geometries of the piston and bit which relaxes the arbitrariness of the incoming stress wave, while it also considers an initial gap at the bit/rock interface, similarly to the alternative impulse-momentum formulation proposed by Chiang and Elías [22]. Further generalizations were proposed in [23, 24, 25] to investigate the influence of 3D effects on drilling efficiency (they are negligible for DTH percussive drilling), the amount of evanescent energy elastically radiated in the rock massif during drilling (it is not significant), and the impact of 3D effects combined to an explicit modeling of the bit/rock interaction using finite elements (trends of 1D simulations are sufficient for design purposes), respectively. Despite the insight these results provide for a single percussive impact, it is a wonder to what extent they can

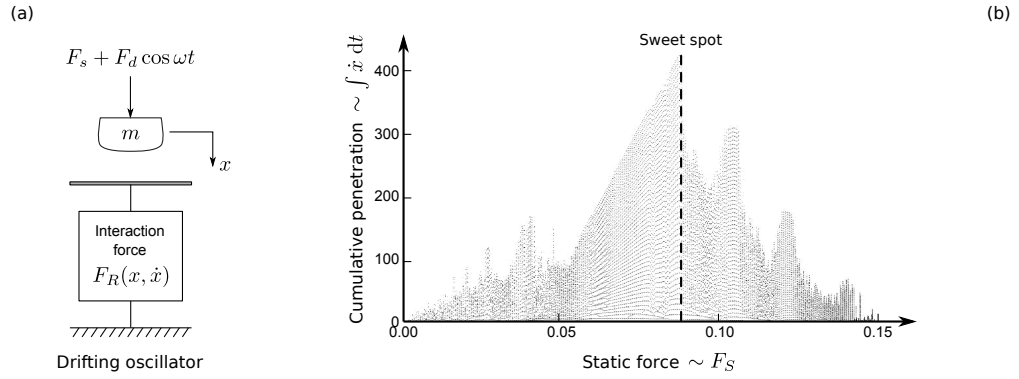

Figure 1.6: (a) – Drifting oscillator model. (b) – Existence of a sweet spot upon proper adjustment of the static load on the oscillator. Adapted from [26].

be extrapolated to the dynamical setting of successive percussive activations, for it is clear that the long-term response of the system might violate some of the assumptions behind these models, *e.g.*, the assumption of bit at rest on the rock does not hold when high percussive frequencies are considered.

Following a distinct approach, the group at the Centre for Applied Dynamics Research of the University of Aberdeen studied the dynamical response of drifting impact oscillators; that is, a single degree of freedom oscillator under external harmonic loading, in unilateral contact with a sliding interface representative of the bit/rock interaction. Two families of interface laws have been investigated, variations on the serial connection between a plastic slider and a viscoelastic cell [27, 28, 29, 30] and piecewise power laws that, in a sense, generalize the bilinear model on the basis of Hertz' contact theory [31]. Such systems have been demonstrated to experience periodic or chaotic motion, depending on their parametric configuration, and numerically reproduce the presence of a sweet spot in the parametric space; see the illustration in Figure 1.6. The direct applicability of these models to percussive drilling is, however, questionable. The first family of interface laws is not in line with the experimental evidence on bit/rock interaction; for instance, the model allows unbounded penetration under a static load above the slider threshold force. And, harmonic excitation is not representative of the impulsive loading generated by the percussive activation.

To overcome these limitations, we have proposed an alternative drifting oscillator

model [32]; it is based on a bilinear bit/rock interaction law, enriched with an energy barrier, and an impulsive rather than harmonic loading. The analyses have highlighted the existence of an optimal configuration as well, thereby hinting that the process dynamics might be the cause to the existence of an optimal drilling configuration. Furthermore, this suggests that drilling efficiency should be assessed by consideration of the long-term response of the dynamical process rather than by the analysis of energy transfer over a single activation.

On another aspect of the problem, Chiang and Stamm [33] developed a thermodynamical model describing the functioning of a pneumatic DTH hammer. On the basis of the representation of the piston/bit interaction by a coefficient of restitution to be experimentally or numerically determined, the model enables the calculation of the pressure force applied to the piston as a function of its motion and the fluid input/output parameters.

To our knowledge, the issue of cleaning, *i.e.*, the flushing of rock debris to the surface, and the account for the angular motion of the system have not been addressed in the scientific literature.

1.4 Penetration while drilling and generalized bit/rock interaction

The assessment of the long-term response of the drilling process requires the consideration of successive bit/rock interaction cycles; these are referred to as drilling cycles in the thesis. The explicit modeling of the interaction, for instance by use of finite elements and an advanced constitutive material model for the rock, enables the handling of such a situation. This, however, requires the introduction of many geometrical and material parameters, *e.g.*, the model of Saksala [16] counts 21 material parameters, and involves a computational cost far too important in regards to the previously stated constraints of simple and low dimensional model with a limited number of parameters.

One alternative is to go one scale up in the representation of the interaction and consider its force/penetration representation. The bilinear relationship that has been demonstrated to approximate well the interaction, both from experimental and numerical results, therefore has to be generalized to successive drilling cycles, for, in this case,

the penetration no longer equals the bit/rock interface displacement. This can be done by defining the conditions for the start of a new drilling cycle and a transformation law relating the interface displacement to the bit penetration.

In the absence of experimental data as to the expected interaction behavior for successive drilling cycles, an arbitrary choice has to be made to generalize the interaction law. This choice is of importance as the model responses will be conditioned by it. Several directions have been investigated. The one we propose is, we believe, that which limits the choice arbitrariness most.

Assuming that a new drilling cycle starts at the closure of the bit/rock interface or whenever the interface velocity changes sign during the unloading interaction phase, we define the penetration while drilling $p(t)$ as the following affine transformation of the interface position $u_R(t)$

$$p(t) := u_R(t) - u_{R,\ell} + \frac{F_{R,\ell}}{K_R}. \tag{1.1}$$

Variables $u_{R,\ell}$ and $F_{R,\ell}$ denote the position of the interface and the interaction force at the start of the drilling cycle, respectively; we refer to the starting point of the drilling cycle as the lower point along the drilling cycle, whence the index ℓ. These two variables are history variables; that is, they provide information as to the past status of the interface law. They are updated in a stepwise manner, at the beginning of each new drilling cycle. This implies that the penetration while drilling experiences a discontinuity at the start of a new drilling cycle. It is reset to zero or to a positive value depending on the interaction mode prior to the start of the new drilling cycle, to ensure the continuity of the interaction force. Similarly, we denote by indices p and u the history variables relative to the status of the interface law at peak penetration and at the upper location along the drilling cycles. Figure 1.7 illustrates the correspondence between the interface position and the penetration while drilling, on the basis of a bilinear representation of the interaction law. Points A, C^+ and F^+ define the lower characteristics of drilling cycles; the penetration is reset to zero at A, F^+ and to a positive value at C^+. Points B and E correspond to peak penetration while C, D and F do to upper locations along the drilling cycle.

As will be demonstrated in Section 2.5, the coupling of the bilinear law with the proposed definition of the penetration while drilling allows unbounded penetration under a static load. This rather unphysical behavior follows from the rate-independency of the

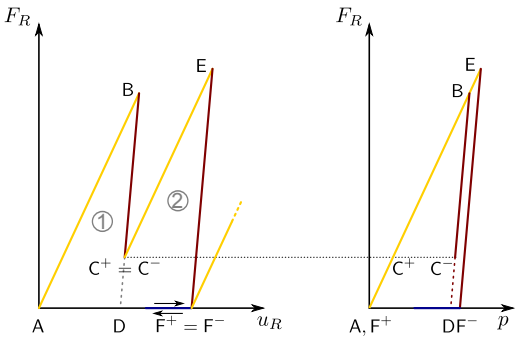

Figure 1.7: Correspondence between the penetration while drilling (left) and the bit/rock interface displacement (right), upon assumption of a bilinear representation of the bit/rock interaction.

bilinear law and the equal treatment of static and dynamic indentations. To dissociate these two types of interaction, we supplement the bilinear interaction law with an energy barrier; that is, a unilateral velocity-dependent dissipative component is added to the definition of the interaction law, as long as the work it has achieved over the current drilling cycle is below a given threshold and the interface is moving downwards: the energy barrier. This modeling addition to the interaction law can partly be justified by the necessity to account for dissipative processes evolving on faster timescales than that defined by the typical duration of a drilling cycle. An example of such a process is the energy elastically radiated in the rock medium following the impact of the bit on the rock surface.

Following this enrichment of the bilinear law, the interaction force F_R can be defined as a piecewise linear function of the penetration while drilling p, the penetration velocity $\dot{p} := \mathrm{d}p/\mathrm{d}t$, and a discrete parameter that we refer to as the drilling mode. It is given in Figure 1.8, with the conditions for drilling mode transition. Four distinct modes are to be considered: free flight (FF), dissipative forward contact (DFC), forward contact (FC) and backward contact (BC). Free flight corresponds to an open bit/rock interface; the force on bit is therefore zero, $F_R = 0$. The only possible mode transition is to dissipative forward contact; it takes place when the gap between the bit and the rock vanishes. At gap closure, a new drilling cycle is started and the penetration is reset to 0; the force on bit results from a stiffness and a viscous terms, $F_R = K_R p + C_R \dot{p}$. The interaction model remains in this mode until either the energy barrier is reached

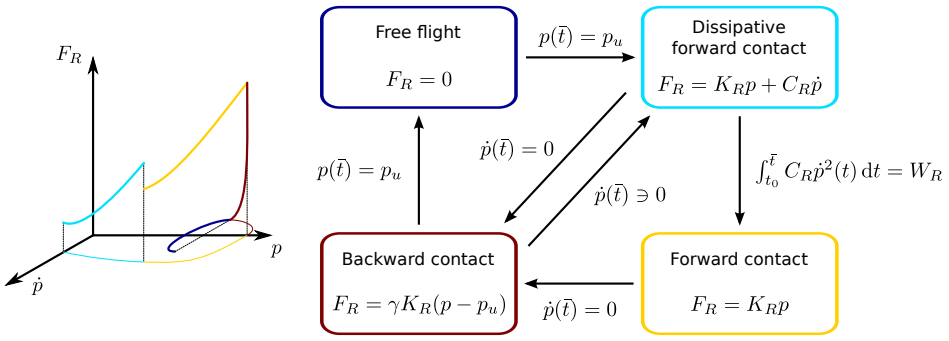

Figure 1.8: Definition of the generalized bit/rock interaction law. The instant of mode transition is generically represented by $\bar{t}$.

when the energy dissipated by the viscous force reaches threshold W_R, the model then switches to forward contact mode, or until the interface velocity vanishes before changing sign, then the model switches to backward contact. In the former case, the viscous term is dropped from the definition of the force on bit, $F_R = K_R p$; the forward contact mode is active until the interface velocity changes sign leading to a transition to backward contact mode. In backward contact mode, the interface moves upward and the force, $F_R = \gamma K_R (p - p_u)$, is defined by the unloading stiffness γK_R, with respect to the drilling cycle upper location $p_u := p_p(\gamma - 1)/\gamma$ defined at the mode transition. Two mode transitions are possible, to either free flight or dissipative forward contact, depending on which transition condition occurs first.

The generalized bit/rock interaction law that we have presented here is central to the three models we propose. Variations thereof are used, in accordance with the simplifying assumptions the drilling process models originate from.

1.5 Personal contributions

The position of this work as an initiative toward the integrated analysis of the process of percussive drilling makes it both exploratory and pioneering. Accordingly, research efforts were required in multiple directions so that well-posed models could be defined and the numerical tools for their analysis be developed. The most notable contributions of this thesis are:

- The generalization of the bilinear bit/rock interaction law to successive drilling cycles and the proposition of three models of percussive drilling based thereon [32, 34, 35].

- The extension of the concept of saltation matrix to systems with history variables [36].

- The proposition of a framework for the accuracy analysis of time integration schemes dedicated to linear structural dynamics. The framework accounts for both structural damping and external loading. It is applicable to systems with multiple degrees of freedom without any restriction on the form of linear damping [37].

- The establishment of a high-order 2-level unconditionally stable integration scheme to march second-order linear equations of motion in time [37].

- The development of a root-solving module to detect events along trajectories numerically computed by integration schemes dedicated to structural dynamics [38].

1.6 Thesis organization

Prior to the development of a full scale integrated model, a simplified model of the drilling process is proposed in Chapter 2. It is based on the reduction of the process model to a drifting oscillator representing a rigid bit. The percussive activation is modeled as a periodic impulsive force and the DFC mode collapsed in time in virtue of a timescale separation assumption. The analysis of the motion long-term response reveals the existence of complex dynamics with the coexistence of stable limit cycles and the existence of chaotic windows. Sweet spots are observed in restricted parameter ranges.

In Chapter 3, two models accounting for the piston dynamics are proposed. They are both based on the definition of a piecewise constant pressure force that drives the piston motion. The first model considers elastic bodies and resolves the wave propagation in the mechanical system that is reduced to one spatial dimension. A variation of the generalized bit/rock interaction introduced in Section 1.4 is used. Aiming at the event-driven integration of the piecewise-defined continuous model, a semi-discrete

formulation, relying on linear finite elements is proposed. Following this presentation, the elastic model is degenerated into a rigid body model, by invoking arguments of timescale separation. An analytical expression of the average post-activation velocities of the piston and the bit, obtained from wave propagation considerations is then used to represent the impact interaction between the two bodies. Scaling analyses are conducted for both models and the governing equations presented in dimensionless form.

Chapter 4 is dedicated to the presentation of the numerical tools that are used to analyze the elastic and rigid two-body models. The tools are developed on the generic basis of the piecewise-defined linear equation of motion and the associated event functions that govern its piecewise definition. Details about the time integration scheme and the root-solving module are given. A validation example based on the simplification of Newton's cradle dynamics is proposed. The mitigation of the spurious oscillations resulting from the numerical simulation of impacts in 1-dimensional systems is discussed as well.

A preliminary analysis of the response of the two-body models is conducted in Chapter 5 using the tools developed in Chapter 4. Emphasis is put on the analysis of the model response for a reference configuration and on the influence of some model parameters around that configuration. The analysis includes a comparison of the elastic and rigid model predictions. It appears that increasing the activation frequency is likely the most encouraging research direction for improving the average rate of penetration of the bit.

The main results of the thesis are summarized in Chapter 6 that concludes it. Directions for future investigations are provided as well. Given the important arbitrariness that gravitates around the proposed models, these definitely include validation works.

Appendix material is given as well to complete the main text. This includes additional developments on the drifting oscillator, the derivation of the reset map used in the rigid two-body model, the derivation of the integration scheme, the construction of the analytical solution to the Newton's cradle benchmark and the convergence analysis for the selection of the numerical parameters needed to integrate the two-body models.

Chapter 2

Drifting oscillator

"It never hurts to start by writing down the exact solution to the problem."

L.F. Greengard's axiom

As an introduction to the analysis of the dynamics of percussive drilling, we consider the simplest model that could represent the process: a single degree of freedom drifting oscillator. In this model, it is assumed that the bit behaves as a rigid body and that its motion can be decoupled from that of the piston. Also, it is hypothesized that the percussive activation and the dissipative forward contact mode (DFC) can be viewed as instantaneous as compared to the bit motion and its interaction with the rock (timescale separation). A standstill mode (SS), during which the bit is at rest, is introduced to handle situations where the bit has insufficient kinetic energy to overcome the energy barrier; this enables the discrimination between static and dynamic indentation.

The model and preliminary analysis results have been published in [32, 36].

2.1 Equation of motion

The free body diagram of the rigid bit is given in Figure 2.1. We denote the bit mass by M_b. Its vertical displacement u is positively defined in the downward direction. The static force and the impulsive loading representing the feed force and the percussive activation, respectively, are denoted by F_S and δF_{T_a}, and F_R refers to the bit/rock

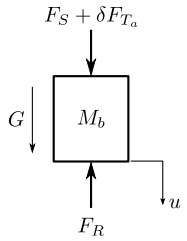

Figure 2.1: Free body diagram of the single degree of freedom drifting oscillator model.

interaction force. The latter is defined as a function of the penetration while drilling, $F_R = F_R(p)$, that itself is a function of the bit displacement, $p = p(u)$, according to its definition (1.1). The action of the gravity G is considered. The equation governing the bit dynamics is readily obtained by application of Newton's law

$$M_b \ddot{u} = M_b G + F_S + \delta F_{T_a} - F_R; \tag{2.1}$$

overhead dots are used as a shorthand notation for time differentiation, *i.e.*, $\dot{u} := \mathrm{d}u/\mathrm{d}t$.

The impulsive loading δF_{T_a}, representing the percussive activation, is chosen to be of period T_a and of constant impulse I at each pulse. It reads

$$\delta F_{T_a}(t) := I \sum_{i \in \mathbb{N}} \delta(t - iT_a - t_s), \tag{2.2}$$

with $\delta(\cdot)$ denoting Dirac delta function and $t_s \in [0, T_a)$ denoting the time shift of the percussive activation with respect to the origin of time; the set $\mathbb{N}$ represents that of natural numbers. The impulsive loading is thus zero but at specific time instants spaced by a duration T_a, at which it increases the momentum of the bit by a constant amount. The impulse I must be understood as an effective value for the momentum transferred from the piston to the bit during the percussive activation.

Accounting for the definition of the impulsive loading force, the equation of motion reduces to

$$M_b \ddot{u} = M_b G + F_S - F_R \tag{2.3}$$

everywhere but at the instants of impact, $t_i := iT_a + t_s$, at which the bit velocity experiences an instantaneous jump

$$\dot{u}(t_i^+) = \dot{u}(t_i^-) + \frac{I}{M_b}, \quad i \in \mathbb{N}. \tag{2.4}$$

Exponents + and − indicate the evaluation of the right and left limits of the function, *i.e.*, $u(t_i^{\pm}) := \lim_{\epsilon \downarrow 0} u(t_i \pm \epsilon)$. These are different for discontinuous variables. This notation convention is used throughout the thesis.

Under the assumption of timescale separation between fast and slow dynamics, the DFC drilling mode collapses in time, yielding an instantaneous application of the energy barrier. Accordingly, at the start of a drilling cycle, the bit velocity experiences a jump discontinuity; its magnitude is ruled by

$$\dot{p}_\ell^+ = \begin{cases} \sqrt{\left(\dot{p}_\ell^-\right)^2 - \left(\dot{p}_{\mathsf{SS}}\right)^2} & \text{if } \dot{p}_\ell^- > \dot{p}_{\mathsf{SS}}, \\ 0 & \text{otherwise,} \end{cases} \tag{2.5}$$

where $\dot{p}_\ell^-$ denotes the bit velocity at the start of the drilling cycle and $\dot{p}_{\mathsf{SS}} := \sqrt{2W_R/M_b}$ is the characteristic velocity associated with the energy barrier W_R. Thus, if the bit has insufficient kinetic energy at the start of a drilling cycle, its velocity instantaneously vanishes. To handle this complete loss of energy, the standstill (SS) mode is added to the definition of the interaction law. In this mode, the bit remains at rest until the next percussive activation, provided it is sufficiently large to overcome the energy barrier, *i.e.*, $I/M_b > \dot{p}_{\mathsf{SS}}$. In SS, static prevails ($\ddot{u} = 0$) and, threfeore, the interaction force compensates the bit weight and the feed force, $F_R = M_b G + F_S$. The other modes, namely, free flight (FF), forward contact (FC), backward contact (BC), are defined according to the text of Section 1.4.

Expanding the bit/rock interaction law for each mode, the equation of motion is recast in the following piecewise form

$$\begin{aligned} \mathsf{FC}: &\quad M_b\ddot{p} + K_R p = M_b G + F_S, \\ \mathsf{BC}: &\quad M_b\ddot{p} + \gamma K_R p = M_b G + F_S + \gamma K_R p_u, \\ \mathsf{FF}: &\quad M_b\ddot{p} = M_b G + F_S, \\ \mathsf{SS}: &\quad \ddot{p} = \dot{p} = 0. \end{aligned} \tag{2.6}$$

Transitions from one mode to the other are triggered by the occurrence of a transition condition that follows either from the regular motion of the bit or from the percussive activation; these are shown in Figure 2.2. The penetration is reset at the start of the FC and SS drilling modes. The upper penetration $p_u := p_p(\gamma - 1)/\gamma$ is updated at the

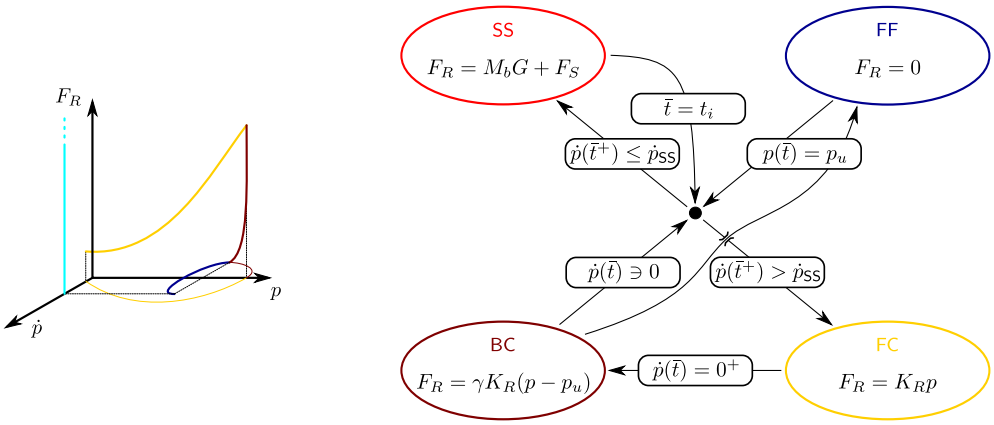

Figure 2.2: Definition of the generalized bit/rock interaction law for the drifting oscillator model. The instant of transition is generically denoted by $\bar{t}$; $\dot{p}_{\mathsf{SS}}$ denotes the velocity threshold associated with the energy barrier.

FC $\rightarrow$ BC drilling mode transition; its definition follows from the positiveness of the interaction force during the BC drilling mode.

2.2 Dimensionless formulation

To reduce the number of governing parameters, it is convenient to reformulate the model in dimensionless coordinates. Choosing the timescale proportional to the resonant period of the spring/mass system associated with the bit/rock interface at loading, and the reference length scale as the peak penetration resulting from the sole action of a percussive activation on a bit at rest and in contact with the rock, in the absence of energy barrier,

$$T := \sqrt{\frac{M_b}{K_R}}, \qquad L := \frac{I}{\sqrt{K_R M_b}}, \tag{2.7}$$

we define the dimensionless time and penetration while drilling

$$\tau := \frac{t}{T}, \qquad \mathcal{P} := \frac{p}{L}. \tag{2.8}$$

The piecewise-defined equation of motion immediately follows

$$\begin{aligned} \mathsf{FC}: &\quad \ddot{\mathcal{P}} + \mathcal{P} = \phi_S, \\ \mathsf{BC}: &\quad \ddot{\mathcal{P}} + \gamma\mathcal{P} = \phi_S + \gamma\mathcal{P}_u, \\ \mathsf{FF}: &\quad \ddot{\mathcal{P}} = \phi_S, \\ \mathsf{SS}: &\quad \ddot{\mathcal{P}} = \dot{\mathcal{P}} = 0, \end{aligned} \tag{2.9}$$

with

$$\phi_S := \frac{M_b G + F_S}{I}\sqrt{\frac{M_b}{K_R}} \tag{2.10}$$

and $\mathcal{P}_u := p_u/L$. The overhead dot now denotes differentiation with respect to the dimensionless time, $\dot{\mathcal{P}} := \mathrm{d}\mathcal{P}/\mathrm{d}\tau$. Following the choice of reference scales, the velocity jump ensuing the percussive activation at $\tau_i := t_i/T$ has unit magnitude, $[\![\dot{\mathcal{P}}_i]\!] := \dot{\mathcal{P}}(\tau_i^+) - \dot{\mathcal{P}}(\tau_i^-) = 1$. The scaled percussive activation parameters are referred to as $\tau_a := T_a/T$, $\tau_s := t_s/T$ and the threshold velocity relative to the energy barrier as

$$\dot{\mathcal{P}}_{SS} := \frac{T}{L}\dot{p}_{SS} = \sqrt{\frac{2W_R M_b}{I}}. \tag{2.11}$$

The possible mode transitions read

$$\begin{aligned} \mathsf{FF} \;\to\; \mathsf{FC}: &\quad \mathcal{P}(\bar{\tau}) = \mathcal{P}_u \;\&\; \dot{\mathcal{P}}(\bar{\tau}) > \dot{\mathcal{P}}_{\mathsf{SS}}, \\ \mathsf{FF} \;\to\; \mathsf{SS}: &\quad \mathcal{P}(\bar{\tau}) = \mathcal{P}_u \;\&\; \dot{\mathcal{P}}(\bar{\tau}) \le \dot{\mathcal{P}}_{\mathsf{SS}}, \\ \mathsf{FC} \;\to\; \mathsf{BC}: &\quad \dot{\mathcal{P}}(\bar{\tau}) = 0, \\ \mathsf{BC} \;\to\; \mathsf{FF}: &\quad \mathcal{P}(\bar{\tau}) = \mathcal{P}_u, \\ \mathsf{BC} \;\to\; \mathsf{FC}: &\quad \dot{\mathcal{P}}(\bar{\tau}^+)\cdot\dot{\mathcal{P}}(\bar{\tau}^-) < 0 \;\&\; \dot{\mathcal{P}}(\bar{\tau}^+) > \dot{\mathcal{P}}_{\mathsf{SS}}, \\ \mathsf{BC} \;\to\; \mathsf{SS}: &\quad \dot{\mathcal{P}}(\bar{\tau}) \ni 0 \;\&\; \dot{\mathcal{P}}(\bar{\tau}^+) \le \dot{\mathcal{P}}_{\mathsf{SS}}, \\ \mathsf{SS} \;\to\; \mathsf{FC}: &\quad \bar{\tau} = \tau_i \;\&\; \dot{\mathcal{P}}_{\mathsf{SS}} < 1. \end{aligned} \tag{2.12}$$

Percussive activations that do not lead to a change of the velocity sign do not trigger a change of drilling mode.

For the reference configuration given in Section 5.1, the reference scales value $T = 0.107$ ms and $L = 0.374$ mm. This yields the dimensionless parameters indicated in Table 2.1 that also lists their practical range.

Table 2.1: Typical ranges of the drifting oscillator dimensionless parameters.

Parameter	γ	ϕ_S	τ_a	$\dot{\mathcal{P}}_{\mathsf{SS}}$
Ref. cfg.	5	10^{-2}	400	$3 \cdot 10^{-2}$
Range	(1,∞)	$2.5 \cdot [10^{-4}, 10^{-2}]$	$[10^0, 10^3]$	(0,1)

2.3 Computation of the average rate of penetration

Of interest to us is the influence of the model parameters on the predicted average rate of penetration. It is defined by

$$\langle \dot{\mathcal{P}} \rangle_\tau := \frac{1}{T} \int_0^T \dot{\mathcal{P}}\,(\tau)\, d\tau, \tag{2.13}$$

where T is the duration of the averaging time window. If the long-term response is periodic, the time window is chosen equal to the period of the stationary solution $n\tau_a$; given the non-autonomous nature of the model (time enters the governing equations through the function defining the occurrence of percussive activation), the period multiplicity n is necessarily a positive integer [39]. If the long-term response is aperiodic, the averaging window should theoretically tend to infinity; however, for practical matters, we use $T = 100\tau_a$. In any case, the computation of the system trajectory is required.

Even though the equation of motion can be solved analytically for each drilling mode, the existence of a global closed-form solution seems illusive due to the complex switch patterns that take place during the motion of the bit. These analytical solutions can, nonetheless, be exploited in a semi-analytical event-driven integration procedure to robustly and efficiently march the equation of motion in time from a given set of initial conditions (these include the state variables, the drilling mode and the history variables required by the mode transition conditions active in the initial drilling mode). Such an integration strategy, most adapted to hybrid dynamical systems, *i.e.*, systems whose motion is governed by continuous-time and discrete-time dynamics [40], is described by Acary and Brogliato [41] on the basis of a three-stage strategy: (i) integrate the smooth vector field up to the next non-smooth event, (ii) accurately locate the time of this transition, and (iii) identify the next drilling mode and accordingly reinitialize the system at the event time.

With the availability of an integration procedure, the stationary solution can be computed via a shooting procedure [42, 43] that enforces a periodicity condition on the system trajectory in the phase plane; periodicity of the drilling mode must be verified *a posteriori*. The convergence of this procedure is contingent on two conditions, namely (*i*) the existence of a periodic response for the arbitrarily chosen limit cycle period and (*ii*) the choice of an initial guess in the basin of attraction of the iterative procedure. An example of periodic solution is analyzed in the next section. The embedding of the shooting algorithm in an arclength-parameterized continuation procedure [42, 43, 44] then enables the computation of solution branches upon variation of one of the model parameters, once the shooting procedure has been successfully initialized. Alongside the calculation of the periodic solution, its stability can be numerically assessed by computing the Floquet multipliers by use of finite differences [39, 43]. Specific care is then required to handle the non-smooth nature of the limit cycle; we have chosen to define its origin at the point of peak penetration, a point that belongs to any limit cycle and at which the fundamental solution matrix is continuous. Also, a consistent initialization of the history variables is required to ensure the non-violation of the causality embedded in these variables. Analytical developments, involving the calculation of the saltation matrices at the non-smooth points of the vector field [36, 39, 45, 46], have validated the correctness of these numerical procedures.

Despite its power, the continuation procedure (which was used to produce the results given in [32] and partly reported in Appendix A) proves fragile in practice, due to the numerical difficulties engendered by the non-smooth nature of the model, *e.g.*, discontinuities of the solution branches resulting from the non-commutativity of the periodic activation and the energy barrier. Also, the occurrence of chaos does not facilitate its use. Alternatively, we have used the stroboscopic Poincaré map to comprehend the influence the model parameters play on its long-term response. In this projection of the system dynamics, the state variables as well as the drilling mode are captured every activation period along the computed trajectory. Periodic trajectories are then characterized by a number of values (per variable) equal to the multiplicity n of the limit cycle period, which tends (theoretically) to infinity for aperiodic and chaotic solutions. Even though it fails at detecting coexisting stable attractors (convergence to a periodic solution is dependent on the chosen initial conditions), the Poincaré map still provides

a robust insight as to the influence of the model parameters on the type of response to be expected from the model, for a given parametric configuration. The results of the parametric analysis presented in Section 2.6 are based on the use of this map.

Details about the numerical procedures can be found in Appendix A.

2.4 Characterization of periodic solutions

Given the hybrid nature of the model, a complete solution is given by the bit trajectory plus the sequence of drilling modes the system has gone through along that trajectory. Two lighter but incomplete descriptors can, nonetheless, be used. We illustrate them on the basis of the period-1 stationary solution corresponding to the reference configuration given in Table 2.1, as computed by the shooting procedure. It is given in Figures 2.3-2.4 that show the time series of the penetration $\mathcal{P}$, the penetration rate $\dot{\mathcal{P}}$ and the interaction force ϕ_R over a period and at the end of the limit cycle; also, the phase portrait and the interaction law response in the penetration/force plane are represented. Color codes are used to represent the current drilling mode; they are identical to the ones used in the definition of the bit/rock interaction law in Figure 2.2. This color convention is used throughout the thesis.

The first descriptor is inspired by the works on impact oscillators by Peterka et al. [47, 48], who have introduced the notion of average number of impacts to characterize the periodic response of these systems. We define the average number of drilling cycles per loading period as the ratio m/n between the number of drilling cycles m and the period multiplicity n. This measure provides a rough idea of the phase portrait topology while incorporating the period multiplicity at the same time. For the example limit cycle, the ratio is given by $m/n = 5/1$.

The second descriptor is richer but less readable in the case of complex trajectories, *e.g.,* period-n stationary solutions, with $n > 1$. It corresponds to the explicit writing of the periodic sequence of drilling phases. Accounting for the inner-periodicity of the sequence, the periodic sequence of drilling modes for the example limit cycle reads $((\mathsf{FC} \rightarrow \mathsf{BC} \rightarrow \mathsf{FF})_5 \rightarrow \mathsf{SS} \rightarrow [\![\dot{\mathcal{P}}_i]\!])_{\circlearrowleft}$, where indices indicate a number of repetitions (5) or a periodicity condition ($\circlearrowleft$), and $[\![\dot{\mathcal{P}}_i]\!]$ denotes the occurrence of percussive activation. Although not complete, this descriptor provides a fair inspiration as to the qualitative

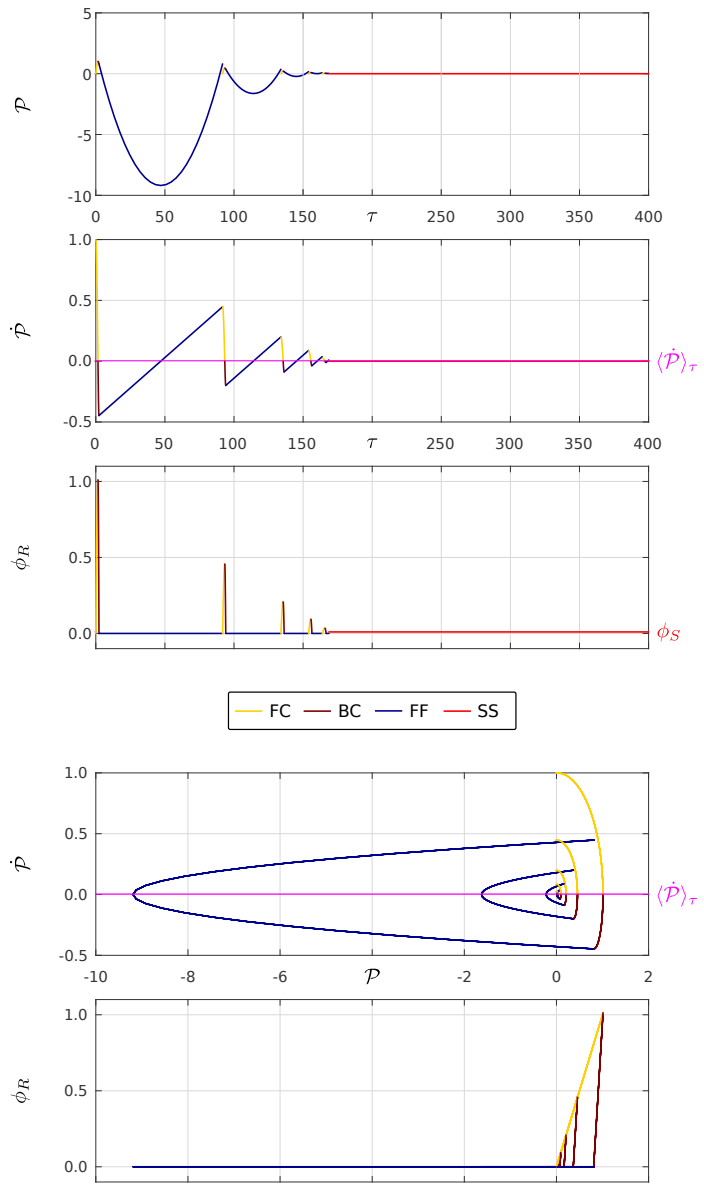

Figure 2.3: Period-1 ($n = 1$) limit cycle corresponding to the reference configuration, with five drilling cycles ($m = 5$) – Time series and projections into the phase plane and into the penetration/interaction force plane. The periodic sequence is given by $((\mathsf{FC} \to \mathsf{BC} \to \mathsf{FF})_5 \to \mathsf{SS} \to [\![\dot{\mathcal{P}}_i]\!])_{\circlearrowleft}$.

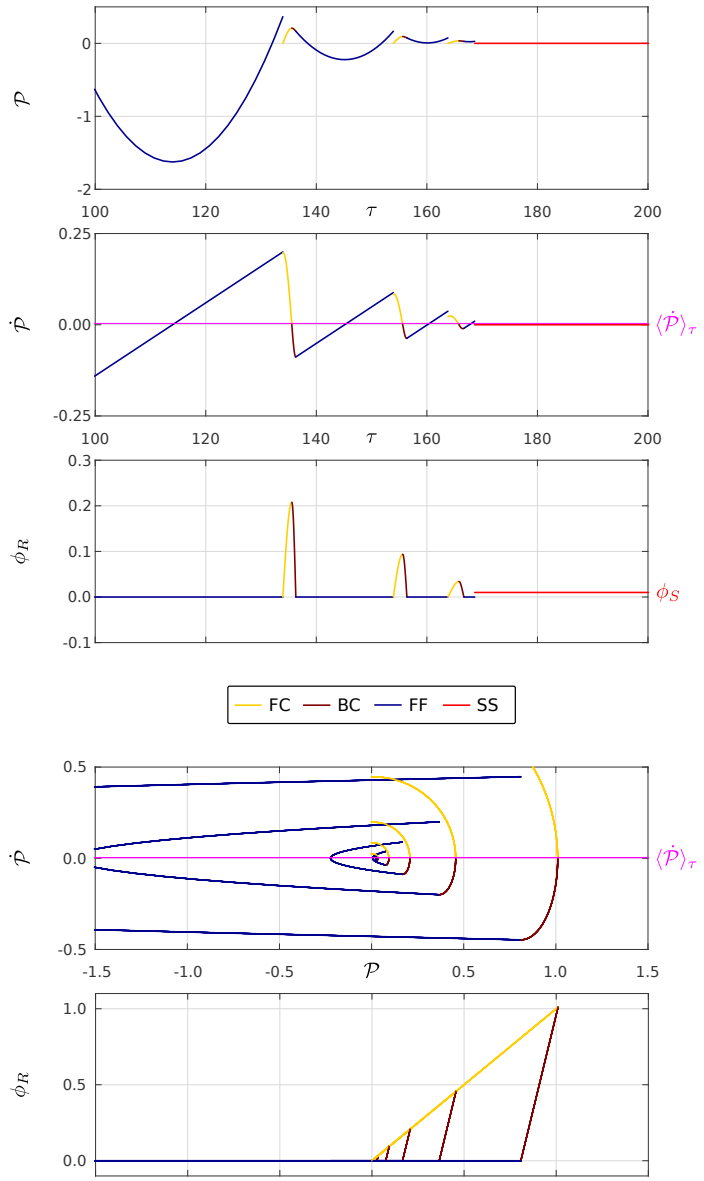

Figure 2.4: Period-1 ($n = 1$) limit cycle corresponding to the reference configuration, with five drilling cycles ($m = 5$) – Zoom on the time series and the projections into the phase plane and into the penetration/interaction force plane. The periodic sequence is given by $((\mathsf{FC} \to \mathsf{BC} \to \mathsf{FF})_5 \to \mathsf{SS} \to [\![\dot{\mathcal{P}}_i]\!])_{\circlearrowleft}$.

outline of the limit cycle phase portrait. It also enables the recovery of the first one ($m/n = 5/1$), as five $\mathsf{FC} \to \mathsf{BC}$ transitions and one velocity jump appear in the periodic sequence.

Beyond the illustration of these two descriptors, it is interesting to further consider Figures 2.3-2.4 and the qualitative behavior of the periodic trajectory. Even though the amplitude of the drilling cycles decreases monotonically, the periodic motion can be decomposed into two parts. The first one is the post-activation response that immediately follows from the impulsive loading of the bit. It consists of drilling cycles achieving an important penetration, followed by very large amplitude (negative penetration) free flight phases. Next, a second phase of motion takes place. It is the convergence to the standstill mode with drilling cycles of lower amplitude and free flight phases that tend to vanish following the decrease of the bit velocity at the exit of the drilling cycle (upper location). This motion pattern can mostly be explained by the energetic analysis of the drilling cycle.

2.5 Energetic analysis of the drilling cycle

In dimensionless coordinates, the bit/rock interaction model depends on two parameters, namely $\gamma \in (1, \infty)$ and $\dot{\mathcal{P}}_{\mathsf{SS}} \in (0, 1)$. They control the dissipation associated with the interaction law, on the slow (bit motion) and fast (instantaneous) timescales, respectively. Knowledge of their influence on the bit motion can be gained by analyzing the balance of the system mechanical energy over a drilling cycle, whose variation between two points along the bit trajectory reads

$$\frac{\dot{\mathcal{P}}_2^2}{2} - \frac{\dot{\mathcal{P}}_1^2}{2} = \phi_S(\mathcal{P}_2 - \mathcal{P}_1) - \mathcal{W}_R^{12}. \tag{2.14}$$

Variables indexed by 1 and 2 refer to these variables evaluated at arbitrarily chosen points 1 and 2 along the bit trajectory and $\mathcal{W}_R^{12}$ denotes the work done by the bit/rock interaction force along the path joining these two points.

To that end, we consider the drilling cycle resulting from the initiation of the system in the forward contact mode, with zero penetration and a kinetic energy sufficient to overcome the energy barrier, namely $\mathcal{P}_\ell = 0$ and $\dot{\mathcal{P}}_\ell > \dot{\mathcal{P}}_{\mathsf{SS}}$, in the absence of percussive

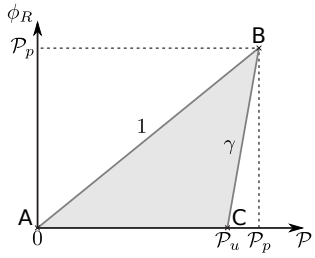

Figure 2.5: The energy dissipated by the penetration process, on the timescale of bit motion, is given by the area delimited by the drilling cycle in the dimensionless penetration/interaction force $(\mathcal{P}, \phi_R)$-space .

activation. The projection of the system trajectory into the dimensionless penetration/interaction force $(\mathcal{P}, \phi_R)$-space is then expected to follow the path ABC shown in Figure 2.5, *i.e.*, a sequence FC $\rightarrow$ BC of drilling modes. The work done by the interaction force being defined as the sum of the energetic components associated with the slow and fast timescales

$$\mathcal{W}_R(\mathcal{P}) := \int_0^{\mathcal{P}} \phi_R(\vartheta)\, \mathrm{d}\vartheta + \frac{\dot{\mathcal{P}}_{\mathsf{SS}}^2}{2}, \tag{2.15}$$

the energy consumed by the penetration process at peak and upper penetration is given by

$$\mathcal{W}_R(\mathcal{P}_p) = \frac{\mathcal{P}_p^2}{2} + \frac{\dot{\mathcal{P}}_{\mathsf{SS}}^2}{2}, \qquad\qquad \mathcal{W}_R(\mathcal{P}_u) = \frac{\mathcal{P}_p \mathcal{P}_u}{2} + \frac{\dot{\mathcal{P}}_{\mathsf{SS}}^2}{2}. \tag{2.16}$$

Combining these results with transition conditions (2.12) and the system balance of energy (2.14), the peak and upper penetrations can be related to the initial conditions via

$$\mathcal{P}_p = \phi_S + \sqrt{\phi_S^2 + \dot{\mathcal{P}}_\ell^2 - \dot{\mathcal{P}}_{\mathsf{SS}}^2}, \qquad \mathcal{P}_u = \frac{\gamma - 1}{\gamma}\left(\phi_S + \sqrt{\phi_S^2 + \dot{\mathcal{P}}_\ell^2 - \dot{\mathcal{P}}_{\mathsf{SS}}^2}\right), \tag{2.17}$$

as well as the upper (rebound) velocity that is given by

$$\dot{\mathcal{P}}_u = -\frac{1}{\sqrt{\gamma}}\sqrt{\dot{\mathcal{P}}_\ell^2 - \dot{\mathcal{P}}_{\mathsf{SS}}^2}. \tag{2.18}$$

These results are very instructive about the behavior of the system and provide a quantitative justification to the trajectory observed in Figures 2.3-2.4.

(i) Should the bit have a positive velocity $\dot{\mathcal{P}}_\ell > \dot{\mathcal{P}}_{\mathsf{SS}}$ at the beginning of a drilling cycle during which no percussive activation takes place, then it will necessarily exit the

drilling cycle with a negative velocity and enter a free flight phase, leading to the sequence of drilling modes ($\mathsf{FC} \to \mathsf{BC} \to \mathsf{FF}$).

(ii) The upper velocity $\dot{\mathcal{P}}_u$ has magnitude lower than and sign opposite to that of the lower velocity $\dot{\mathcal{P}}_\ell$. Given the conservative nature of the static load ϕ_S applied to the bit during the free flight mode, the lower velocity for the subsequent drilling cycle is equal, in magnitude, to the upper velocity of the current cycle. The drilling cycles and free flight phases following a percussive activation from standstill are thus expected to monotonically decrease in amplitude with respect to the number of completed drilling cycles. As the free flight duration also scales with the upper velocity, free flight phases shorten with the drilling cycle number and tend to vanish.

(iii) In the absence of percussive activation, the velocity at the start of drilling cycle $i > 1$ is given by

$$\dot{\mathcal{P}}_{\ell,i} = \sqrt{\frac{\dot{\mathcal{P}}_{\ell,1}^2}{\gamma^{i-1}} + (\gamma^{i-1} - 1)\,\epsilon^2}, \tag{2.19}$$

with $\epsilon := \dot{\mathcal{P}}_{\mathsf{SS}}/\sqrt{\gamma - 1}$. Using this result and the energetic condition at the start of a drilling cycle, the bit can be shown to experience a succession of m sequences of drilling modes $(\mathsf{FC} \to \mathsf{BC} \to \mathsf{FF})_m$ until the energy barrier is reached, with

$$m = \left\lceil \frac{\ln\left(\dot{\mathcal{P}}_\ell^2/\epsilon^2 + 1\right)}{\ln \gamma} \right\rceil - 1. \tag{2.20}$$

The brackets $\lceil \cdot \rceil$ denote the rounding operation to the nearest largest integer number. Setting $\dot{\mathcal{P}}_\ell = 1$, the lower velocity consequent to a percussive activation from the standstill mode, we recover $m = 5$, as observed in the example limit cycle of Figure 2.3.

(iv) Expanding equation (2.16), the work done by the interaction force along a drilling cycle is given by

$$\mathcal{W}_R(\mathcal{P}_u) = \frac{\gamma - 1}{2\gamma}\left(\phi_S + \sqrt{\phi_S^2 + \dot{\mathcal{P}}_\ell^2 - \dot{\mathcal{P}}_{\mathsf{SS}}^2}\right)^2 + \frac{\dot{\mathcal{P}}_{\mathsf{SS}}^2}{2}. \tag{2.21}$$

Provided $\dot{\mathcal{P}}_{\mathsf{SS}}$ is chosen independently of γ, we see that the energy consumed by a drilling cycle is virtually independent of parameter γ when it is large, as

$(\gamma - 1)/\gamma \sim 1$. This confirms that the model response is rather insensitive to unloading parameter γ at high values. In the particular case of a single percussive activation in the absence of a static load, $(\mathcal{P}_\ell, \dot{\mathcal{P}}_\ell, \phi_S) = (0, 1, 0)$, it simplifies to

$$\mathcal{W}_R(\mathcal{P}_u) = \frac{(1+\epsilon^2)(\gamma-1)}{2\gamma}. \tag{2.22}$$

(v) In the absence of an energy barrier ($\dot{\mathcal{P}}_{\mathsf{SS}} = 0$), the system experiences unbounded penetration under the sole action of the vertical dead load. Indeed, considering the application of the static loading from rest conditions $(\mathcal{P}_\ell, \dot{\mathcal{P}}_\ell) = (0, 0)$, the state upon completion of the drilling cycle reads $(\mathcal{P}_u, \dot{\mathcal{P}}_u) = (2\phi_S, 0)$; that is, the bit achieves finite penetration and exits the drilling cycle with zero velocity. Given the absence of an energy barrier, the transition $\mathsf{BC} \to \mathsf{FC}$ takes place and a new drilling cycle is initiated with identical initial conditions $(\mathcal{P}_\ell, \dot{\mathcal{P}}_\ell) = (0, 0)$. This scenario repeats indefinitely and the bit achieves unbounded cumulative penetration under a static load. The energy barrier, in making a distinction between static and dynamic indentations, prevents such unphysical behaviors.

(vi) In the limit $\gamma \to 1$ and for $\dot{\mathcal{P}}_{\mathsf{SS}} = 0$, the upper and lower velocities have the same magnitude but opposite sign. This is the translation of the conservative nature of the degenerated bit/rock interaction, for it becomes equivalent to a linear spring in unilateral contact with the bit. In the limit $\gamma \to 1$ and for $\dot{\mathcal{P}}_{\mathsf{SS}} > 0$, the system behaves similarly to a bouncing ball with finite duration dissipative contact phases [49]; indeed, the energy barrier dissipates energy at each closure of the interface yielding a rebound velocity with lower magnitude than the velocity at the closure of the interface. In either case, no penetration is achieved on average.

(vii) In the limit $\gamma \to \infty$, the rebound velocity vanishes whatever the magnitude of the initial velocity. This corresponds to a fully dissipative interaction law, *i.e.*, $(\mathcal{P}_u, \dot{\mathcal{P}}_u) = (\mathcal{P}_p, 0)$. The system motion is then given by $(\mathsf{FC} \to \mathsf{SS} \to [\![\dot{\mathcal{P}}_i]\!])_{\circlearrowleft}$ provided the activation period τ_a is longer than the duration of the forward contact phase. Backward contact and free flight phases become inaccessible. The average rate of penetration then reads

$$\langle \dot{\mathcal{P}} \rangle_\tau = \frac{\phi_S + \sqrt{\phi_S^2 + 1 - \dot{\mathcal{P}}_{\mathsf{SS}}^2}}{\tau_a}. \tag{2.23}$$

(viii) The standstill mode is an absorbant mode for the dynamical system. Two consequences follow.

(a) Any trajectory that enters a standstill mode is stuck in this mode until the next activation, provided it is sufficiently large to overcome the energy barrier. As such, the standstill mode acts as a reset of the system initial conditions to $(\mathcal{P}_\ell, \dot{\mathcal{P}}_\ell) = (0, 1)$ at the time of next activation.

(b) The zero vector field associated with the standstill phase leads to a zero fundamental solution matrix during that arc of trajectory. Accordingly, limit cycles containing a standstill phase are super-stable in the sense that both Floquet multipliers are zero, *i.e.*, the trajectory exactly returns on the limit cycle after one period provided perturbations do not preclude the presence of the standstill phase in the perturbed motion sequence.

2.6 Parametric analysis

To investigate the influence of the model parameters on the average rate of penetration, parametric analyses have been conducted around the reference configuration. Time integration of the equations of motion was carried over two hundred activation periods for each considered parametric configuration and the initial part of the response corresponding to hundred activation periods was discarded to minimize the influence of transients. Standstill initial conditions were considered and stroboscopic Poincaré maps constructed. They show the value of the state variables at the pre-activation instant τ_i^-; the color code associated with the bit/rock interaction law is used to represent the drilling mode at that time. Additionally, the evolution of the cumulative penetration or bit displacement is displayed, with each point corresponding to the pre-activation instant; these results have served as the basis to compute the average rate of penetration also shown.

Figure 2.6 illustrates the influence of the static force ϕ_S on the model response. It is seen that around the reference configuration, the presence of the standstill mode rules the dynamics of the system and drilling follows a period-1 stationary solution. As the parameter is decreased, the long-term motion of the dynamical system experiences

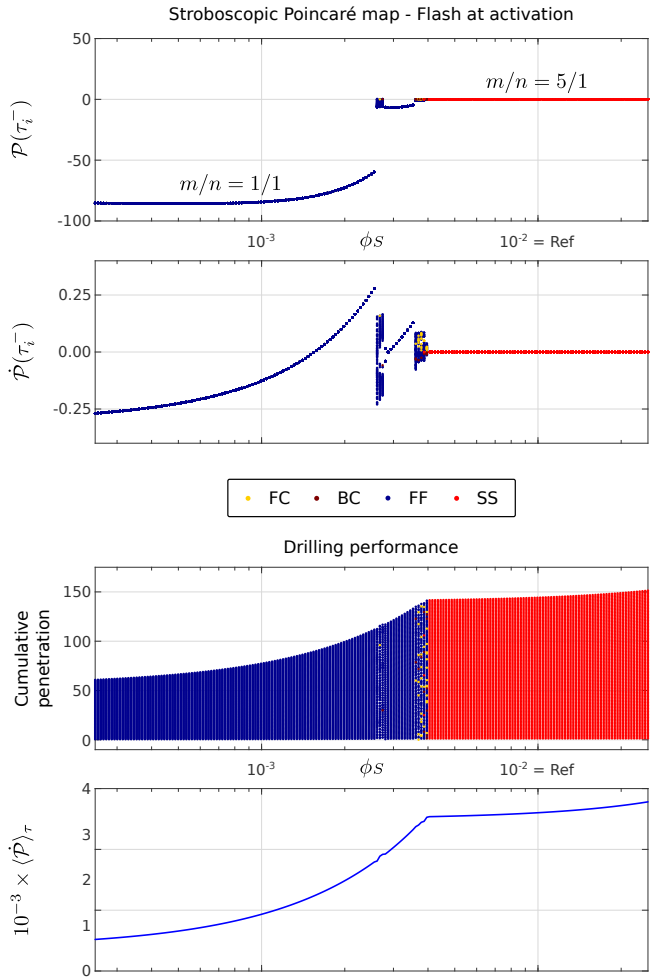

Figure 2.6: Influence of parameter ϕ_S (feed force) on the model response – Stroboscopic Poincaré map and drilling performance analysis. All other parameters correspond to the reference configuration.

a sequence of bifurcations and period-n, with $n > 1$, as well as aperiodic solutions become dominant. With further decrease of the parameter, the motion exits this window of complex behavior and a period-1 stationary motion is recovered; in this regime, the bit experiences large free flight phases as is witnessed by the negative value of the penetration at activation time. Through the sequence of bifurcations, the average number of drilling cycles is altered, with a direct consequence on the average rate of penetration. Its variation with the static force is linear on both sides of the angular point located at about $\phi_S = 4 \cdot 10^{-3}$; it is not properly reflected given the use of semilogarithmic axes.

The influence of parameter γ on the model response is shown in Figure 2.7. Starting from $\gamma = 1000$ towards decreasing values, it is seen that the period multiplicity of the stationary response remains equal to 1 until the occurrence of bifurcations around $\gamma = 3$. As expected, the penetration rate is little affected by its variations for large values of γ. Steps in the cumulative penetration and penetration rate correspond to the sudden increase of the number of drilling cycles m comprised by the periodic solution as γ is decreased. Interestingly, the penetration rate is seen to increase with the number of drilling cycles, to culminate at a maximum at the entry of the bifurcation zone around $\gamma = 3$. It then decreases monotonically towards zero as $\gamma \to 1$, as expected. The existence of rich dynamics at low γ is a direct consequence of the lower energy consumption of the interaction process, for this enables the interaction of the percussive activation with the system dynamics, as larger and longer free flight phases result from a low γ value. Although parameter γ is not, *per se*, a control parameter of the model, it can be influenced by the bit design. It is thus expected that a proper bit design can contribute toward the increase of the bit average rate of penetration.

For the reference configuration, the model predicts that the bit converges to standstill after the realization of five drilling cycles. As was mentioned in Section 2.5, the standstill mode is an absorbant mode for the system dynamics; fancy dynamics is thus not expected in the near parametric vicinity of the reference configuration as long as the stationary response exhibits that periodic sequence. One way to break it down is by reducing the period of the percussive activation τ_a. Figure 2.8 shows its influence on the model response. Decreasing it from $\tau_a = 1000$ toward $\tau_a = 1$, it is seen to first have a positive influence on the rate of penetration while not affecting the cumulative

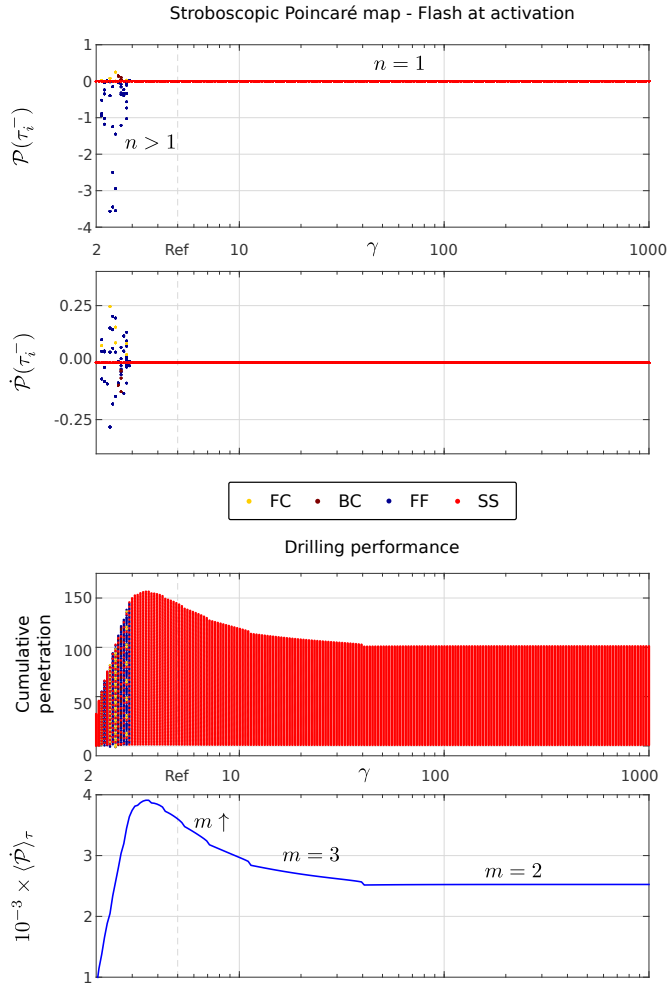

Figure 2.7: Influence of parameter γ (bit/rock interaction) on the model response – Stroboscopic Poincaré map and drilling performance analysis. All other parameters correspond to the reference configuration.

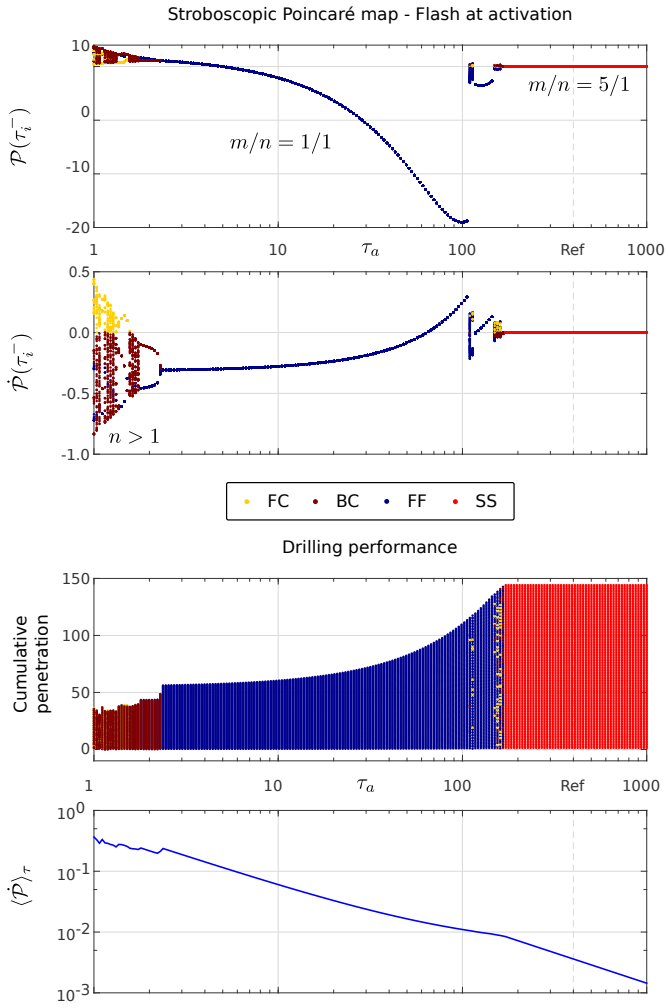

Figure 2.8: Influence of parameter τ_a (period of percussive activation) on the model response – Stroboscopic Poincaré map and drilling performance analysis. All other parameters correspond to the reference configuration.

penetration, as long as the system is in a $m/n = 5/1$ response similar to that of the reference configuration. This result is justified by the fact that once the bit is in the standstill mode, it remains in that mode until the next percussive activation; in such regime, the average rate of penetration is thus inversely proportional to the period of percussive activation. Through a bifurcation pattern similar to the one observed upon variation of the static force ϕ_S, see Figure 2.6 for $\phi_S = [20, 40]$, the stationary response takes a 1/1 form around $\tau_a = 100$. The average number of drilling cycles achieved by the stationary solution remains so until the period of the percussive activation becomes of the same order of magnitude as the duration of a drilling cycle; that is, $\tau_a = \mathcal{O}(1)$ given the scaling. Upon reaching that threshold, percussive activation fully couples with the bit/rock interaction; period-doubling bifurcations take place and windows of periodic solutions are observed in-between windows of aperiodic motion. Whereas constant time windows are used to compute the cumulative penetration in Figures 2.6-2.7, the one used in Figure 2.8 is proportional to τ_a. This proportionality more than compensates the decrease of the cumulative penetration with the increase of the percussive activation frequency τ_a^{-1}; indeed, the average rate of penetration is seen to, on average, increase with the activation frequency.

2.7 Concluding remarks

The drifting oscillator is probably the lowest dimensional model one could come with to represent the dynamics of percussive drilling. Although the hybrid nature of the model (partly due to the use of a realistic bit/rock interaction law) allows a rich spectrum of response types, *e.g.*, coexistence of limit cycles, chaotic behavior and clues of optimal drilling configurations, its single degree of freedom is synonymous of multiple shortcomings.

The principal one is the assumption of periodic percussive activation. As will become clear in the following chapters, the dynamics of the bit plays a significant influence on that of the piston through the interplay of waves propagating in the mechanical system. There are thus only a limited set of configurations for which the assumption would hold. Moreover, its verification in the conditions of the stationary response does not guarantee it would hold during the transient phase. Accordingly, the evaluation of parameter I

(the impulse delivered to the bit at each blow) from physical considerations is a tricky business rendering hypothetical the application of the model to a real drilling situation.

Richer models are thus required to represent the process.

Chapter 3

Two-body models

"A problem well put is half solved."

J. Dewey

The coupling of the bit/rock interaction model with a drifting oscillator has revealed some of the dynamical complexity and richness that can be expected from a model of the percussive drilling process. However, due to the oversimplified representation of the mechanical system in that model, its application to a physical device proves difficult, notably as regards the evaluation of the effective percussive activation impulse. A more advanced representation of the mechanical system is thus required.

In this chapter, we present two models of the percussive drilling process that are based on the reduction of the mechanical system to two bodies, namely the piston and the bit; see the illustration in Figure 3.1. The first model is based on the elastic representation of the two bodies. It resolves both the fast and slow timescale (sub)processes underlying the drilling process, in particular, the wave propagation in the mechanical

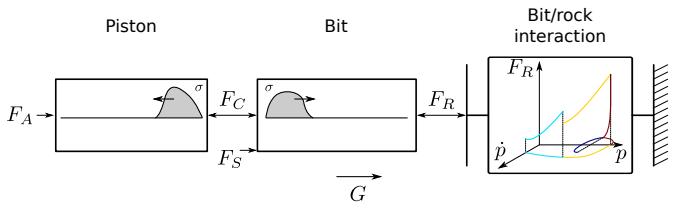

Figure 3.1: Simplified representation of the percussive drilling process.

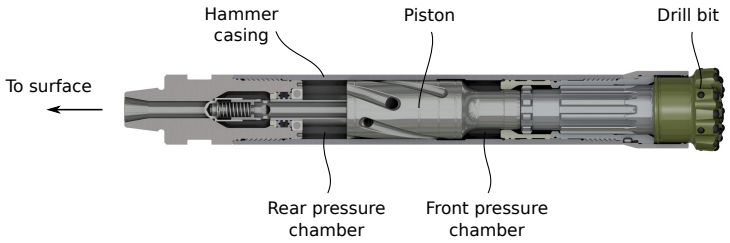

Figure 3.2: CAD drawing of the 8-in Impax down-the-hole hammer, manufactured by SMITH BITS [51].

system. The second is based on a multiscale formulation. The two bodies are considered rigid but their interaction during percussive activation is assessed, however, on the basis of wave propagation arguments, by use of analytical expressions for the post-impact velocities resulting from the longitudinal collinear impact of two elastic bars. In both models, a piecewise-constant pressure law is used to define the force driving the piston motion, and the bit/rock interaction law given in Section 1.4 serves as basis to a computational model.

3.1 Pressure force on the piston

Pneumatic DTH hammers usually comprise two pressure chambers that are alternatively fed with compressed air [50]; see Figure 3.2. In valveless systems, the access of the compressed air flow to either chamber follows from the piston motion, more specifically from its position relative to that of the hammer casing. The pressure force applied to the piston thus results from the thermodynamics of the air flow as ruled by the motion of the piston [33].

Rather than invoking a thermodynamical model that, at the price of complexity, would provide an accurate definition of the pressure force throughout the piston motion cycle, see [52, Fig. 3] for an example of pressure force, we have recourse to a simplified law, based on two parameters only, whose calibration guarantees the orders of magnitude of the percussive frequency, of the impact velocity, and of the piston maximal stroke. These are the only variables of interest, as our interest is focused on the piston/bit system motion. The law is based on the relative average motion of the piston/bit

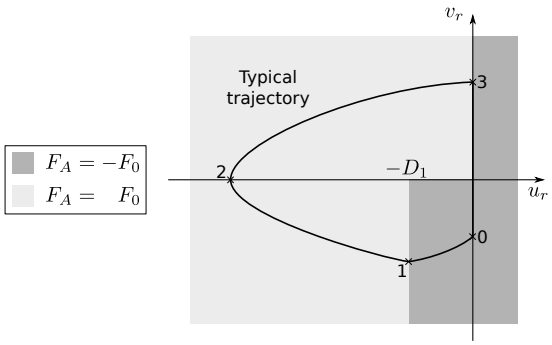

Figure 3.3: Piecewise-constant pressure model to represent the pneumatic driving of the piston as a function of the relative displacement and velocity between the piston and the bit, u_r, v_r.

system, that we denote by u_r, v_r; it is given by

$$F_A(u_r, v_r) = \begin{cases} F_0 & \text{if } (u_r, v_r) \in (-\infty, -D_1] \times \mathbb{R} \cup (-D_1, 0] \times \mathbb{R}^+, \\ -F_0 & \text{otherwise.} \end{cases} \tag{3.1}$$

Or in shorthand notation $F_A = \alpha F_0$ with discrete parameter $\alpha \in \{-1; 1\}$ defined in accordance with the piston relative motion.

Figure 3.3 summarizes the piecewise definition of the pressure law in the phase plane (u_r, v_r) and shows the typical trajectory that would follow a rigid piston in case the bit is at rest, *i.e.*, relative motion is absolute. Starting from point 0 with a negative velocity $v_{r,0}$, the pressure force is defined upwards and the piston accelerated in the same direction. Arrived at point 1, the direction of the pressure force switches to downwards; the piston experiences constant deceleration and its velocity is zero when it reaches point 2. At that point, it starts its descent toward the bit, which it collides upon reaching the contact interface at point 3. As soon as contact is established at the piston/bit interface, the pressure force direction is set to upwards.

Following the assumptions of rigid piston and bit at rest, the impact velocity at point 3, $v_{r,3}$, the maximal stroke at point 2, $-u_{r,2}$, and the piston free flight duration t_3

can be estimated as a function of the law parameters F_0, D_1; they read

$$\begin{aligned} v_{r,3} &= \sqrt{2\frac{F_0 D_1}{M_p}}\sqrt{2+\mu}, \\ -u_{r,2} &= D_1\,(2+\mu)\,, \\ t_3 &= \sqrt{2\frac{D_1 M_p}{F_0}}\left(\sqrt{2+\mu}+2\sqrt{1+\mu}-\sqrt{\mu}\right), \end{aligned} \tag{3.2}$$

where $\mu := M_p v_{r,0}^2/2F_0D_1$ is the ratio between the piston initial relative kinetic energy $M_p v_{r,0}^2/2$ and the energy provided to the piston over a pressure cycle $E_P := F_0D_1$. Therefore, given reference values for the piston mass M_p and the relative velocity $v_{r,0}$, parameters F_0, D_1 can be estimated by solving a constrained nonlinear algebraic problem that enforces equality constraints on variables $v_{r,3}, t_3$ and the inequalities $0 < D_1 < -u_{r,2}$. For the reference configuration detailed in Section 5.1, we have $M_p = 7555$ g. Setting $v_{r,3} = 8.5$ mm/ms, $v_{r,0} = -3$ mm/ms, $t_3 = 45$ ms ($\equiv 22.2$ Hz) and $-u_{r,2} = 100$ mm, we obtain $D_1 = 39$ mm and $F_0 = 3064$ N, which we round to $D_1 = 40$ mm and $F_0 = 3000$ N for the reference configuration. In addition, for this reference setting, $\mu = 0.284 = \mathcal{O}(10^{-1})$. Accordingly, equations (3.2) naturally reveal the scales intrinsic to the motion of the piston, namely

$$L_P := D_1, \qquad V_P := \sqrt{F_0 D_1/M_p}, \qquad T_P := \sqrt{D_1 M_p/F_0}, \tag{3.3}$$

for the dimensions of length, velocity and time, respectively.

Derivatives of the reference scales can be obtained by combining them. Two useful associated quantities are the reference power P_P and impulse I_P delivered by the pressure force. They follow from the multiplication of the reference velocity by the magnitude of the pressure force and the piston mass

$$P_P := \sqrt{\frac{F_0^3 D_1}{M_p}}, \qquad I_P := \sqrt{F_0 D_1 M_p}. \tag{3.4}$$

The former expression will be used to assess the influence of the percussive frequency on the model response while enforcing the theoretical constancy of the delivered power, *i.e.*, enforcing $F_0^3 D_1 = F_0^3 D_1\big|_{\mathsf{Ref}}$, and the latter can serve to evaluate the impulse parameter I of the drifting oscillator model.

3.2 Elastic model

3.2.1 Equations of motion

In the elastic model we propose, the motion of each body is governed by the scalar wave equation that expresses the balance of linear momentum of an infinitesimal slice of material [53, 54]. This choice is justified by:

- the reduction of the piston and the bit to 1D bodies, an approximation justified by their slenderness and concurring with analyses showing the limited 3D effects on the response of percussive drilling systems [23, 25];
- the restriction of the problem to the linear elastic setting;
- the restriction of motion to the axial direction which prevents any complication due to large displacements as there are no rotations;
- the restriction to particle velocities that are well below the wave propagation speed so that shocks do not occur; in percussive drilling, typical piston/bit relative impact velocities are of the order of 10 m/s as compared to the 5000 m/s of the wave propagation speed in steel.

Let $O\boldsymbol{e}_x$ be the global axis system with respect to which positions and displacements are measured and $O_i\boldsymbol{e}_i, i \in \{p; b\}$, be local axis systems moving with the top surface of the piston (subscript p) and the bit (subscript b), respectively. Following these definitions, the position of a material point $x_i(X_i, t)$ in the global axis system, at time t, can be expressed as the sum of the position of the local axis system origin $x_{i,0}$ at the origin of time, its associated Lagrangian coordinate $X_i \in [0, L_i]$, and the displacement $u_i(X_i, t)$

$$x_i(X_i, t) = x_{i,0} + X_i + u_i(X_i, t); \tag{3.5}$$

obviously, this relationship verifies

$$x_i(X_i, 0) = x_{i,0} + X_i, \tag{3.6}$$

since it is implicitly assumed that $u_i(X_i, 0) = 0$.

Under this notation, the generic wave equation ruling the motion of the piston and the bit reads

$$\rho A \frac{\partial^2 u_i}{\partial t^2}(X_i, t) = EA \frac{\partial^2 u_i}{\partial X_i^2}(X_i, t) + \rho A f_i. \tag{3.7}$$

Dimensional parameters ρ, E refer to the steel density and Young's modulus; the cross section of the cylinders is denoted by A, and the external body forcing term by f_i, which depends on the considered body. Coupling between the motion of each body, as well as with the hole bottom, enters the equations of motion through the boundary conditions.

Specializing to the piston, the boundary conditions at the top and bottom ends are given by

$$\frac{\partial u_p}{\partial X_p}(0, t) = 0, \qquad 0 \leq -\frac{\partial u_p}{\partial X_p}(L_p, t) \perp g(t) \geq 0, \tag{3.8}$$

where the complementarity condition expresses the Signorini condition [55] at the contact interface. Either it is open with a positive gap function, the distance between the piston bottom end and the bit top end,

$$\begin{aligned} g(t) &= x_b(0, t) - x_p(L_p, t), \\ &= g_0 + u_b(0, t) - u_p(L_p, t), \end{aligned} \tag{3.9}$$

with g_0 denoting the the initial gap, and a zero contact stress $E\partial u_p/\partial X_p(L_p, t) = 0$. Or it is closed with a zero gap function $g(t) = 0$ and a compressive contact stress $E\partial u_p/\partial X_p(L_p, t) \leq 0$. The body force includes the action of gravity G and that of the pressure force F_A that we choose to apply as a body force so as to not generate spurious wave fronts through its piecewise constant definition

$$f_p = G + \frac{F_A}{\rho A L_p}. \tag{3.10}$$

As to the bit, its boundary conditions read

$$0 \leq -\frac{\partial u_b}{\partial X_b}(0, t) \perp g(t) \geq 0, \qquad -EA \frac{\partial u_b}{\partial X_b}(L_b, t) = F_R, \tag{3.11}$$

where F_R denotes the bit/rock interaction force. Its definition, a variant of that given in Section 1.4, is deferred to a subsequent section. The body force includes gravity and the feed force applied from the surface F_S that we also define as a body force to prevent spurious wave fronts which would result from its application at a single point

$$f_b = G + \frac{F_S}{\rho A L_b}. \tag{3.12}$$

3.2.2 Scaling

The governing equations introduced heretofore depend on a number of dimensional parameters. Table 3.1 lists these 20 variables plus the 2 dependent fields, as well as their generic units. According to the Π-theorem [56], the set of governing parameters can be reduced to at most 17 variables provided the equations are reformulated with dimensionless quantities.

To that end, it is interesting to address the problem from a timescale perspective by introducing reference scales representative of the dynamics of the (sub)processes. The first two timescales are associated with the wave propagation in the bit and the piston; they are given by the wave travel times in each body

$$T_1 := \frac{L_p}{c_0}, \qquad T_2 := \frac{L_b}{c_0}, \tag{3.13}$$

where $c_0 := \sqrt{E/\rho}$ is the wave propagation speed in the material. Second, we consider the pressure law. Based on its analysis, a third timescale, approximating the piston free flight time, is given as

$$T_3 := \sqrt{\frac{D_1 M_p}{F_0}}, \tag{3.14}$$

where $M_p := \rho A L_p$ denotes the piston mass. Then, on the basis of rigid body motion considerations, which hold for configurations with $K_R L_b/EA \ll 1$ (see [17]), we introduce a timescale representative of the duration of a drilling cycle

$$T_4 := \sqrt{\frac{M_b}{K_R}}, \tag{3.15}$$

where $M_b := \rho A L_b$ refers to the bit mass. This timescale is the one that enters the scaling of the drifting oscillator model. A fifth timescale associated with the energy barrier is then defined. Assuming the bit velocity to be constant and equal to $V_P = \sqrt{F_0 D_1/M_p}$, the integral condition defining the energy barrier can be solved for its upper boundary, yielding

$$T_5 := \frac{W_R}{F_0 D_1}\frac{M_p}{C_R}. \tag{3.16}$$

This approximation only holds for the drilling cycle ensuing a percussive activation; indeed, the lower bit velocity in subsequent drilling cycles induces a larger duration of the DFC phase. It can be used to define the values of the energy barrier parameters

C_R, W_R. In particular, the constraints $\omega_{54} := T_5/T_4 \ll 1, \varrho := W_R/F_0D_1 \ll 1$ must be enforced to reflect the faster and lower energy nature of the processes embedded in the energy barrier. Here and in the sequel, timescale ratios are denoted by $\omega_{ij} := T_i/T_j$. Typical orders of magnitude for the timescales read (in milliseconds)

$$T_1 = \mathcal{O}(10^{-2}), \quad T_2 = \mathcal{O}(10^{-2}), \quad T_3 = \mathcal{O}(10), \quad T_4 = \mathcal{O}(10^{-1}), \quad T_5 = \mathcal{O}(10^{-4}). \tag{3.17}$$

These clearly emphasize the multiscale nature of the problem, as five orders of magnitude are spanned by the different timescales.

Parallel to the timescales, we introduce two length scales; the first is chosen as the piston length and the second as a typical penetration following a percussive activation

$$L_1 = L_p, \qquad L_2 = \sqrt{\frac{F_0 D_1}{K_R}}. \tag{3.18}$$

They have magnitudes (in millimeters)

$$L_1 = \mathcal{O}(10^2), \qquad L_2 = \mathcal{O}(10^{-1}). \tag{3.19}$$

Also, the second length scale can be related to the one used in the scaling of the drifting oscillator by evaluating the percussive impulse in accordance with the scaling of the pressure law. We then have $I = I_P = \sqrt{F_0 D_1 M_p}$ and the drifting oscillator reference length scale reads $L = L_2/\sqrt{\omega_{21}}$. Given that $\omega_{21} = \mathcal{O}(1)$ for typical drilling systems, the reference scales are equivalent, in the sense that they have the same order of magnitude.

To further the parallel with the drifting oscillator, we select T_4 as the reference timescale and define the dimensionless time with respect to the duration of a typical drilling cycle

$$\tau := \frac{t}{T_4}. \tag{3.20}$$

Additionally, we also define the dimensionless abscissa and displacement fields with respect to the introduced length scales

$$\xi_i := \frac{x_i}{L_1}, \qquad \mathcal{U}_i := \frac{u_i}{L_2}. \tag{3.21}$$

Introducing the scaled variables in the equations of motion, we get

$$\ddot{\mathcal{U}}_i = \omega_{41}^2 \mathcal{U}_i'' + \phi_i, \quad i \in \{p; b\}, \tag{3.22}$$

Table 3.1: Parameters entering the governing equations and their generic units (M: mass, L: length, T: time).

Dependent variables	u_p	L	u_b	L		
Independent variables	x_p	L	x_b	L	t	T
Material	E	$\mathsf{ML}^{-1}\mathsf{T}^{-2}$	ρ	ML^{-3}		
Geometry	L_p	L	L_b	L	A	L^2
Static loads	G	LT^{-2}	F_S	MLT^{-2}		
Pressure law	D_1	L	F_0	MLT^{-2}	α	1
Bit/rock interaction	K_R	MT^{-2}	C_R	MT^{-1}	W_R	$\mathsf{ML}^2\mathsf{T}^{-2}$
	γ	1	β_R	1	u_R	L
Contact	g_0	L				

Table 3.2: Definition of dimensionless variables and parameters.

Dependent variables	$\mathcal{U}_p := u_1/L_2$	$\mathcal{U}_b := u_b/L_2$	
Independent variables	$\xi_p := x_p/L_1$	$\xi_b := x_b/L_1$	$\tau := t/T_1$
Scale ratios	$\omega_{21} := T_2/T_1$	$\omega_{41} := T_4/T_1$	$\omega_{15} := T_1/T_5$
Static loads	$\varpi := G(T_4^2/L_2)$	$\phi_S := F_S/M_bG$	
Pressure law	$\delta_1 := D_1/L_2$	$\phi_0 := F_0/M_pG$	α
Bit/rock interaction	$\kappa_R := \omega_{21}$	$\zeta_R := \varrho\omega_{41}\omega_{15}$	$\psi_R := \omega_{21}/\omega_{41}\omega_{15}$
	$\varrho := W_R/F_0D_1$	γ	
	$\mathcal{U}_R := u_R/L_2$	β_R	
Contact	$\mathcal{G}_0 := g_0/L_2$		

Table 3.3: Practical ranges of order magnitudes of the dimensionless groups.

Scale ratios	$\omega_{21} = 1$	$\omega_{41} \in [10^{-1}, 1]$	$\omega_{15} \in [10^{-1}, 1]$
Static loads	$\varphi_S \in [1, 10^2]$	$\varpi \in [10^{-8}, 10^{-5}]$	
Pressure law	$\varphi_0 \in [1, 10^2]$	$\delta_1 \in [10, 10^3]$	$\alpha \in \{-1; 1\}$
Bit/rock interaction	$\kappa_R = 1$	$\zeta_R \in [10^{-8}, 10^{-2}]$	$\psi_R \in [1, 10^2]$
	$\gamma \in (1, 10^3]$	$\varrho \in [10^{-6}, 10^{-2}]$	$\mathcal{U}_R = 1$
Contact	$\mathcal{G}_0 \in [10^{-2}, 10^2]$		

where an overhead dot defines differentiation with respect to the dimensionless time and a prime symbol differentiation with respect to the dimensionless abscissa, $\dot{\mathcal{U}}_i := \partial\mathcal{U}_i/\partial\tau$, $\mathcal{U}_i' := \partial\mathcal{U}_i/\partial\xi_i$. The dimensionless body force reads $\phi_i := (T_4^2/L_2)f_i$. Specializing to the piston and the bit, they can be written as

$$\phi_p = \varpi\left(\alpha\varphi_0 + 1\right), \qquad \phi_b = \varpi(\varphi_S + 1), \tag{3.23}$$

with $\varpi := G/(L_2/T_4^2)$ the ratio between the acceleration due to gravity and that associated with the drilling process, $\varphi_0 := F_0/M_pG$ the load due to the pressure force on the piston and $\varphi_S := F_S/M_bG$ the static feed force applied to the bit. The use of curly variables, φ, is reserved to dimensionless forces scaled by the reduced gravity ϖ; straight ones, ϕ, are used for other dimensionless forces. Similarly, the boundary conditions can be expressed in terms of dimensionless variables. For the piston, we have

$$\mathcal{U}_p'(0,\tau) = 0, \qquad 0 \leq -\mathcal{U}_p'(1,\tau) \perp \mathcal{G} \geq 0, \tag{3.24}$$

with the dimensionless gap $\mathcal{G} := g/L_2$. Introducing the scaled penetration while drilling, $\mathcal{P}(\tau) := p(t(\tau))/L_2$, the boundary conditions for the bit can be expressed as

$$0 \leq -\mathcal{U}_b'(0,\tau) \perp \mathcal{G} \geq 0, \qquad \mathcal{U}_2'(\omega_{21},\tau) = \begin{cases} 0 & \mathsf{FF}, \\ \kappa_R\mathcal{P} + \zeta_R\dot{\mathcal{P}} & \mathsf{DFC}, \\ \kappa_R\mathcal{P} & \mathsf{FC}, \\ \gamma\kappa_R\left(\mathcal{P} - \mathcal{P}_u\right) & \mathsf{BC}, \end{cases} \tag{3.25}$$

with $\kappa_R := \omega_{21}, \zeta_R := \varrho\omega_{41}\omega_{15}, \mathcal{P}_u := p_u/L_2$. The mode transition conditions merely follow from the definitions given in Figure 1.7 by replacing the dimensional penetration-related variables by their dimensionless counterpart and rewriting the threshold condition as

$$\int_0^{\bar{\tau}} \dot{\mathcal{P}}^2(\tau)\,\mathrm{d}\tau = \psi_R, \tag{3.26}$$

with $\psi_R := \omega_{21}/\omega_{41}\omega_{15}$. Table 3.2 lists all the dimensionless numbers that enter the scaled equations; 15 of them are required to fully define the problem, with, for instance (another set could have been chosen), τ, ξ_i, ω_{41}, ω_{21}, ω_{15}, ϖ, φ_S, α, φ_0, δ_1, ϱ, γ, β_R, $\mathcal{U}_R$, $\mathcal{G}_0$. Parameters β_R,$\mathcal{U}_R$ are related to the bit/rock interaction law, they generically represent the discrete drilling mode and the history variables; $\delta_1 := D_1/L_2$ is the scaled

switch distance entering the definition of the pressure law. On the basis of typical dimensional parameters for percussive drilling systems, practical ranges can be identified for the dimensionless groups. They are given in Table 3.3.

3.2.3 Semi-discrete computational model

A vast number of numerical methods have been developed to numerically solve wave propagation problems, *e.g.*, spectral collocation methods [57, 58, 59], approximations based on finite differences [60, 61], or discontinuous Galerkin formulations [62, 63, 64]. In this ocean of literature, the choice of a method must be guided by the specifics of the problem.

The main driver to our choice has been the piecewise linear nature of the governing equations. It has led us to retain the standard dynamic finite element approach [60, 65, 66] with an embedded event-driven integration procedure [39, 41]. Following this strategy, the governing equations are semi-discretized in space to yield the equations of motion ruling the dynamics of the semi-discrete approximation to the continuous system. These are then integrated in time to yield the discrete approximation to the original continuous problem. We now define the semi-discrete approximation. Details about its integration in time are deferred to Chapter 4.

Given the 1-dimensional setting of the problem, the application of the finite element method is a mere exercise. We leave it to the reader to consult references on the topic if need be, for instance, the introductory monograph of Hughes [65]. Upon application of the method, the semi-discrete equations of motion approximating the dynamics of the piston and the bit can be stated in the generic form

$$\mathbf{M}\dot{\boldsymbol{\mathcal{V}}} + \mathbf{C}_R\boldsymbol{\mathcal{V}} + (\mathbf{K} + \mathbf{K}_R + \mathbf{K}_C)\boldsymbol{\mathcal{U}} = \boldsymbol{\phi} + \alpha\boldsymbol{\phi}_P + \boldsymbol{\phi}_R + \boldsymbol{\phi}_C, \tag{3.27}$$

with $\boldsymbol{\mathcal{V}} = \dot{\boldsymbol{\mathcal{U}}}$. Vectors $\boldsymbol{\mathcal{U}}(\tau), \boldsymbol{\mathcal{V}}(\tau) \in \mathbb{R}^d$ denote the nodal displacements and velocities of the d degrees of freedom of the semi-discrete system and matrices $\mathbf{K}, \mathbf{M} \in \mathbb{R}^{d\times d}$, with $\mathbf{K} \geq 0, \mathbf{M} > 0$, the symmetric 2-block diagonal stiffness and mass matrices. They are obtained by combination of the assembled matrices for a single bar on the basis of a uniform mesh; matching element sizes are used for the piston and bit meshes. For linear

($p = 1$) and quadratic ($p = 2$) elements, the element matrices are given by

$$\mathbf{K}^e_{p=1} := \frac{\omega_{41}^2}{L_e}\begin{pmatrix} 1 & -1 \\ -1 & 1 \end{pmatrix}, \qquad \mathbf{M}^e_{p=1} := \frac{L_e}{12}\begin{pmatrix} 5 & 1 \\ 1 & 5 \end{pmatrix}, \tag{3.28}$$

$$\mathbf{K}^e_{p=2} := \frac{\omega_{41}^2}{3L_e}\begin{pmatrix} 7 & -8 & 1 \\ -8 & 16 & -8 \\ 1 & -8 & 7 \end{pmatrix}, \qquad \mathbf{M}^e_{p=2} := \frac{L_e}{30}\begin{pmatrix} 4 & 2 & -1 \\ 2 & 16 & 2 \\ -1 & 2 & 4 \end{pmatrix}; \tag{3.29}$$

where L_e refers to the element length and the average of the lumped and consistent mass matrices is used in the linear case, for it is known to yield more accurate results [65, 67]. The static loads are embedded in the constant load vector

$$\boldsymbol{\phi} := \varpi(\mathbf{M}\mathbf{1}_p + (1 + \varphi_s)\mathbf{M}\mathbf{1}_b), \tag{3.30}$$

where vectors $\mathbf{1}_i$ have unit entries at rows corresponding to degrees of freedom associated with body $i \in \{p; b\}$ and zeros at other entries.

Quantities subscripted by P pertain to the definition of the pressure law, these by R to that of the bit/rock interaction law, and those by C to the status of the contact interface at the piston/bit interface. Their update is governed by the occurrence of events or mode transitions. Figure 3.4 summarizes all the possible dynamics mode transitions in the elastic two-body model, by reference to the event functions $\mathcal{Q}_i$ defined next.

Contact interaction

To handle the contact interaction between the two bodies, a penalty formulation is used [66, 68, 69]. In physical terms, this approach is equivalent to introducing a fictitious constitutive contact model at the interface. In mathematical terms, it corresponds to relaxing the complementarity conditions entering (3.24) and (3.25) by allowing the interpenetration of the contacting bodies and defining the contact force as a function of this interpenetration.

Let the signed localization vector $\mathbf{w}_C \in \mathbb{R}^d$ be defined so that the gap function, *i.e.*, the distance between the piston and the bit contact nodes, is given by

$$\mathcal{Q}_1 := \mathbf{w}_C^T\boldsymbol{\mathcal{U}} + \mathcal{G}_0. \tag{3.31}$$

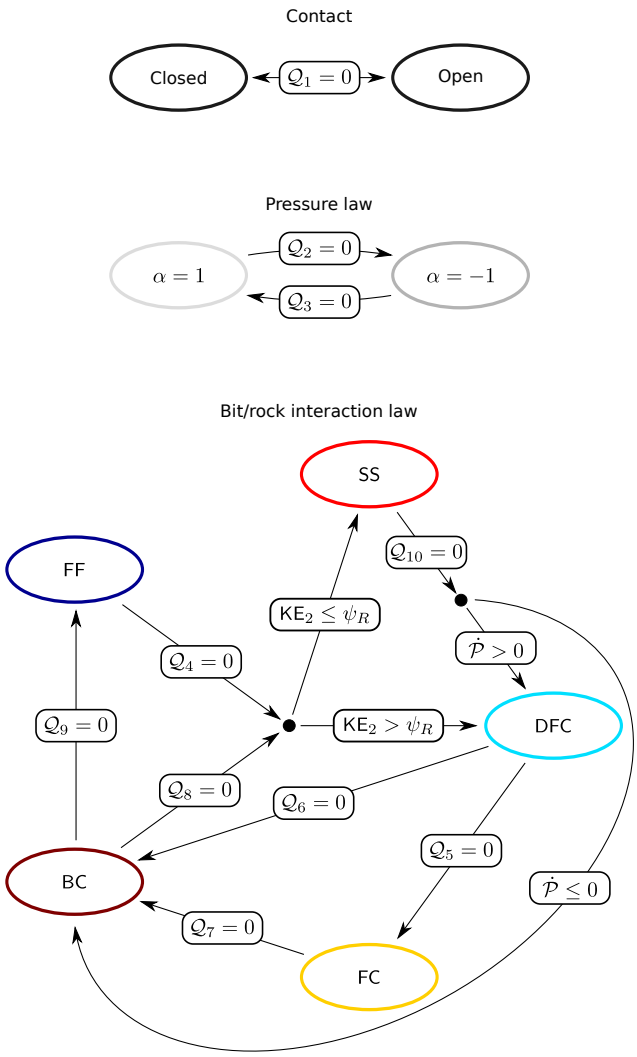

Figure 3.4: Mode transition pattern for the two-body elastic model.

Thus, vector $\mathbf{w}_C \in \mathbb{R}^d$ has zero entries everywhere but at the degrees of freedom corresponding to the contact nodes. Given the convention of positive displacements in the downward direction, the non-zero entries are given by -1 and 1 for the piston and the bit, respectively. Following that definition, the use of a quadratic contact potential translates into a contact force proportional to the interpenetration and

$$\mathbf{K}_C := \kappa_C \mathbf{w}_C \mathbf{w}_C^T \qquad\qquad \boldsymbol{\phi}_C := -\kappa_C \mathbf{w}_C \mathcal{G}_0, \tag{3.32}$$

whenever $\mathcal{Q}_1 < 0$. They vanish when the gap function is positive.

Parameter κ_C represents the numerical contact stiffness. In its dimensional form, it can be shown to correspond to a scaling of the bit/rock interaction stiffness $K_C := K_R(\kappa_C/\omega_{21})$. The use of the penalty method thus introduces the additional timescale

$$T_6 := \frac{1}{\sqrt{\kappa_C}} T_4 \tag{3.33}$$

in the semi-discrete model.

The choice of the contact stiffness is discussed in Chapter 4. Too large values excite spurious high-frequency oscillations. Too low values allow large interpenetrations that are not representative of the original problem.

Pressure law

The pressure force driving the piston motion is defined according to its average motion relative to that of the bit. Defining the average relative motion as

$$\upsilon_r := \langle \boldsymbol{\mathcal{U}}_p \rangle_\xi - \langle \boldsymbol{\mathcal{U}}_b \rangle_\xi - \mathcal{G}_0, \tag{3.34}$$

with the spatially averaged displacements at the center of mass

$$\langle \boldsymbol{\mathcal{U}}_p \rangle_\xi := \mathbf{1}_p^T \mathbf{M} \boldsymbol{\mathcal{U}}, \qquad\qquad \langle \boldsymbol{\mathcal{U}}_b \rangle_\xi := \frac{1}{\omega_{21}} \mathbf{1}_b^T \mathbf{M} \boldsymbol{\mathcal{U}}, \tag{3.35}$$

the two event functions relative to the pressure law read

$$\mathcal{Q}_2 := \upsilon_r, \tag{3.36}$$

$$\mathcal{Q}_3 := \upsilon_r + \delta_1. \tag{3.37}$$

We define them as mutually exclusive; that is, only one of them can be active at a given time. This slight deviation from the definition (3.1) further enforces the cyclicity of the piston motion. The ID of the active function is tracked by the value of parameter α that gives the direction of application of the pressure force. When $\alpha = 1$, the pressure force points downwards and $\mathcal{Q}_2$ is active. When $\mathcal{Q}_2 = 0$ is realized, the pressure parameter is switched to $\alpha = -1$ and $\mathcal{Q}_3$ becomes active. The pressure parameter is reset to $\alpha = 1$ when $\mathcal{Q}_3 = 0$ is realized.

The static load vector associated with the pressure law is given by

$$\boldsymbol{\phi}_P := \varpi\varphi_0 \mathbf{M}\mathbf{1}_p. \tag{3.38}$$

Bit/rock interaction

The definition of the bit/rock interaction law that we use is an alteration of that given in Section 1.4; a standstill mode is added for reasons of computational efficiency, to avoid the numerous drilling mode switches taking place when the bit converges to equilibrium. This addition is motivated by the fact that whenever the bit kinetic energy is low as compared to the energy barrier, the penetration it achieves is negligible in comparison to that resulting from the percussive activation.

In dimensionless coordinates, the penetration while drilling is given by

$$\mathcal{P}(\tau) := \frac{p(t(\tau))}{L_2} = \mathbf{w}_R^T \boldsymbol{\mathcal{U}} - \mathcal{U}_{R,\ell} + \phi_{R,\ell}, \tag{3.39}$$

where $\mathbf{w}_R$ is the localization vector of the bit degree of freedom located at the bit/rock interface, with zero entries everywhere but a unit entry at that degree of freedom; $\mathcal{U}_{R,\ell}$ and $\phi_{R,\ell}$ denote the position of the contact degree of freedom and the value of the interaction force at the start of the drilling cycle. The instantaneous rate of penetration is given by

$$\dot{\mathcal{P}}(\tau) := \mathbf{w}_R^T \boldsymbol{\mathcal{V}}. \tag{3.40}$$

When the interaction mode is free flight (FF), the contact at the bit/rock interface is open and the interaction force is zero. Thus, the mode-dependent quantities are zero, *i.e.*,

$$\mathbf{K}_R = \mathbf{C}_R = \mathbf{0}, \qquad \boldsymbol{\phi}_R = \mathbf{0}. \tag{3.41}$$

From the FF mode, the interaction law can either switch to the dissipative forward contact mode (DFC) or the standstill mode (SS). The switch occurs at the closure of the interface gap; that is, when

$$\mathcal{Q}_4 := \mathcal{P} - \mathcal{P}_u \tag{3.42}$$

is equal to zero. The transition to either mode depends on the magnitude of the bit kinetic energy

$$\mathsf{KE}_b := (\mathbf{I}_b \boldsymbol{\mathcal{V}})^T \mathbf{M} (\mathbf{I}_b \boldsymbol{\mathcal{V}})/2. \tag{3.43}$$

Matrix $\mathbf{I}_b$ is the restriction of the identity matrix to the degrees of freedom of the bit; it has zero diagonal entries for the piston ones. If $\mathsf{KE}_b > \psi_R$, a new drilling cycle is initiated and the interaction law switches to the DFC mode. In the opposite case, the interaction law switches to the SS mode.

In the DFC mode, the mode-dependent quantities are given by

$$\mathbf{K}_R := \kappa_R \mathbf{w}_R \mathbf{w}_R^T, \qquad \mathbf{C}_R := \zeta_R \mathbf{w}_R \mathbf{w}_R^T, \qquad \boldsymbol{\phi}_R := \kappa_R \mathbf{w}_R (\mathcal{U}_{R,\ell} - \phi_{R,\ell}). \tag{3.44}$$

Two transitions are authorized. Either the energy barrier is reached and the interaction law switches to the forward contact mode (FC), or the velocity of the contact node vanishes and the interaction law switches to the backward contact mode (BC). The first switch corresponds to the zeros of the event function

$$\mathcal{Q}_5 := \psi(\dot{\mathcal{P}}) - \psi_R, \tag{3.45}$$

where $\psi(\dot{\mathcal{P}})$ represents the work done by the viscous force component of the interaction law, as evaluated by formula (4.9). The second transition is defined by the zeros of the event function

$$\mathcal{Q}_6 := \dot{\mathcal{P}}. \tag{3.46}$$

During FC motion, the mode-dependent quantities read

$$\mathbf{K}_R := \kappa_R \mathbf{w}_R \mathbf{w}_R^T, \qquad \mathbf{C}_R := \mathbf{0}, \qquad \boldsymbol{\phi}_R := \kappa_R \mathbf{w}_R (\mathcal{U}_{R,\ell} - \phi_{R,\ell}). \tag{3.47}$$

Only one transition is authorized, to the BC mode. It occurs when the instantaneous rate of penetration vanishes, *i.e.*, at a zero of

$$\mathcal{Q}_7 := \dot{\mathcal{P}}. \tag{3.48}$$

When the interaction law is in the BC mode, the mode-dependent quantities are defined as

$$\mathbf{K}_R := \gamma\kappa_R \mathbf{w}_R \mathbf{w}_R^T, \qquad \mathbf{C}_R := \mathbf{0}, \qquad \boldsymbol{\phi}_R := \gamma\kappa_R \mathbf{w}_R \mathcal{U}_{R,u}, \tag{3.49}$$

with the upper displacement $\mathcal{U}_{R,u} := \mathcal{P}_u + \mathcal{U}_{R,\ell} - \phi_{R,\ell}$ and the upper penetration $\mathcal{P}_u := \mathcal{P}_p(\gamma - 1)/\gamma$ given as a function of the peak penetration reached at the transition to the BC mode. Transitions to three modes can take place. Upon vanishing of the instantaneous rate of penetration, the interaction law can switch to either the DFC or the SS mode

$$\mathcal{Q}_8 := \dot{\mathcal{P}}.$$

Conditions for the start of a new drilling cycle are identical to the ones enforced after the FF mode; if $\mathsf{KE}_b > \psi_R$, the interaction law switches to the DFC mode, otherwise it switches to the SS mode. Upon vanishing of the contact force, *i.e.*, when event function

$$\mathcal{Q}_9 := \mathcal{P} - \mathcal{P}_u$$

vanishes, contact opens at the bit/rock interface and the interaction law enters the FF mode.

In the SS mode, the mode-dependent quantities are given by

$$\mathbf{K}_R := \gamma\kappa_R \mathbf{w}_R \mathbf{w}_R^T, \qquad \mathbf{C}_R := \zeta_R \mathbf{w}_R \mathbf{w}_R^T, \qquad \boldsymbol{\phi}_R := \gamma\kappa_R \mathbf{w}_R \mathcal{U}_{R,u}. \tag{3.50}$$

Thus, during standstill, the bit rests on Kelvin-Voigt viscoelastic cell, with stiffness $\gamma\kappa_R$ and viscosity ζ_R. As the occurrence of standstill typically occurs during phases of independent motion of the piston and the bit, it is expected that the interaction force converges to the sum of the bit weight and applied feed force, $\phi_R \to \omega_{21}(1+\varphi_S)\varpi$. The bit is authorized to leave the SS mode when it has sufficient energy to overcome the energy barrier; that is, when

$$\mathcal{Q}_{10} := \mathsf{KE}_b - \psi_R$$

vanishes. Transition to either the DFC or the BC mode is allowed depending on the sign of the instantaneous rate of penetration $\dot{\mathcal{P}}$.

3.3 Rigid model

3.3.1 Assumption of timescale separation

The scaling analysis of the elastic model has revealed that the dynamics of the drilling process evolves on multiple timescales. Although a coupling of the extreme and separated timescales is expected through the intermediate ones, it is nevertheless tempting to formulate a multiscale model that is built on assumptions of timescale separation.

To that end, let the following hypothesis be stated

$$T_1, T_2, T_5 \ll T_3, T_4; \tag{3.51}$$

that is, all phenomena evolving on timescales faster than T_4 can be considered as instantaneous; T_3 is typically one to two orders of magnitude larger than T_4. Following this assumption, the piston and the bit can be considered as rigid bodies on timescale T_4. Also, the DFC drilling mode as well as the interaction between the piston and the bit collapse in time.

3.3.2 Two degrees of freedom model

Under these hypotheses, the dimensional equations of motion ruling the piston and the bit dynamics, between percussive activations, read

$$\begin{aligned} M_p \dot{v}_p &= M_p G + \alpha F_0, \\ M_b \dot{v}_b &= M_b G + F_S - F_R, \end{aligned} \tag{3.52}$$

with $\dot{v}_p, \dot{v}_b$ denoting the piston and bit accelerations; the overhead dot is again used as a shorthand notation for time differentiation. As the DFC mode collapses in time, the bit/rock interaction model to be used is the one that was coupled to the drifting oscillator. The definition of the bit/rock interaction force given in Figure 2.2 is thus of application, in combination with the instantaneous enforcement of the energy barrier at the start of a drilling cycle, as given by equation (2.5), with $\dot{p}_\ell = v_{b,\ell}$ (the bit velocity at the start of a drilling cycle). Parameters α, F_0 follow from the definition of the pressure law introduced in Section 3.1. Due to the rigid body assumption, the piston motion relative to that of the bit corresponds to the opposite of the gap function between the

piston and the bit and of its time derivative that are used to track the occurrence of percussive activation

$$u_r = -g := u_p - u_b - g_0, \qquad v_r = -\dot{g} := v_p - v_b. \tag{3.53}$$

To complete the model definition, the contact interaction between the piston and the bit must be specified. Under the assumption of timescale separation, $T_1, T_2 \ll T_4$, this interaction is instantaneous with respect to the body motion and gives rise to jump discontinuities of the piston and bit velocities. To quantify them, we introduce the following reset map

$$v_p^+ = v_p^- \left(1 - \frac{\tau_C}{2}\right) + v_b^- \left(\omega_{21} - \frac{\tau_C}{2} + \frac{1 - \mathrm{e}^{-\eta(\tau_C - \omega_{21})}}{\eta}\right), \tag{3.54}$$

$$\begin{aligned} v_b^+ = {} & \frac{v_p^-}{\omega_{21}} \left(\omega_{21} - \frac{\tau_C}{2} + \frac{1 - \mathrm{e}^{-\eta(\tau_C - \omega_{21})}}{\eta}\right) \\ & + \frac{v_b^-}{\omega_{21}} \left(\frac{\tau_C}{2} - \omega_{21} + \frac{2e^{-\eta(\tau_C - \omega_{21})} - e^{-\eta\tau_C} - 1}{\eta}\right). \end{aligned} \tag{3.55}$$

that defines the post-contact velocities, v_p^+, v_b^+, as a function of the pre-contact velocities, v_p^-, v_b^-, of the bit/rock interaction mode through stiffness parameter η and of the system geometry via ω_{21}. These equations express the exact post-contact average velocities of two elastic bars experiencing a collinear longitudinal impact, with one of them being elastically supported by a spring of stiffness η; this model problem is illustrated in Figure 3.5. Complete details can be found in Appendix B. Parameter τ_C denotes the duration of the contact phase on the normalized timescale of wave propagation; it is given by

$$\tau_C = \omega_{21} - \frac{1}{\eta} \ln\left(\frac{v_p^-}{2v_b^-} + \frac{1}{2}\right) \tag{3.56}$$

if

$$v_b^- < v_p^- < v_b^- \left(2\mathrm{e}^{\eta(\omega_{21} - 2)} - 1\right), \tag{3.57}$$

and by

$$\tau_C = 2, \tag{3.58}$$

otherwise. For application to the percussive drilling model, stiffness parameter η must be scaled with the bit/rock interaction stiffness; simplifying all expressions, we have

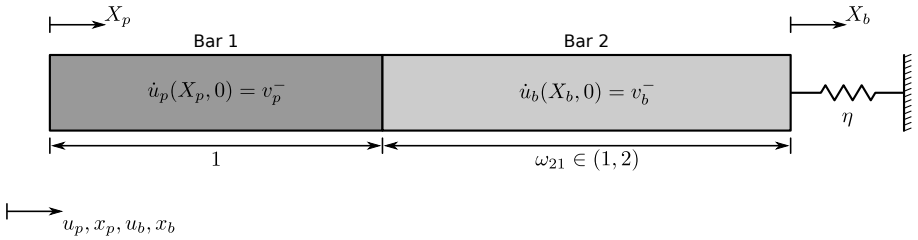

Figure 3.5: Collinear longitudinal impact of similar bars with an elastic boundary condition at the rightmost bar end, scaled model problem.

$\eta = 0$ in the FF and SS modes, $\eta = \omega_{24}/\omega_{41}$ in the FC mode,F and $\eta = \gamma\omega_{24}/\omega_{41}$ in the BC mode.

The validity of the reset map is restricted to bit/piston length ratios $\omega_{21} \in (1, 2)$, which are typical of percussive drilling systems.

3.3.3 Dimensionless model

The reference scales T_3, T_4 and L_2 identified for the elastic model equally apply to the rigid model. Therefore, they can be used as a basis to reformulate the model in dimensionless coordinates. Taking L_2 and T_4 as reference scales to define the dimensionless variables, the equations of motion can be cast in the matrix form

$$\mathbf{M}\dot{\boldsymbol{\mathcal{V}}} + \mathbf{K}_R\boldsymbol{\mathcal{U}} = \boldsymbol{\phi} + \alpha\boldsymbol{\phi}_P + \boldsymbol{\phi}_R. \tag{3.59}$$

The displacement and velocity vectors are the vertical concatenation of the piston and bit scaled displacements and velocities. Given the problem scaling, the mass matrix is the identity matrix of dimension 2, $\mathbf{M} = \mathbf{I}$, and the vector of constant static loads is given by

$$\boldsymbol{\phi} := \varpi \begin{pmatrix} 1 \\ 1+\varphi_S \end{pmatrix}. \tag{3.60}$$

The other quantities are mode-dependent and detailed below; their definition is a simplification of the ones pertaining to the elastic model. The possible mode transitions are shown in Figure 3.6.

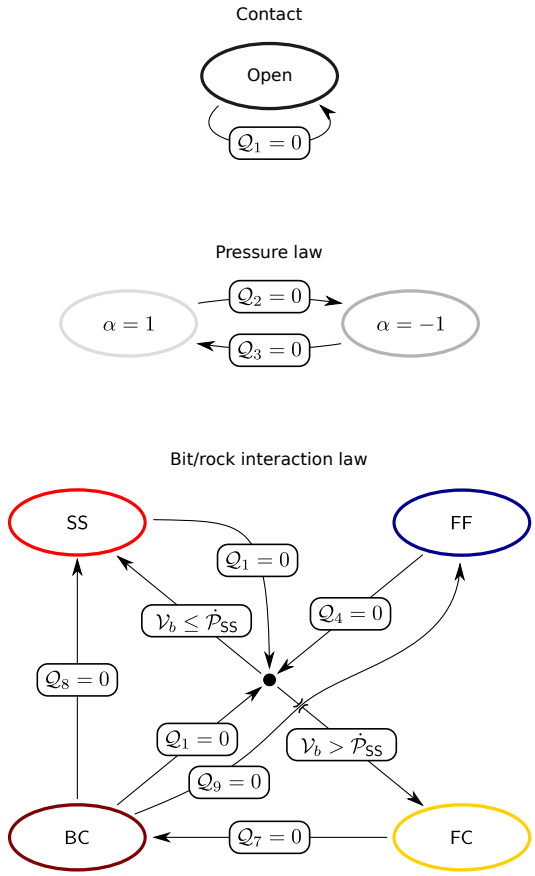

Figure 3.6: Mode transition pattern for the two-body rigid model.

Contact interaction

The occurrence of contact is tracked by the gap function between the piston and the bit, defined as

$$\mathcal{Q}_1 := \mathcal{U}_b - \mathcal{U}_p + \mathcal{G}_0. \tag{3.61}$$

Whenever the gap function vanishes, the reset map is applied to the piston and bit velocities. Equations (3.54)-(3.55) are scaling-independent given that both sides have the dimension of velocity and that all function arguments are expressed by dimensionless groups. They can thus be used with the dimensionless model by way of the mere substitution $v_i^{\pm} \leftarrow \mathcal{V}_i^{\pm}, i \in \{p; b\}$.

Pressure law

Under the assumption of rigid bodies, the gap function and the relative motion between the piston and the bit are opposite of each other

$$\mathcal{Q}_2 := -\mathcal{Q}_1. \tag{3.62}$$

Thus, the pressure force switch at zero relative motion coincides with the occurrence of percussive activation. When $\mathcal{Q}_2$ vanishes, the pressure force direction is set to upwards, *i.e.*, $\alpha = -1$. The other transition, $\alpha \leftarrow 1$, takes place at zeros of

$$\mathcal{Q}_3 := \mathcal{U}_p - \mathcal{U}_b - \mathcal{G}_0 + \delta_1. \tag{3.63}$$

The load vector associated with the pressure force is given by

$$\boldsymbol{\phi}_P := \varpi\varphi_0 \begin{pmatrix} 1 \\ 0 \end{pmatrix}. \tag{3.64}$$

Again, the modes associated with the pressure law are set as mutually exclusive.

Bit/rock interaction law

In the rigid model, the penetration while drilling is defined on the basis of the motion of the bit center of gravity. It is given by

$$\mathcal{P}(\tau) := \mathcal{U}_b - \mathcal{U}_{R,\ell} + \phi_{R,\ell}. \tag{3.65}$$

When the interaction mode is free flight (FF), the contact at the bit/rock interface is open and the interaction force is zero. Thus, the mode-dependent quantities are zero, *i.e.*,

$$\mathbf{K}_R = \mathbf{0}, \qquad \boldsymbol{\phi}_R = \mathbf{0}. \tag{3.66}$$

From the FF mode, the interaction law can either switch to the forward contact mode (FC) or the standstill mode (SS). The switch occurs at the closure of the interface gap; that is, when

$$\mathcal{Q}_4 := \mathcal{P} - \mathcal{P}_u \tag{3.67}$$

equals zero. The transition to either mode depends on the kinetic energy of the bit. If $\mathcal{V}_b > \dot{\mathcal{P}}_{\mathsf{SS}}$, with $\dot{\mathcal{P}}_{\mathsf{SS}} := \sqrt{2\varrho}$, a new drilling cycle is initiated and the interaction law switches to the FC mode; the bit kinetic energy is instantaneously decreased by the amount of the energy barrier

$$\mathcal{V}_b^+ = \sqrt{(\mathcal{V}_b^-)^2 - (\dot{\mathcal{P}}_{\mathsf{SS}})^2}. \tag{3.68}$$

In the opposite case, the bit velocity is reduced to zero, $\mathcal{V}_b^+ = 0$, and the interaction law switches to the SS mode.

During FC motion, the mode-dependent quantities read

$$\mathbf{K}_R := \begin{pmatrix} 0 & 0 \\ 0 & 1 \end{pmatrix}, \qquad \boldsymbol{\phi}_R := (\mathcal{U}_{R,\ell} - \phi_{R,\ell}) \begin{pmatrix} 0 \\ 1 \end{pmatrix}. \tag{3.69}$$

One transition is authorized, it is to the BC mode. It occurs when the bit velocity vanishes, *i.e.*, at a zero of

$$\mathcal{Q}_7 := \dot{\mathcal{V}}_b. \tag{3.70}$$

When the interaction law is in the BC mode, the mode-dependent quantities are defined as

$$\mathbf{K}_R := \gamma \begin{pmatrix} 0 & 0 \\ 0 & 1 \end{pmatrix}, \qquad \boldsymbol{\phi}_R := \gamma \mathcal{U}_{R,u} \begin{pmatrix} 0 \\ 1 \end{pmatrix}, \tag{3.71}$$

with the upper displacement $\mathcal{U}_{R,u} := \mathcal{P}_u + \mathcal{U}_{R,\ell} - \phi_{R,\ell}$ and the upper penetration $\mathcal{P}_u := \mathcal{P}_p(\gamma - 1)/\gamma$ given as a function of the peak penetration reached at the transition to the BC mode. Transitions to three modes can take place. Upon vanishing of the bit velocity, the interaction law switches to the SS mode

$$\mathcal{Q}_8 := \dot{\mathcal{V}}_b; \tag{3.72}$$

according to the energetic analysis of the drilling cycle of Section 2.5, such transition is only expected to happen if $\gamma \to \infty$, however. Upon vanishing of the contact force, *i.e.*, when the event function

$$\mathcal{Q}_9 := \mathcal{P} - \mathcal{P}_u \tag{3.73}$$

vanishes, the bit/rock interface opens and the interaction law enters the FF mode. Following a percussive activation, a new drilling cycle can be started and the interaction

law switched to the FC mode provided the post-activation bit velocity verifies $\mathcal{V}_b^+ > \dot{\mathcal{P}}_{\mathsf{SS}}$. In case the velocity changes sign but does not verify the energy barrier condition, the interaction law is switched to the SS mode. If the bit velocity does not change sign following a percussive activation, then the interaction law remains in the BC mode.

In the SS mode, the mode-dependent quantities are defined by

$$\mathbf{K}_R := \mathbf{0}, \qquad \boldsymbol{\phi}_R := \varpi(1+\phi_S)\begin{pmatrix} 0 \\ 1 \end{pmatrix}. \tag{3.74}$$

It is to be noted that due to a difference of scaling, the interaction force is different by a factor ω_{21} from the limit to which the elastic model converges during standstill. The interaction law is authorized to leave the SS mode once the bit has sufficient energy to overcome the barrier. This can only happen following a percussive activation. Such transition must thus be tracked on the basis of $\mathcal{Q}_1$.

Chapter 4

Computational aspects

"Research is what I'm doing when I don't know what I'm doing."

W. von Braun

By formulation, the proposed models of the percussive drilling process are of non-smooth and piecewise nature. These properties require particular attention when it comes to numerically integrate their governing equations, as the transition points, at which the dynamics is switched, must be accurately captured. One integration strategy is the so-called event-driven integration [39, 41] that relies on the finding of the zeros of the event functions that control the occurrences of transition points, while integrating the governing equations.

On the basis of the model problem of a piecewise linear equation of motion complemented by event functions, we present in this chapter the numerical and computational developments that we have completed to numerically solve the piecewise-defined equations of motion of the two-body models of percussive drilling.

The numerical methods presented in this chapter have been reported in [37, 38].

4.1 Model problem

Let us consider the reference equation of motion of linear structural dynamics with piecewise-defined terms denoted by subscript $\mathcal{A}$

$$\mathbf{M}\dot{\mathbf{v}} + (\mathbf{C} + \mathbf{C}_{\mathcal{A}})\,\mathbf{v} + (\mathbf{K} + \mathbf{K}_{\mathcal{A}})\,\mathbf{u} = \mathbf{f} + \mathbf{f}_{\mathcal{A}}, \qquad \dot{\mathbf{u}} = \mathbf{v}. \tag{4.1}$$

The usual notation is used for the constant stiffness, damping, and mass matrices that are assumed symmetric and subject to the assumptions of definiteness common to mechanical problems; $\mathbf{K}, \mathbf{C} \geq 0$ and $\mathbf{M} > 0$, respectively. Each matrix is real and has dimensions $d \times d$, where d denotes the number of degrees of freedom of the problem. The displacement and velocity vectors are denoted by $\mathbf{u}, \mathbf{v} \in \mathbb{R}^d$ and, again, overhead dots indicate time differentiation. These and the external forcing $\mathbf{f} \in \mathbb{R}^d$ are functions of the independent time variable t. In the following developments, the piecewise-defined quantities are assumed constant between the transition points that correspond to the zeros of m independent active event functions. By independent, it is meant that to each event occurrence corresponds a single alteration of the piecewise-defined quantities and that, in case simultaneous events occur, there is no indeterminacy as to the update of these quantities. It is further assumed that these are given by an affine transformation of the state vector $\mathbf{x} := [\mathbf{u}\,;\,\mathbf{v}] \in \mathbb{R}^{2d}$

$$\mathbf{q} := \mathbf{W}^T\mathbf{x} + \mathbf{q}_0, \tag{4.2}$$

with $\mathbf{q}, \mathbf{q}_0 \in \mathbb{R}^m$ the vectors of event functions and their initial value, and $\mathbf{W} \in \mathbb{R}^{2d\times m}$ the state transformation matrix. Also, it is assumed that the event functions are continuous between events; impulsive loadings, if any, thus require special attention as they induce a discontinuity of the velocity field.

4.2 Event-driven integration

The essence of event-driven integration is simple. According to Acary and Brogliato [41], it can be described by three steps: (*i*) integrate the smooth vector field up to the next nonsmooth event, (*ii*) accurately locate the time of this transition, and (*iii*) identify the next dynamics mode and accordingly reinitialize the system at the event time. The trajectory of the dynamical system is thus constructed segment by segment and is

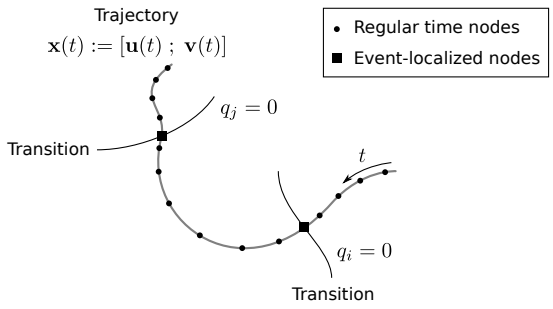

Figure 4.1: Piecewise smooth trajectory in state space.

expected to be smooth between events and, possibly, nonsmooth at events, depending on the nature of the transition. Figure 4.1 illustrates such a piecewise trajectory as it would be computed via an event-driven integration procedure. Every transverse crossing of the system trajectory with the hypersurface defined by zeros of an event function gives rise to an update of the equation of motion. These crossings are, obviously, to be detected and localized while integrating the governing equations.

Although simple in appearance, the implementation of a robust event-driven integration scheme requires overcoming several challenges inherent to floating point arithmetic and the discrete-time representation of a (piecewise) continuous-time problem. For instance, the handling of near-grazing situations or that of simultaneous events in finite precision can prove delicate. A proper combination of an integration procedure and a root-solving strategy is therefore required.

Algorithm 4.1 presents the main steps of the event-driven strategy that we have developed. After the initialization of the required variables, the procedure enters the event-driven integration loop that is conducted until the final simulation time is reached. The computation of each time increment is the result of several key intermediate steps. First, the provisional state $\mathbf{x}_{n+1} := \mathbf{x}(t_{n+1})$ at t_{n+1} is computed by use of a numerical integration scheme, assuming that the parameters of the equation of motion are frozen over the timestep. Second, event detection is conducted to verify that no event function changes sign over the timestep. If any do(es), the event localization module is called, else it is bypassed. This module computes the system state at intermediate times $t_k \in [t_n, t_{n+1}]$ approximating the earliest occurrence of an event over the timestep. It returns a time t_k and a corresponding state $\mathbf{x}_k := \mathbf{x}(t_k)$ prior to which events may or

Algorithm 4.1 Event-driven integration procedure.

Inputs: initial conditions, model data, integration parameters, root-solving parameters

Outputs: state and constraint time histories

```
Initialize procedure (storage, active constraints at initial time, etc.)
Loop over time increments until final simulation time is reached
   Compute provisional state x_{n+1} from x_n
   Detect event(s) that possibly occurred over [t_n, t_{n+1}]
   if events have been detected
      Localize earliest occurrence(s) and identify its(their) ID
      Compute post-transition state and update governing equations
   end if
n ← n + 1
end loop
return
```

may not have taken place. The effective timestep thus covers time interval $[t_n, t_k]$. Update of the post-transition state and the governing equation is then performed, if need be, and the next time increment taken from t_k. In case no event is detected on interval $[t_n, t_{n+1}]$, the provisional state is accepted and the next step taken from t_{n+1}.

4.2.1 Time integration

As per Hilber and Hughes [70], competitive time integration schemes devoted to structural dynamics should verify the following list of attributes:

(i) unconditional stability when applied to linear problems;

(ii) no more than one set of implicit equations should have to be solved at each step;

(iii) second-order accuracy, at least;

(iv) controllable algorithmic dissipation in the higher modes;

(v) self-starting.

One scheme that verifies these attributes is the energy-decaying scheme proposed by Bottasso and Trainelli [71]; we refer to it as the BoTr scheme. Related to the time

discontinuous Galerkin method [72, 73], the scheme was originally proposed in a four-level form, on the basis of an augmented state vector that includes discontinuity state variables at the beginning of the timestep. These quantities being virtually of no use in structural dynamics, we have reduced the scheme to a two-level form via static condensation of the one-step update equations; details are given in Appendix C. The two-level formulation, which we dub the DE^3 scheme, reads

$$\mathbf{H}_0 \mathbf{x}_{n+1} = \mathbf{H}_1 \mathbf{x}_n + \boldsymbol{\ell}_n^{n+1}, \tag{4.3}$$

with $\mathbf{x} := [\mathbf{u}\,;\,\mathbf{v}]$,

$$\begin{aligned}
\mathbf{H}_0 &:= \begin{pmatrix} \mathbf{C} + \frac{\chi+3}{6} h\mathbf{K} & \mathbf{M} - \frac{1+\chi}{12} h^2\mathbf{K} \\ \mathbf{M} - \frac{1+\chi}{12} h^2\mathbf{K} & -\frac{\chi+3}{6} h\mathbf{M} - \frac{1+\chi}{12} h^2\mathbf{C} \end{pmatrix}, \\
\mathbf{H}_1 &:= \begin{pmatrix} \mathbf{C} + \frac{\chi-3}{6} h\mathbf{K} & \mathbf{M} - \frac{1-\chi}{12} h^2\mathbf{K} \\ \mathbf{M} - \frac{1-\chi}{12} h^2\mathbf{K} & -\frac{\chi-3}{6} h\mathbf{M} - \frac{1-\chi}{12} h^2\mathbf{C} \end{pmatrix}, \\
\boldsymbol{\ell}_n^{n+1} &:= \begin{pmatrix} \mathbf{f}_1 \\ \left(t_{n+1/2} - \frac{\chi}{6} h\right) \mathbf{f}_1 - \mathbf{f}_2 \end{pmatrix},
\end{aligned} \tag{4.4}$$

where $\mathbf{f}_1 = \int_{t_n}^{t_{n+1}} \mathbf{f}(t)\,\mathrm{d}t$ and $\mathbf{f}_2 = \int_{t_n}^{t_{n+1}} t\mathbf{f}(t)\,\mathrm{d}t$ must be approximated by high-order quadrature. For instance, the Simpson-Cavalieri quadrature rule that ensures third degree exactness [60, p. 377] can be used; it is given by $\int_{t_n}^{t_{n+1}} f(t)\,\mathrm{d}t = (h/6)(f_n + 4f_{n+1/2} + f_{n+1})$, with the timestep $h := t_{n+1} - t_n$, $t_{n+1/2} := (t_n + t_{n+1})/2$ and $f_n := f(t_n)$. For legibility, we have not included the $\mathcal{A}$-subscripted quantities in the equations; they should, nonetheless, be included when dealing with the original problem. They are dropped as well in the remainder of this section and all references to the equation of motion consider equation (4.1) without them. As we will show, parameter $\chi \in [0, 1]$ controls the numerical dissipation introduced by the scheme during numerical integration and can be related to the spectral radius of the amplification matrix at infinite frequency ρ_∞

$$\chi := \frac{1 - \rho_\infty}{1 + \rho_\infty}, \tag{4.5}$$

in the absence of structural damping.

Alternatively, the update equation can be written in explicit form, upon solving it for the unknown state vector $\mathbf{x}_{n+1}$

$$\mathbf{x}_{n+1} = \mathbf{A}\mathbf{x}_n + \mathbf{b}_n^{n+1}. \tag{4.6}$$

The amplification matrix $\mathbf{A} := \mathbf{H}_0^{-1}\mathbf{H}_1$ and the direct load vector $\mathbf{b}_n^{n+1} := \mathbf{H}_0^{-1}\boldsymbol{\ell}_n^{n+1}$ completely characterize the accuracy and stability properties of the scheme.

Scheme stability

The commonly adopted criterion for stability is that the numerical solution should remain uniformly bounded over all computed time points [74]. For linear problems, the identification of the conditions under which a numerical scheme guarantees state boundedness can be achieved using different but equivalent arguments. For instance, spectral analysis [75] and frequency-domain analysis [76] assess internal stability on the basis of the location of the poles of the discrete equation of motion in the complex plane. Alternatively, energetic arguments, which are extensively used for the development of integration procedures dedicated to specific nonlinear problems, *e.g.*, [77, 78], can be used by relating the concept of stability to the conservation or decay of the system mechanical energy along the computed trajectory [79, 80]. Indeed, for the linear problem (4.1), the boundedness of the quadratic forms defining the mechanical (kinetic + strain) energy

$$E_n := \frac{1}{2}\mathbf{u}^T\mathbf{K}\mathbf{u} + \frac{1}{2}\mathbf{v}^T\mathbf{M}\mathbf{v} \tag{4.7}$$

implies the state boundedness. It is the latter approach that we follow to establish the unconditional stability of the scheme, as the derivation of the energy balance will be of later use.

Let the operators of variation and averaging over a timestep be defined as $\Delta x := x_{n+1} - x_n$ and $\bar{x} := (x_{n+1} + x_n)/2$. Following these definitions and equation (4.7), the variation of the mechanical energy over a timestep $\Delta E := \Delta\mathbf{v}^T\mathbf{M}\bar{\mathbf{v}} + \Delta\mathbf{u}^T\mathbf{K}\bar{\mathbf{u}}$ can be expressed as

$$\Delta E = W_{\text{ext}} - \Delta D_{\mathbf{C}} - \Delta D_{\text{num}}, \tag{4.8}$$

where $W_{\text{ext}}, \Delta D_{\mathbf{C}}$ and ΔD_{num} denote the work of the external forces, the viscous dissipation and the numerical dissipation, respectively, by balancing the work of the internal and external forces. Manipulating the definition of the integration scheme (4.4), the

contributions to the energy variation can be expressed as

$$\begin{aligned} W_{\text{ext}} &:= \frac{1}{h}\left(\Delta\mathbf{u}^T\mathbf{f}_1 - \Delta\mathbf{v}^T\left(t_{n+1/2}\mathbf{f}_1 - \mathbf{f}_2\right)\right), \\ \Delta D_{\mathbf{C}} &:= \frac{1}{h}\Delta\mathbf{u}^T\mathbf{C}\Delta\mathbf{u} + \frac{h}{12}\Delta\mathbf{v}^T\mathbf{C}\Delta\mathbf{v}, \\ \Delta D_{\text{num}} &:= \frac{\chi}{6}\left(-\Delta\mathbf{v}^T\mathbf{f}_1 + \Delta\mathbf{u}^T\mathbf{K}\Delta\mathbf{u} + \Delta\mathbf{v}^T\mathbf{M}\Delta\mathbf{v}\right) \\ &\quad + \frac{\chi h}{6}\left(\Delta\mathbf{v}^T\mathbf{K}\bar{\mathbf{u}} - \Delta\mathbf{u}^T\mathbf{K}\bar{\mathbf{v}} + \Delta\mathbf{v}^T\mathbf{C}\bar{\mathbf{v}}\right). \end{aligned} \tag{4.9}$$

It is observed that the work of the external forces includes a term proportional to the velocity variation over the timestep. This is a direct consequence of the scheme being high order. Also, the numerically conservative character of the scheme is confirmed for $\chi = 0$, as ΔD_{num} vanishes. To prove unconditional stability, we must show that $\Delta E \leq 0$ for all values of the timestep h, when $\mathbf{f}_1 = \mathbf{f}_2 = \mathbf{f} = 0$.

Although the quadratic forms of $\Delta D_{\mathbf{C}}$ show that structural damping does contribute to stability, as $\Delta D_{\mathbf{C}} \geq 0$ independently of h given the semi-definite positiveness of the damping matrix, the cross products involving state averages and variations in ΔD_{num} prevent us from verifying its positiveness and, *a fortiori*, the negativeness of ΔE. In fact, we must revert to the original four-level formulation of the scheme that is given in Appendix C to prove stability. For that formulation, the energy variation over a timestep reads

$$\begin{aligned} \Delta E = &\frac{1}{h}\Delta\mathbf{u}^T\mathbf{f}_1 + \frac{6}{h^2}[\![\mathbf{u}_n]\!]^T\left(t_{n+1/2}\mathbf{f}_1 - \mathbf{f}_2\right) - \frac{1}{h}\Delta\mathbf{u}^T\mathbf{C}\Delta\mathbf{u} \\ &- \frac{\chi}{2h}[\![\mathbf{u}_n]\!]^T\mathbf{K}[\![\mathbf{u}_n]\!] - \frac{3}{h}[\![\mathbf{u}_n]\!]^T\mathbf{C}[\![\mathbf{u}_n]\!] - \frac{\chi}{2h}[\![\mathbf{v}_n]\!]^T\mathbf{M}[\![\mathbf{v}_n]\!], \end{aligned} \tag{4.10}$$

with $[\![x_n]\!] := x_{n^+} - x_n$ denoting the jump discontinuity of variable x at time t_n. Segregation of the contributions is not as direct in this formalism, as can be seen by the absence of term proportional to $\chi\mathbf{f}_1$. However, setting the external loading to zero it readily appears from the quadratic forms involving the jump discontinuities of the state variables that $\Delta E \leq 0$ independently of the timestep h, given the assumptions on the definiteness of the governing matrices $\mathbf{K}, \mathbf{C}, \mathbf{M}$. Furthermore, this implies the positiveness of ΔD_{num} in the absence of external forcing and confirms the dissipative character of the integration scheme when $\chi > 0$.

In [67], Krenk proposed a scheme equivalent to the DE^3 scheme for undamped/unforced linear oscillators but that suffers a loss of accuracy in other configurations, in the

numerically dissipative setting. His spectral analysis of the amplification matrix thus applies to scheme (4.4) in the absence of structural damping. For that configuration, he showed [67, Eq. (42)] that the eigenvalues $\sigma_{\mathbf{A}}$ of the amplification matrix are complex conjugates with magnitude

$$|\sigma_{\mathbf{A}}|^2 = \frac{144 + (12 + 4\chi)\Omega_0^2 + (1 - \chi)^2\Omega_0^4}{144 + (12 + 4\chi)\Omega_0^2 + (1 + \chi)^2\Omega_0^4}, \tag{4.11}$$

where $\Omega_0 := \omega_0 h$ is the reduced eigenfrequency of the single degree of freedom undamped oscillator. This result confirms, from the spectral standpoint, the unconditional stability of the scheme as the amplification matrix has at most unit spectral radius for all values of the timestep. It also indicates, once more, that numerical integration is dissipative for $\chi > 0$ and conservative for $\chi = 0$. Furthermore, letting $\Omega_0 \to \infty$ and denoting the limit magnitude by ρ_∞, parametrization (4.5) is recovered and the range $\chi \in [0, 1]$ is confirmed.

Scheme accuracy

As Wood already reported [81, 82] and we, similarly, have demonstrated [37], the accuracy analysis of integration schemes based on the sole consideration of the scalar undamped/unforced linear oscillator can prove incorrect in certain circumstances. A consistent approach that incorporates the damping and forcing terms is required. To that end, we have developed a framework to analyze the accuracy of two-level integration schemes, which we apply here to the DE^3 scheme.

Let the following energy-based error measure be defined

$$e(t_n) := \frac{\sqrt{2}}{2} \left\| \mathbf{\Gamma}^{1/2}(\mathbf{x}_n - \underline{\mathbf{x}}(t_n)) \right\|_2, \tag{4.12}$$

where $\mathbf{\Gamma} := \mathrm{diag}(\mathbf{K}, \mathbf{M})$ is a symmetric positive semi-definite (in virtue of the assumptions on the mass and stiffness matrices) block diagonal scaling matrix and $\mathbf{x}_n$ the numerical approximation to the exact state vector $\underline{\mathbf{x}}(t_n)$ that is given by

$$\underline{\mathbf{x}}(t_n) := \mathrm{e}^{\mathbf{F}(t_n - t_0)}\underline{\mathbf{x}}(t_0) + \int_{t_0}^{t_n} \mathrm{e}^{\mathbf{F}(t_n - t)}\mathbf{g}(\tau)\,\mathrm{d}t, \tag{4.13}$$

with

$$\mathbf{F} := \begin{pmatrix} \mathbf{0} & \mathbf{I} \\ -\mathbf{M}^{-1}\mathbf{K} & -\mathbf{M}^{-1}\mathbf{C} \end{pmatrix}, \qquad \mathbf{g} := \begin{pmatrix} \mathbf{0} \\ \mathbf{M}^{-1}\mathbf{f} \end{pmatrix}. \tag{4.14}$$

This norm has been introduced by Romero [83] as the natural measure to quantify the errors arising from the numerical computation of the motion of mechanical systems. It can be interpreted as the mechanical energy associated with the errors on the displacement and velocity fields. Considering, without loss of generality, the error generated by a single increment of the integration procedure from initial time 0, that is, $\mathbf{x}_0 = \underline{\mathbf{x}}_0 = \underline{\mathbf{x}}(0)$, the error measure can be specialized to

$$e(h) = \frac{\sqrt{2}}{2} \left\| \mathbf{\Gamma}^{1/2} \left(\left(\mathbf{A} - \mathrm{e}^{\mathbf{F}h} \right) \underline{\mathbf{x}}_0 + \mathbf{b}_0^1 - \int_0^h \mathrm{e}^{\mathbf{F}(h-t)} \mathbf{g}(\tau)\, \mathrm{d}t \right) \right\|_2, \tag{4.15}$$

$$\leq \frac{\sqrt{2}}{2} \left\| \mathbf{\Gamma}^{1/2} \left(\mathbf{A} - \mathrm{e}^{\mathbf{F}h} \right) \underline{\mathbf{x}}_0 \right\|_2 + \frac{\sqrt{2}}{2} \left\| \mathbf{\Gamma}^{1/2} \left(\mathbf{b}_0^1 - \int_0^h \mathrm{e}^{\mathbf{F}(h-t)} \mathbf{g}(\tau)\, \mathrm{d}t \right) \right\|_2, \tag{4.16}$$

by use of the expressions for the numerical and analytical solutions, and of the triangle inequality. Thus, the total numerical error arising from a single timestep is bounded by the sum of two error components, relative to the free and forced responses of the system.

The first component is evidently proportional to the initial energy of the system $E_0 := \left\| \mathbf{\Gamma}^{1/2} \mathbf{x}_0 \right\|_2^2 / 2$. Further hypothesizing the positive definiteness of the scaling matrix $\mathbf{\Gamma}$, a condition that follows from the assumption of positive definiteness of the stiffness matrix, $\mathbf{K} > 0$, we free ourselves from this dependency by maximizing it over all initial conditions with unit energy $E_0 = 1$. This yields

$$e_1(h) := \left\| \mathbf{\Gamma}^{1/2} \left(\mathbf{A} - \mathrm{e}^{\mathbf{F}h} \right) \mathbf{\Gamma}^{-1/2} \right\|_2, \tag{4.17}$$

by definition of the matrix 2-norm (maximum singular value) [60, Theorem 1.2]. As to the second component, it is defined as

$$e_2(h) := \frac{\sqrt{2}}{2} \left\| \mathbf{\Gamma}^{1/2} \left(\mathbf{b}_0^1 - \int_0^h \mathrm{e}^{\mathbf{F}(h-t)} \mathbf{g}(\tau)\, \mathrm{d}t \right) \right\|_2 \tag{4.18}$$

and is problem specific through the definition of the external loading $\mathbf{g}(t)$.

Error components $e_1(h)$, $e_2(h)$ are easily identified as being proportional to the local truncation error as defined by Hughes [65] and to the timestep h. Therefore, the leading-order terms of their Taylor expansion around $h = 0$ directly yield the scheme orders of accuracy k_1, k_2 as regards the free and forced computed responses

$$e_1(h) \sim C_1 h^{k_1+1}, \qquad e_2(h) \sim C_2 h^{k_2+1}. \tag{4.19}$$

Given the additive nature of the errors, the overall order of accuracy of the scheme k is given by the minimum of the two orders

$$k := \min\{k_1, k_2\}. \tag{4.20}$$

Under the assumptions of well-definiteness of the governing matrices, error measures e_1, e_2 do apply to linear structural dynamics as a whole and not only to models for which modal expansion applies. Nonetheless, tractability matters encourage the use of a single degree of freedom model if the accuracy is to be assessed analytically. In that case, the treatment of polynomial and periodic loadings can be streamlined. If other configurations are to be assessed, the numerical route remains the fastest and most versatile one. The convolution product is then preferably computed using adaptive quadrature with stringent tolerances to reach error levels close to machine epsilon. A linear regression of the error components versus the timestep, after logarithmic transformation, provides approximations to k_1, k_2, C_1, C_2.

We combine both analytical and numerical results to assess the accuracy of the scheme defined by equation (4.4). Considering the mass-normalized harmonic single degree of freedom oscillator ($\mathbf{M} = 1, \mathbf{C} = 2\zeta\omega_0, \mathbf{K} = \omega_0^2, \mathbf{f} = \sin\omega t, \omega \neq \omega_0$), a closed-form expression of the matrix exponential can be derived. It reads

$$\mathrm{e}^{\mathbf{F}t} = \mathrm{e}^{-\zeta\omega_0 t} \begin{pmatrix} \cos\omega_d t + \frac{\zeta}{\sqrt{1-\zeta^2}}\sin\omega_d t & \frac{1}{\omega_d}\sin\omega_d t \\ -\frac{\omega_0}{\sqrt{1-\zeta^2}}\sin\omega_d t & \cos\omega_d t - \frac{\zeta}{\sqrt{1-\zeta^2}}\sin\omega_d t \end{pmatrix}, \tag{4.21}$$

with $\omega_d = \omega_0\sqrt{1-\zeta^2}$; subcritical damping is assumed, *i.e.*, $\zeta \in [0, 1)$. Also, given the trigonometric form of its entries, the convolution product entering the definition of e_2 can be expressed as

$$\int_0^h \mathrm{e}^{\mathbf{F}(h-t)} \begin{pmatrix} 0 \\ f(t) \end{pmatrix} \mathrm{d}t = \begin{pmatrix} \frac{1}{2\mathrm{i}\omega_d}\left(H^+[f] - H^-[f]\right) \\ \frac{-\zeta+\mathrm{i}\sqrt{1-\zeta^2}}{2\mathrm{i}\sqrt{1-\zeta^2}}H^+[f] + \frac{\zeta+\mathrm{i}\sqrt{1-\zeta^2}}{2\mathrm{i}\sqrt{1-\zeta^2}}H^-[f] \end{pmatrix}, \tag{4.22}$$

where

$$H^{\pm}[f] = \int_0^h \mathrm{e}^{(-\zeta\omega_0 \pm \mathrm{i}\omega_d)(h-t)} f(t)\,\mathrm{d}t, \tag{4.23}$$

with $\mathrm{i} := \sqrt{-1}$. Given the linearity of the integral operator, periodic and smooth functions can be treated by Fourier and Taylor series expansion, on the basis of the

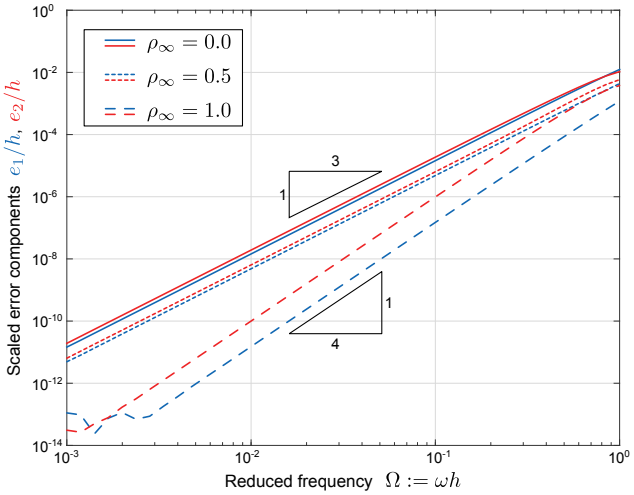

Figure 4.2: Numerical evaluation of the error orders k_1, k_2 for the DE^3 scheme. External loading is considered harmonic, $f = \sin \omega_0 t$. Parameters: $(\omega_0, \zeta, \omega) = (1, 0.1, 2)$.

following results

$$
\begin{aligned}
H^{\pm}[\mathrm{e}^{i\omega t}] &= \frac{1}{\mathrm{i}(\omega \mp \omega_d) + \zeta\omega_0} \left(\mathrm{e}^{\mathrm{i}\Omega} - \mathrm{e}^{-\zeta\Omega_0 \pm \mathrm{i}\Omega_d}\right), \\
H^{\pm}[t^n] &= \gamma\left(n+1, -\zeta\Omega_0 \pm \mathrm{i}\Omega_d\right) \frac{\mathrm{e}^{-\zeta\Omega_0 \pm \mathrm{i}\Omega_d}}{\left(-\zeta\omega_0 \pm \mathrm{i}\omega_d\right)^{n+1}},
\end{aligned}
\tag{4.24}
$$

with $\Omega_0 := \omega_0 h, \Omega := \omega h, \Omega_d := \omega_d h$ and the incomplete gamma function $\gamma(n+1, x) := \int_0^x t^n \mathrm{e}^{-t} \mathrm{d}t$. The first result does not apply in the conditions of resonant excitation in the absence of damping, *i.e.*, when $\omega = \omega_0$ and $\zeta = 0$. Noting that $\sin \omega t = \mathrm{Re}(\mathrm{e}^{i\omega t})$, the above expressions can be used in combination with the numerical evaluation of the norms, for several values of the timestep h. This yields the curves of Figure 4.2 that confirm that the scheme is third-order accurate in the numerically dissipative setting ($k = k_1 = k_2 = 3$ when $\rho_\infty < 1$) and fourth-order accurate in the numerically conservative one ($k = k_1 = k_2 = 4$ when $\rho_\infty = 1$). In fact, series expansion of e_1, e_2 show that the leading-order term of the Maclaurin series is fourth-order and proportional to χ; it thus vanishes when conservative integration is used and the scheme gains one accuracy order.

4.2.2 Root-solving strategy

The second ingredient to event-driven integration is the root-solving strategy that encompasses three tasks: (*i*) the detection of events over the current timestep interval $[t_n, t_{n+1}]$, (*ii*) the accurate localization of events in case their occurrence has been detected and (*iii*) the identification of the next dynamics mode the system will experience so that piecewise-defined quantities can be updated.

Event detection and localization has become a standard feature on most solver packages for systems of first-order ordinary differential equations, e.g., [84]. Several approaches exist [85, 86, 87] but, mostly, advanced solvers exploit a continuous extension of the discrete solution to detect and localize events: a polynomial approximating with sufficient accuracy the continuous solution on the basis of the discrete one is constructed and used for event detection and localization [88, 89]. These prove best at balancing the responses to the two main challenges faced by root-solving [88]: robustness and efficiency. Procedures must indeed guarantee that events shall not be overlooked and that their localization can be performed with a reasonable computational effort. Nonetheless, to our best knowledge, no such continuous extensions exist for the schemes dedicated to the integration of the second-order equations of motion arising in mechanics and a general procedure had to be devised to integrate equation of motion (4.1) while tracking the occurrence of zeros of the m event functions (4.2). The one we propose is based on the continuous extension of the state variables using cubic Hermite interpolation and the driving of event localization past the point of event occurrence, so that improper mode switches are automatically avoided in (numerical) grazing situations. A loop on active events is used to handle multiple event occurrences.

Event detection

Let the event functions at times t_n, t_{n+1} be denoted by $\mathbf{q}_n, \mathbf{q}_{n+1}$ and their time derivatives by $\dot{\mathbf{q}}_n, \dot{\mathbf{q}}_{n+1}$; if they involve the velocity, the accelerations can be obtained from the equation of motion. Let also the time interval be mapped onto a parent domain by the linear transformation $\tau(t) := (t - t_n)/h$, with the current timestep $h := t_{n+1} - t_n$, so that $\tau \in [0, 1]$. On the parent domain, the interpolated event functions are then given

by

$$\begin{aligned}\tilde{\mathbf{q}}(\tau) := \mathbf{q}_n + \tau h\dot{\mathbf{q}}_n + \tau^2\left(-3\mathbf{q}_n - 2h\dot{\mathbf{q}}_n + 3\mathbf{q}_{n+1} - h\dot{\mathbf{q}}_{n+1}\right) \\ + \tau^3\left(2\mathbf{q}_n + h\dot{\mathbf{q}}_n - 2\mathbf{q}_{n+1} + h\dot{\mathbf{q}}_{n+1}\right),\end{aligned} \tag{4.25}$$

or $\tilde{\mathbf{q}}(\tau) = \sum_{i=0}^{3} \mathbf{a}_i \tau^i$. This continuous extension of the event functions is the backbone of the detection and localization of event occurrences as both procedures are based on its roots. It is also the source of possible numerical complications. The tilde notation has been introduced to underscore the fact that $\tilde{\mathbf{q}}(\tau)$ is an approximation to the time-continuous event functions $\mathbf{q}(\tau)$ that would be computed by the integration scheme upon variation of the integration timestep.

Given the third order of the interpolating polynomial, the number of its roots in the parent domain can take any value in $\{0; 1; 2; 3\}$. The event-detection step consists in detecting the presence of at least one root in the parent domain without necessarily computing the polynomial roots, for each event.

Sturm sequences [90] and the likes based on Vincent's theorem [91], which associate the presence of polynomial roots in arbitrary intervals to sign changes in specific sequences, are well known means for the detection of roots of univariate polynomials in selected intervals. They are commonly implemented in Computer Algebra Systems (CAS) in combination with exact arithmetic. However, when combined to floating-point arithmetic, these become more difficult to use not to say unreliable when badly scaled polynomials are to be assessed; see for instance the specific iterative treatment proposed by Suzuki and Sasaki [92] to regularize Sturm sequences in such cases.

By design of the proposed root-solving algorithm, there will be numerous situations where badly scaled and degree degenerate polynomials will be expected. A simple example being when the timestep h becomes very small as compared to the characteristic timescale of the oscillations, for the system trajectory is almost linear in that setting. Therefore, an alternative technique based on a sign analysis of the interpolating polynomial and its derivative is used, instead. Algorithm 4.2 gives the rationale behind the detection procedure. A single event function is considered in this description; multiple event functions are treated by embedding the procedure in a loop over all active functions. If the event function changes sign across the time interval, there is at least one root in the parent domain, for the event function is assumed continuous; event localization is requested. If the function does not change sign across the interval, then there

Algorithm 4.2 Event-detection procedure.

Assumption: $q(0) \neq 0$

```
if q(0)q(1) < 0
    Proceed with event localization
else
    Compute abscissa of extrema τ_{1,2} = (−a_2 ± √(a_2 − a_1 a_3))/(3a_3)
    if ∃i ∈ {1,2} : τ_i ∈ (0,1) & q(0)q̃(τ_i) < 0
        Proceed with event localization
    else
        if q(1) = 0
            Event at t_{n+1}
        else
            No event occurrence over the current timestep
        end if
    end if
end if
```

Algorithm 4.3 Event-localization procedure.

```
Compute roots of active event functions in (t_n, t_{n+1}] → h_evt
while true
    Compute iteration time t_k := t_n + f(h_evt, k) > t_n + h_evt
    Compute state at iteration time, x(t_k)
    Compute active event functions at iteration time, q(t_k)
    Detect occurrence of events in (t_n, t_k) using Algorithm 4.2
    if any
        Compute roots of zero-crossing event functions → h_evt
        if any in (t_n, t_k − tTol)
            Proceed with additional iteration
        else
            if all events in [t_k − tTol, t_k) verify |q(t_k) + sign(q_n)qTol| < qTol
                return (events are localized)
            else
                Proceed with an additional iteration
            end if
        end if
    else
        No event occurs on (t_n, t_k), accept x_k and proceed with next increment
    end if
end while
```

might be zero or two roots. Occurrence of the roots is detected by comparing the sign of $q(0)$ to that of the extrema of $\tilde{q}$ provided they exist and are located in the parent domain. If there is a sign change, then occurrence is expected and event localization is requested. If not, either there is no event occurrence on the given time interval or $q(1) = 0$, in which case the end of the timestep coincides with the event occurrence.

Event localization

Upon detection of the possible occurrence of events over the current timestep, the event-localization module is called. Its purpose is to accurately compute the time of occurrence of the earliest event(s) and the associated state of the system; it must handle the possible simultaneous (up to a numerical tolerance) occurrence of events. The proposed localization procedure is iterative and relies on the combination of a root-solving module that computes the zeros of the cubic interpolation polynomials and a relaxation scheme that attempts to force event occurrence.

To avoid any robustness issue, the root-solving module is based on the numerical computation of the roots of cubic polynomials rather than on Cardano's analytical formula; the latter, indeed, proves sensitive to degree degeneracy and, in floating-point arithmetic, to error propagation in the computation of the intermediate coefficients defining the polynomial roots [93]. Two formulations are used.

For degree-degenerate situations, *i.e.*, $|a_3| < \texttt{degTol} \ll 1$ where `degTol` is an arbitrarily chosen tolerance, the companion eigenvalue formulation proposed by Corless et al. [94] is used; it is based on the barycentric representation of the Hermite interpolant. Following that formalism, the roots of the cubic approximant are given by the generalized eigenvalues

$$\bar{\boldsymbol{\tau}} := \{\bar{\tau} \in \mathbb{C} : |\bar{\tau}\boldsymbol{\Upsilon}_1 - \boldsymbol{\Upsilon}_0| = 0\}, \tag{4.26}$$

where

$$\boldsymbol{\Upsilon}_0 := \begin{pmatrix} 0 & & & & q(0) \\ 1 & 0 & & & \dot{q}(0) \\ & & 1 & & q(1) \\ & & 1 & 1 & \dot{q}(1) \\ -2 & -1 & 2 & -1 & 0 \end{pmatrix}, \qquad \boldsymbol{\Upsilon}_1 := \begin{pmatrix} 1 & & & & \\ & 1 & & & \\ & & 1 & & \\ & & & 1 & \\ & & & & 0 \end{pmatrix}, \tag{4.27}$$

with $\dot{q}(\tau) := \frac{\mathrm{d}q}{\mathrm{d}\tau}$. The two infinite spurious eigenvalues consequent to the formulation are obviously to be discarded. The eigenvalue problem can be solved using any appropriate library.

Alternatively, in non-degenerate situations, *i.e.*, $\texttt{degTol} < |a_3|$, the fitting procedure proposed by Strobach [95] is employed. It is based on the rewriting of the event function in the normalized form

$$\tilde{q}_0(\tau) := \frac{q_0}{a_3} = (\tau^2 + x_1\tau + x_2)(\tau + x_3) \tag{4.28}$$

and the identification of coefficients $x_i, i \in \{1; 2; 3\}$, by a combination of analytical results and numerical methods.

Real roots of the cubic interpolants that belong to the parent domain $[0, 1]$ correspond to approximations of the times of event occurrence as predicted by the integration scheme. An iterative procedure is therefore wrapped around the polynomial root-solving module so that events can be accurately localized. Key to the procedure is the treatment of multiple events in parallel by looping over all active event functions as well as the driving of the iterate time past the point of predicted earliest event occurrence $t_n + h_{\mathrm{evt}}$. The latter feature plays an important role as regards the robustness of the procedure and greatly simplifies the identification of the next dynamics mode; the idea has been borrowed from Birta et al. [96]. Its main steps are given in Algorithm 4.3. When events are detected, their expected time of occurrence is numerically computed as the roots of the interpolation polynomial. On the basis of the timestep to the expected earliest event occurrence, h_{evt}, the iteration time $t_k > t_n + h_{\mathrm{evt}}$ is computed as a function of h_{evt} and the iteration number. It approaches $t_n + h_{\mathrm{evt}}$ by the right as the number of iterations increases, so as to force event occurrence prior to its localization. The state and the event functions are then computed at t_k. Subsequent to this update, the time interval is divided into three non-overlapping sets

$$(t_n, t_{n+1}] := (t_n, t_k - \texttt{tTol}) \cup [t_k - \texttt{tTol}, t_k) \cup [t_k, t_{n+1}], \tag{4.29}$$

and the presence of events assessed in (t_n, t_k) using the event-detection module. If any zero-crossing is detected in $(t_n, t_k - \texttt{tTol})$, an additional iteration is requested. Otherwise, if at least one event is located in $[t_k - \texttt{tTol}, t_k)$ and all events in that interval verify the residual condition

$$|q(t_k) + \mathrm{sign}(q_n)\texttt{qTol}| < \texttt{qTol} \tag{4.30}$$

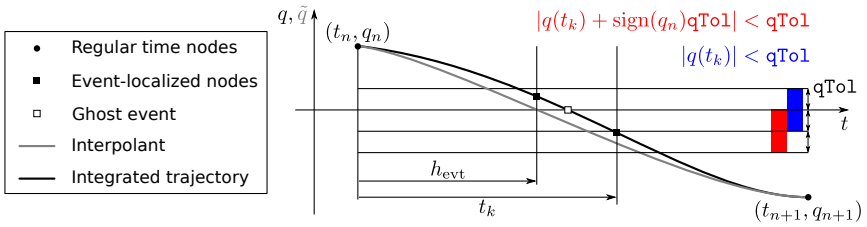

Figure 4.3: Avoiding numerical accumulation by driving event localization past the event occurrence.

that expresses a change of sign with respect to the event function at t_n, they are returned as localized. Otherwise, an additional iteration is requested. If no event is detected in (t_n, t_k), then the state computed at t_k is accepted as is and the time integration proceeds with the next increment, taken from $(t_k, \mathbf{x}_k)$. Tolerance parameter `tTol` has been introduced to increase the accuracy of the event-localization procedure in near-grazing situations for which the time derivative of event functions has a limited magnitude. In regular situations the convergence process is controlled by `qTol` [38].

The force of the proposed procedure is that it automatically prevents numerical accumulation, also known as *discontinuity sticking* in the literature [89, 97], and is robust to numerical grazing.

Figure 4.3 illustrates the concept of numerical accumulation that may arise with a root-finding procedure that is based on the common residual magnitude convergence criterion and how it is avoided when condition (4.30) is used. For this, we consider a single event function with a single zero-crossing over the timestep, with $q_n > 0$ and $q_{n+1} < 0$. If the regular convergence criterion based on the residual magnitude is used for event localization, it may well be that the event is localized before its occurrence, in which case $q_n q(\bar{t}) > 0$, $\bar{t} := t_n + h_{\mathrm{evt}}$. As the derivative of the event function is negative, $\dot{q}(\bar{t}) < 0$, a zero-crossing of the event function is to be expected over the next time increment. This crossing corresponds to a ghost of the previously localized event; it can lock the integration procedure on a single mode transition if it is not rejected by some strategy. Indeed, an indefinite detection and localization of ghost events could take place if the event function residual does not change sign throughout the localization procedure. The best solution to a problem being, when possible, to avoid creating the problem, forcing event localization past event occurrence by combining the convergence

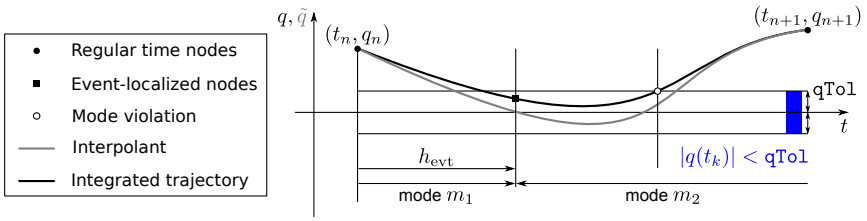

Figure 4.4: Illustration of numerical grazing and dynamics mode violation.

criterion (4.30) and the relaxation procedure defining the iterate times is likely the most robust answer to numerical accumulation and why we have chosen it.

Driving event-localization past event occurrence, in combination with the acceptance of all computed points prior to event occurrence, also enables the algorithm not to fall into the trap of numerical grazing that arises from the approximate nature of $\tilde{q}(t)$. As shown in Figure 4.4, there may be situations were the system trajectory comes close to the event occurrence condition but, in fact, never reaches it. In such situations, the interpolant might lead to the detection of events that actually never occur. The localization of these events with the regular residual magnitude convergence criterion can then lead to improper dynamics mode transitions. Such situations are, also, automatically avoided by driving event-localization past event occurrence. Indeed, in this illustrative example, the proposed procedure would not consider the event detected at $t + h_{\text{evt}}$ as localized, accept this point as part of the regular trajectory and take a new increment. Even if an event was detected during this new increment, it would not be localized as the trajectory never crosses the condition $q = 0$.

4.2.3 Mode switching

The general problem of mode switching typically requires the resolution of a decision problem, as is, for instance, the case when multiple contacts occur simultaneously in multibody dynamics [41, Ch. 8.5]. Under the assumption of independent event functions, things considerably simplify. To each event occurrence corresponds a single alteration to the system dynamics. Accordingly, the update of the piecewise-defined quantities entering (4.1) is easily conducted by tracking the ID of the localized events.

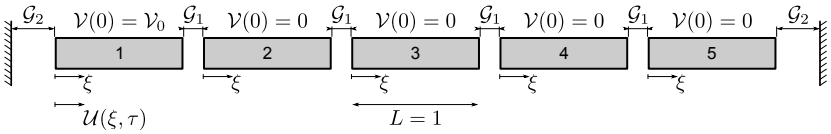

Figure 4.5: Simplified model of Newton's cradle with $N = 5$ identical bars of unit length. Gaps between all bars, $\mathcal{G}_1$, are taken identical and so is it for the gaps with the rigid side walls, $\mathcal{G}_2$. Bar 1 has initial velocity $\mathcal{V}_0$ while all other ones are at rest. The gap parameters verify the condition $\mathcal{G}_1, \mathcal{G}_2 > \mathcal{V}_0$. Wave propagation speed is unity. The bar IDs have been dropped for readability.

4.2.4 Validation

Several test problems have been considered to validate the event-driven integration procedure; see [38] for examples involving unilateral contact elastic constraints. We only report the results of the simplified Newton's cradle benchmark problem that we have developed for testing purposes. Its analytical solution is derived in Appendix D; it can serve as a reference problem to compare methods dedicated to the simulation of wave propagation in multibody contacting elastic solids. It also provides elements for the choice of numerical parameters relative to the method.

Problem definition and analytical solution

The present benchmark problem is inspired from the so-called Newton's cradle, a device that consists of collinear identical cable-suspended steel balls that, after initiation of a first impact, collide in a theoretically infinite manner through conservation of both momentum and energy. Far from the original model that comes with its lot of complexities due to the possibility of multiple impacts occurring simultaneously, see for instance [98], the one we consider is an academic simplification. Rather than working with spherical impactors, we consider N identical slender elastic bars with constant properties along their main axis. Figure 4.5 illustrates this conservative system for $N = 5$.

Given the slenderness and the elasticity of the bars, we assume that their motion is ruled by the 1-dimensional wave equation. After normalization, the problem is characterized by parameters $\mathcal{G}_1, \mathcal{G}_2, \mathcal{V}_0$; that is, the initial gap between the bars, the initial gap between extreme bars and the rigid side walls, and the initial velocity of bar 1, all other bars being initially at rest. The wave propagation speed and the bar lengths are

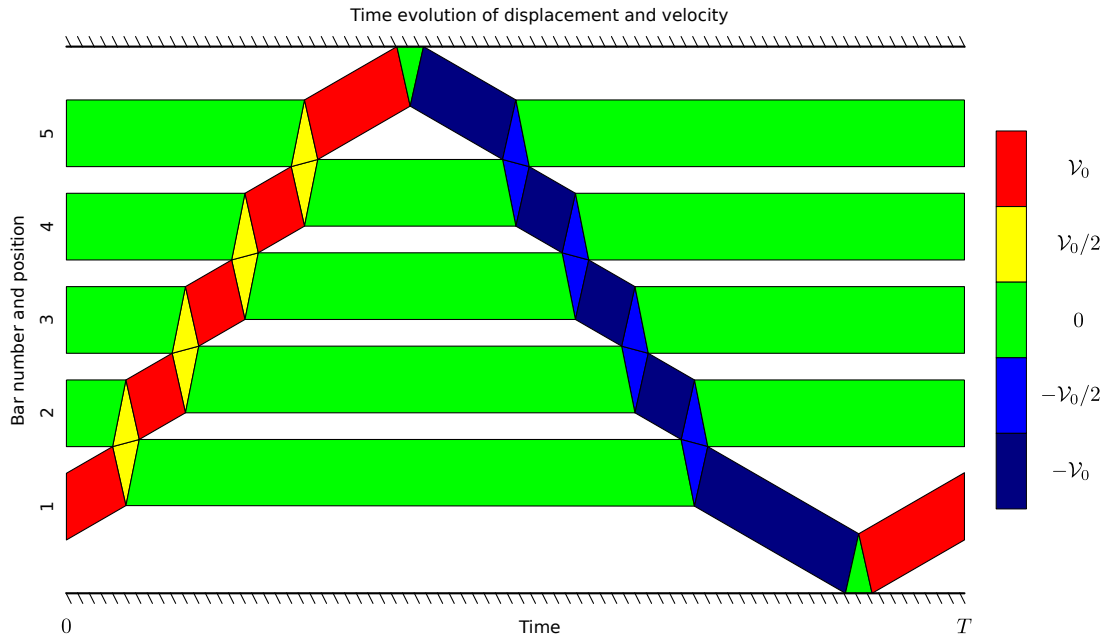

Figure 4.6: Motion of the system for $N = 5$ over one period T. Momentum propagates from initially moving bar 1 via the successive interaction phases, to eventually return to bar 1 that recovers its initial state given the system geometry, the problem conservativeness, and the identical nature of the bars.

set to unity. Upon enforcement of the conditions $\mathcal{G}_1, \mathcal{G}_2 > \mathcal{V}_0$, persistent contact phases are guaranteed to occur sequentially.

The analytical solution has been derived under this assumption. Given the problem definition, it is periodic with period T. Figure 4.6 illustrates the system response over one period for $N = 5$. Time is displayed along the horizontal axis while the vertical axis represents the bar positions; velocity information is superimposed using colors. Motion is propagated from one bar to the other through sequential contact phases. A single bar is moving at a time except when bar/bar persistent contact phases take place. Bars involved in contact phases experience deformations; outside contact phases, they have uniform velocity and behave like rigid bodies.

An interesting perspective of the problem is thus that of the rigid body motion that can be associated with the spatial average of the bar motions

$$\langle \mathcal{U}_i \rangle_\xi (\tau) := \int_0^1 \mathcal{U}_i(\xi_i, \tau)\, d\xi_i, \qquad \langle \mathcal{V}_i \rangle_\xi (\tau) := \int_0^1 \mathcal{V}_i(\xi_i, \tau)\, d\xi_i; \tag{4.31}$$

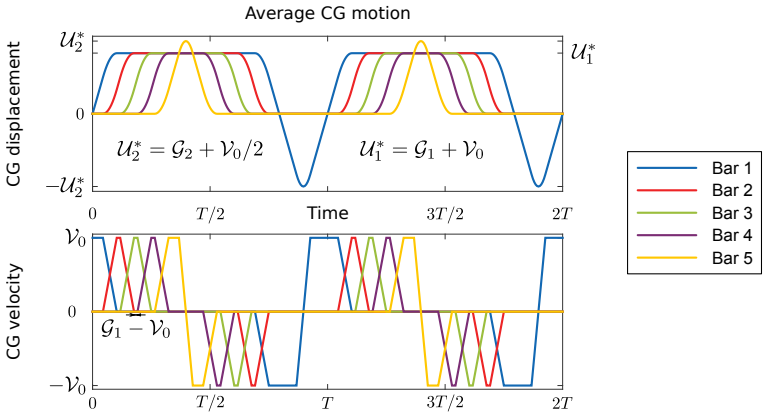

Figure 4.7: Average motion of the bar centers of gravity over two periods, for $N = 5$. Scaling corresponds to $(\mathcal{V}_0, \mathcal{G}_1, \mathcal{G}_2) = (0.05, 0.075, 0.0125)$.

index i represents the bar ID. Averaging brackets corresponding to space and time are differentiated by the appended subscript, with ξ for space, τ for time, and ξ, τ for averaging in both space and time. It is depicted in Figure 4.7, still for $N = 5$ bars, over a duration of two periods; it is to be viewed in parallel with Figure 4.6.

Numerical results

Following the finite element discretization approach used to transform the continuous elastic two-body model into semi-discrete equations of motion, the benchmark problem can be cast in the form of the model problem (4.1), with $N+1$ event functions given by the gap functions associated with each contact interface. The advocated event-driven integration strategy can then be used to compute an approximation to the exact solution.

To compare the numerical response with the analytical one, the following dimensionless error measure is introduced

$$E(T) = \frac{1}{N} \sum_{i=1}^{N} \left(\frac{\left| \langle \boldsymbol{\mathcal{U}}_i \rangle_\xi - \langle \mathcal{U}_i \rangle_\xi \right|}{\sqrt{\mathcal{G}_1 \mathcal{G}_2}} + \frac{\left| \langle \boldsymbol{\mathcal{V}}_i \rangle_\xi - \langle \mathcal{V}_i \rangle_\xi \right|}{\mathcal{V}_0} \right), \tag{4.32}$$

where the numerical approximations are given by

$$\langle \boldsymbol{\mathcal{U}}_i \rangle_\xi(\tau_n) := \mathbf{1}_i^T \mathbf{M} \boldsymbol{\mathcal{U}}_n, \qquad \langle \boldsymbol{\mathcal{V}}_i \rangle_\xi(\tau_n) := \mathbf{1}_i^T \mathbf{M} \boldsymbol{\mathcal{V}}_n. \tag{4.33}$$

Again, left-multiplication by $\mathbf{1}_i$ corresponds to a summation operation on the degrees of freedom pertaining to body i. Convergence of this error measure with respect to mesh

refinement is assessed in Figure 4.8 that also shows the influence of the contact stiffness. The simulation parameters are defined as follows:

- Model parameters are set to $(N, \mathcal{V}_0, \mathcal{G}_1, \mathcal{G}_2) = (5, 0.05, 0.125, 0.075)$.
- Some numerical dissipation is introduced via the time integration procedure by setting $\rho_\infty = 0.9$.
- The contact stiffness is defined proportional to the largest entry of the global stiffness matrix, $\kappa_C = \hat{\kappa}_C \max(\max(\mathbf{K}))$. For linear and quadratic elements, the largest entry of the stiffness matrix is given by $\max(\max(\mathbf{K})) = 2(d/N - 1)$ and $\max(\max(\mathbf{K})) = (8/3)(d/N - 1)$, respectively, where d is the total number of degrees of freedom in the semi-discrete model. Thus, at equal scaling factor, the contact stiffness increases with mesh refinement.
- The nominal timestep for the simulation is chosen so that a unit Courant number is achieved. As, given the problem scaling, it is equal to the internodal distance $(d/N - 1)^{-1}$, the timestep decreases with mesh refinement.
- Tolerances for the event-localization procedure are set to $(\texttt{qTol}, \texttt{tTol}, \texttt{degTol}) = (10^{-6}, 10^{-4}, 10^{-12})$.

Results show that, at constant contact stiffness scaling factor $\hat{\kappa}_C = 0.1$, the convergence rate is slightly above (below) 1 when linear (quadratic) elements are used. Other configurations lead to slower convergence rates. Furthermore, at equal number of degrees of freedom, linear elements provide a slightly more accurate solution than quadratic elements.

Additional insight into the numerical response is given in Figure 4.9 that depicts the average response of the 5 bars in terms of displacement and velocity, as well as the evolution of the contact response through the gap functions and the contact forces. The evolution of the system energies is also given; relation (4.9) was used for their computation. The results correspond to simulation parameters $(p, d/N, \hat{\kappa}_c) = (1, 250, 0.1)$. Apart from a phase discrepancy that is visible at the level of the end displacement of body 1, $\langle \boldsymbol{\mathcal{U}}_1 \rangle_\xi(T)$, and on the gap functions 1 and 2, the average numerical response matches well the exact response given in Figure 4.7. The evolution of the contact response shows

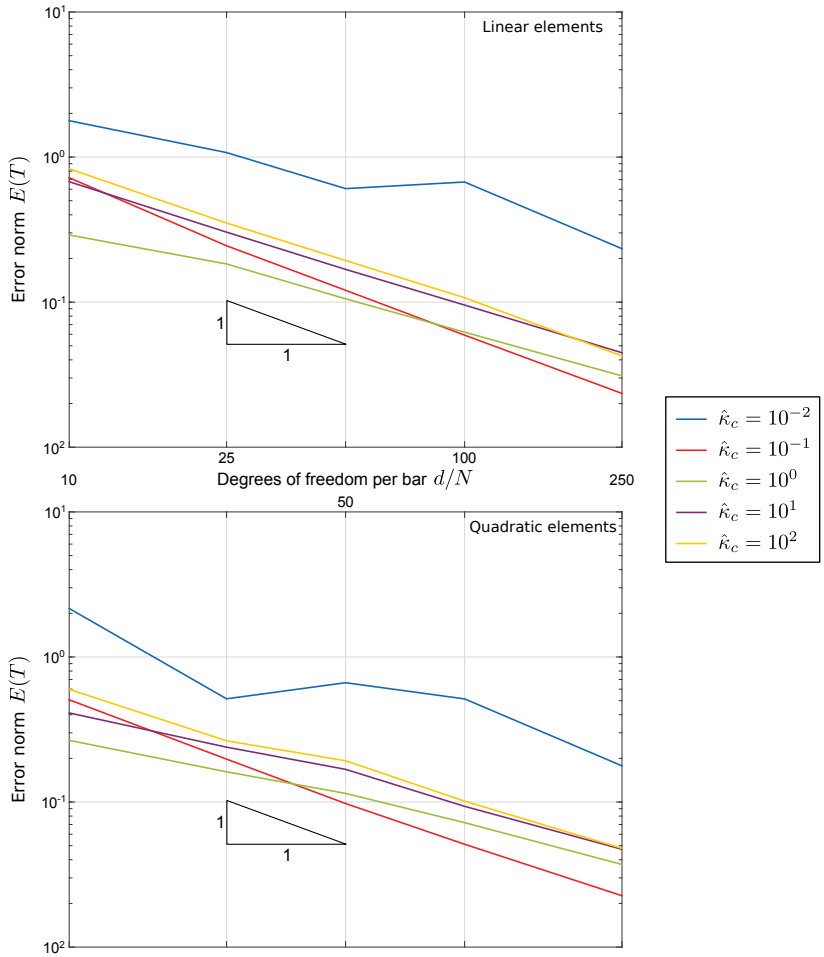

Figure 4.8: Convergence analysis for linear (top) and quadratic (bottom) elements on the basis of error measure (4.32), for several values of the contact stiffness scaling factor.

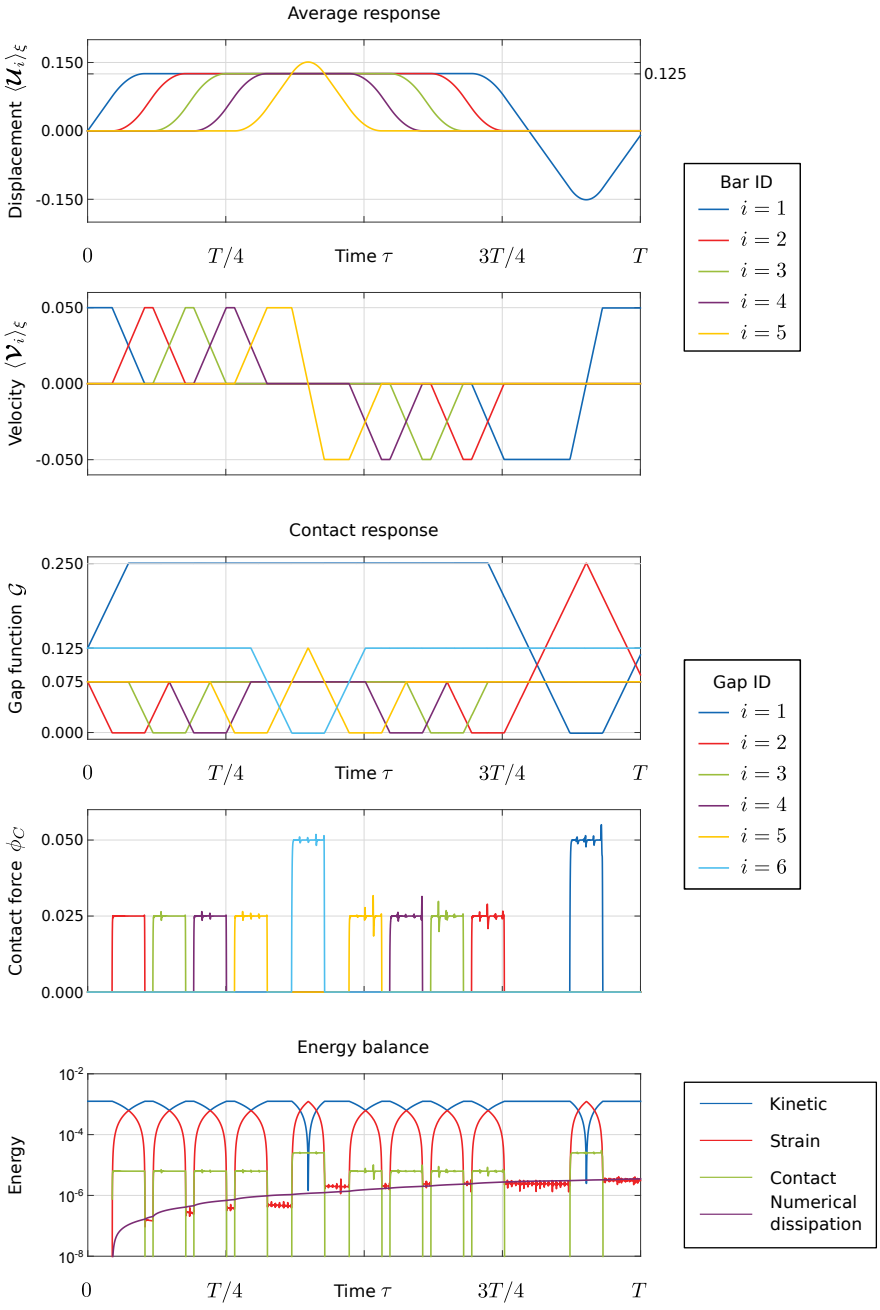

Figure 4.9: Time evolution of the system response with, from the top to the bottom plot: the average body displacements, the average body velocities, the gap functions, the contact forces and the distribution of energy in the system. Simulation parameters: $(p, d/N, \hat{\kappa}_c) = (1, 250, 0.1)$.

that, even with a limited contact stiffness, the interpenetration remains tolerable. Numerics show a magnitude of 10^{-3} units of length, where a single unit corresponds to the bar length, given the problem normalization. Also, the limited contact stiffness prevents the contact interaction from overexciting high-frequency oscillations, as can be noticed by the contact force response. The exact contact force that corresponds to the horizontal plateau is well captured but for limited spikes that correspond to wave fronts traveling in the bars; their spacing coincides with the interbody gap $\mathcal{G}_1$. The reduction of these numerical perturbations is addressed in the next section. The evolution of energetic quantities in the system indicates that: (i) the amount of numerical dissipation remains well below the characteristic energy of the system defined as the initial kinetic energy, and (ii) the combination of the penalty method with the proposed event-driven integration procedure is stable. It is, indeed, well-known that the penalty method can be the source of energetic instabilities in dynamic finite element computations for it does not ensure a zero net work of the contact force over a closure/opening cycle of the contact interface [55, 77, 99, 100]. These are automatically eliminated by the event-driven strategy provided the event-localization `qTol` is sufficiently small; indeed, the energy drift associated with the handling of unilateral constraints is directly proportional to the tolerance [38].

4.2.5 Taming spurious oscillations

Hyperbolic problems are known to propagate discontinuities in time and space. A simple example is the discontinuous velocity field following the collinear longitudinal impact of two identical bars; see equations (D.2)-(D.3). Such discontinuities are a source of trouble to numerical methods that typically assume some degree of continuity of the integrated fields. Indeed, jump discontinuities correspond to infinite frequency signals and can be captured accurately neither in space nor in time given the finite resolution of the meshes. They usually result in the occurrence of spurious oscillations in the neighborhood of the discontinuities: the Gibbs oscillations.

The control of these spurious oscillations is vital to simulating percussive drilling. Even though they are originally localized at jump discontinuities, Gibbs oscillations tend to diffuse around the moving discontinuity under the action of numerical dispersion. As the bit/rock interaction law notably depends on the nodal velocity at the bit/rock

interface, to not tame these oscillations is a guarantee of garbage results.

A wealth of methods have been devised to address the need for non-oscillatory solutions in the presence of high gradients and discontinuities, *e.g.*, shock-capturing space-time finite elements [101, 102] or the reconstruction-based ENO [103] and WENO approaches [104], among others. Similarly, upwind-based methods locally add artificial viscosity to the original model. In these methods, the local dissipation is obtained by accounting for the characteristic wave-structure of the hyperbolic system, to some extent.

Following that approach, Banks and Henshaw [105] have proposed the UW1 scheme, a first-order accurate explicit scheme based on conservative finite differences for the second-order wave equation. Considering the scalar wave equation

$$\dot{v} = c_0^2 u'' + f, \qquad\qquad v = \dot{u}, \tag{4.34}$$

with constant source term f, and assuming a uniform mesh in the time and space directions with size h_t and h_x, the update equations read

$$\begin{aligned} v_i^{n+1} &:= v_i^n + h_t c_0^2 D_+ D_- u_i^n + \frac{h_t}{2} c_0 h_x D_+ D_- v_i^n + h_t f_n, \\ u_i^{n+1} &:= u_i^n + h_t v_i^n + \frac{h_t^2}{2} c_0^2 D_+ D_- u_i^n + \frac{h_t}{4} c_0 h_x D_+ D_- v_i^n + \frac{h_t^2}{2} f_n. \end{aligned} \tag{4.35}$$

Indices $i \in \{1; \dots; I\}$ refer to the spatial mesh and exponents $n \in \{0; \dots; N\}$ to the time mesh. Operator $D_+ D_- x_i := (x_{i+1} - 2x_i + x_{i-1})/h_x^2$ represents the second-order accurate centered finite difference approximation to the continuous second-order spatial derivative. The enforcement of spatial boundary conditions requires the alteration of the update equations at the boundaries of the spatial mesh. Adequate definition of the boundary conditions is required as they are known to affect the stability and the accuracy of the scheme [106, 107]; this can prove a delicate task in certain situations.

Interestingly, the modified equations associated with the update scheme (4.35), *i.e.*, the continuous partial differential equations that are actually solved by the update scheme [107, 108], show that upwinding dominantly acts as a damping term involving the second spatial derivative of the displacement/velocity field

$$\begin{aligned} \frac{\partial^2 u}{\partial t^2} &= c_0^2 \frac{\partial^2 u}{\partial x^2} + f + (1 - \mathrm{CFL}) \frac{c_0 h_x}{2} \frac{\partial^3 u}{\partial t \partial x^2} + \mathcal{O}\left(h_x^2\right) + \mathcal{O}\left(h_t^3\right), \\ \frac{\partial^2 v}{\partial t^2} &= c_0^2 \frac{\partial^2 v}{\partial x^2} + f + (1 - \mathrm{CFL}) \frac{c_0 h_x}{2} \frac{\partial^3 v}{\partial t \partial x^2} + \mathcal{O}\left(h_x^2\right) + \mathcal{O}\left(h_t^3\right), \end{aligned} \tag{4.36}$$

with CFL $:= c_0 h_t / h_x$. The integration scheme is stable provided the damping is positive; that is, for timesteps that verify the Courant-Friedrichs-Lewy condition CFL ≤ 1. Indeed, larger values would result in negative damping triggering instability.

Under the assumption of variable separation that underlies the dynamic finite element method, the first-order perturbation to the wave equation can then be interpreted as a viscous damping term whose viscosity is proportional to the stiffness matrix of the semi-discrete finite element problem. It is thus to expect that introducing proportional damping in the dynamic finite element simulation of longitudinal collinear impacts will have an effect similar to that of the upwinding term in the finite difference update scheme.

The smoothing effect of stiffness-proportional damping is confirmed in Figure 4.10; it compares the results of the event-driven integration procedure to the ones obtained with the upwind scheme UW1 and to the analytical response for the collinear longitudinal impact simulation of two identical rods. The nodal velocities of the two rightmost bar ends are shown, for several values of the damping parameter ζ_K that defines the viscous damping matrix as

$$\mathbf{C} = 2\frac{\zeta_K}{\omega_{cr}}\mathbf{K}; \tag{4.37}$$

where ω_{cr} is the largest eigenfrequency of the finite element mesh. Results are computed for CFL $= 1.0$ and CFL $= 0.5$ for the event-driven and upwind integration procedures, respectively. Integration parameter ρ_∞ is set to $\rho_\infty = 0.9$; however, at this low timestep, numerical damping remains negligible even with $\rho_\infty = 0.0$. It is observed that for $\zeta_K > 0.5$, spurious oscillations of the numerical solution vanish. In particular, for $\zeta_K = 0.5$, the solutions computed by the event-driven procedure and the explicit upwind scheme are identical in amplitude but differ slightly in phase. With both procedures, the velocity discontinuity is smeared across several timesteps. As a consequence, a velocity perturbation is observable after one round trip of the wave front in the bars (2 units of time). As the smearing of the velocity discontinuity increases with the proportional damping, the dip associated with this velocity perturbation logically increases as well. Mesh refinement does not lead to a sensible amelioration of the computed solution. The starting configuration for numerical simulations of percussive drilling can thus be set to roughly fifty elements over the piston body and damping parameter to $\zeta_K = 0.5$. The number of elements for the bit is chosen so that the two meshes have nearly equal

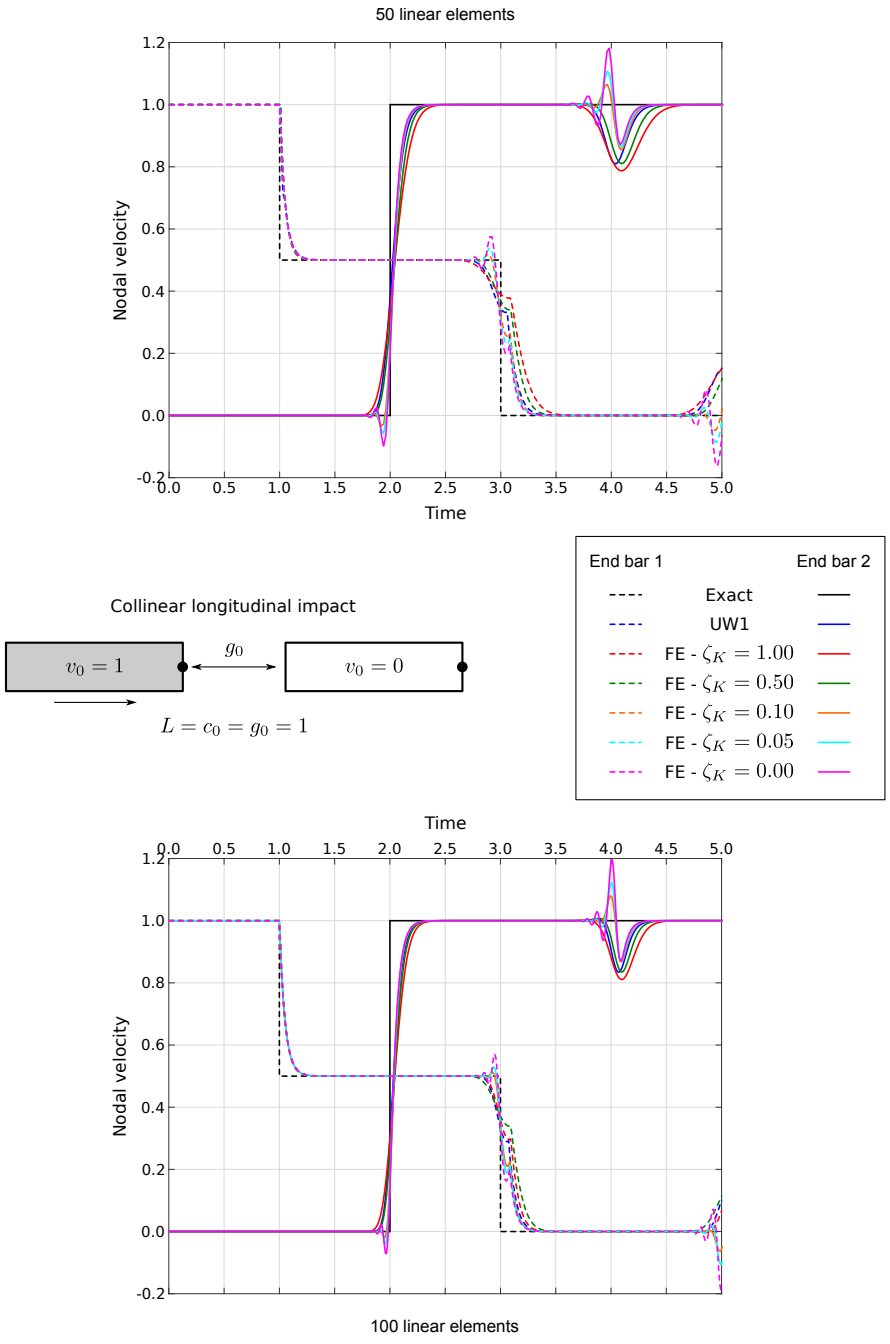

Figure 4.10: Proportional damping influence on the nodal velocity response in a collinear longitudinal impact, as computed by the event-driven integration procedure. The exact response as well as the numerical one obtained via the upwind scheme UW1 are given for reference and comparison.

element sizes.

On this specific example, the upwind scheme outperforms the event-driven integration procedure by a factor of two in terms of computational time. For the percussive drilling model, this trend is, nevertheless, inverted as stability and accuracy requirements lead to a severe reduction of the computational timestep. The upwind scheme is therefore not further considered in this thesis and all results presented in the sequel are computed via the event-driven integration procedure developed in this chapter.

Chapter 5

Numerical results

"An expert is a person who has made all the mistakes that can be made in a very narrow field."

N. Bohr

In this chapter, a preliminary analysis of the long-term responses of the two-body models is presented. In a comparative discussion, the period-1 stationary response of the models for a reference configuration is first considered. Then, the influences of the feed force, the unloading parameter of the bit/rock interaction law and the pressure law parameters are assessed via a parametric analysis.

5.1 Reference configuration

The reference configuration, which also served the definition of the numerical parameters used in Chapter 2, is given in Table 5.1. It is representative of a 3-in down-the-hole hammer/bit system; the pressure law parameters have been calibrated to ensure a percussive activation frequency in the range $[20, 25]$ Hz. The associated timescales are also given, as well as the dimensionless parameters; they have been rounded for convenience.

5.2 Numerical settings

All simulations presented in this chapter are based on an initialization of the system in a generalized free flight configuration. By this designation, it is meant that all contact

Table 5.1: Parameters for the reference configuration. Units are consistent with the set N, mm, g and ms.

Material param.	$\rho = 7850 \cdot 10^{-6}$	$E = 210 \cdot 10^{3}$	
Geometry	$A = 5500$	$L_p = 175$	$L_b = 201.25$
Static loads	$G = 10^{-2}$	$F_S = 2500$	
Pressure law	$D_1 = 40$	$F_0 = 3000$	
B/R interaction	$K_R = 750 \cdot 10^{3}$	$\gamma = 5$	
	$C_R = 10^{4}$	$W_R = 50$	
Timescales	$T_1 = 3.38 \cdot 10^{-2}$	$T_2 = 3.89 \cdot 10^{-2}$	$T_3 = 10$
	$T_4 = 1.08 \cdot 10^{-1}$	$T_5 = 6.30 \cdot 10^{-4}$	$T_6 = 1.07 \cdot 10^{-2}$
Length scales	$L_1 = 175$	$L_2 = 0.40$	
Timescale ratios	$\omega_{21} = 1.15$	$\omega_{41} = \sqrt{10}$	$\omega_{15} = 12.5$
Static loads	$\varpi = 2.5 \cdot 10^{-4}$	$\phi_S = 30$	
Pressure law	$\delta_1 = 100$	$\phi_0 = 40$	
B/R interaction	$\gamma = 5$	$\varrho = 4 \cdot 10^{-4}$	

interfaces are initially open, that the piston has downward uniform velocity and that the bit is uniformly at rest above the rock (no initial deformation). Thus, the initial gap at the piston/bit interface is given a positive value $\mathcal{G}_0 > 0$ and the bit/rock interaction law is initialized in the free flight mode with a positive bit/rock opening $\mathcal{P}_u > 0$. Also, in this initial setting, it is assumed that the pressure force acts in the downward direction, *viz.*, $\alpha = 1$. The definition of these conditions is such that a percussive activation is expected in the early simulation times.

The choice of the discretization parameters is justified in the convergence analysis of Appendix E, for each model. For the elastic model, uniform meshes are used on both the piston and the bit, with $n_p = 50$ elements on the piston and $n_b = \lceil \omega_{21} n_p \rceil = 58$ elements on the bit. The timestep is chosen such that CFL = 5. Event-detection parameters are set to $(\texttt{qTol}, \texttt{tTol}, \texttt{degTol}) = (10^{-6}, 10^{-4}, 10^{-12})$ and $\rho_\infty = 0$. The contact stiffness is set to $\kappa_C = \omega_{41}^2 \lceil \omega_{21} n_p \rceil / 5\omega_{21} \simeq 100.9$. For the rigid model, multiple fixed timesteps are used. They are set to $h = 1$ when the interaction law is in the free flight or in the standstill mode, to $h = 0.1$ when the interaction law is in the forward contact mode and to $h = 0.1/\sqrt{\gamma}$ when the interaction law is in the backward contact mode. Conservative

integration is used, *i.e.*, $\rho_\infty = 1$.

5.3 Period-1 solution for the reference configuration

Simulations show that an attractive period-1 solution exists for the reference configuration; it can be reached from generalized free flight initial conditions after a sufficiently long time integration of the model equations. The results presented hereafter are based on the initial settings $(\langle \boldsymbol{\mathcal{V}}_b \rangle_\xi, \mathcal{G}_0, \mathcal{P}_u) = (2.5, 10^{-1}, 10^{-2})$. Note that for the rigid body model, the spatial averaging operator is the identity operator, *i.e.*, $\langle \mathcal{U}_b \rangle_\xi = \mathcal{U}_b$ and $\langle \mathcal{V}_b \rangle_\xi = \mathcal{V}_b$.

Several projections of the periodic solutions are proposed, so that they can be observed from different standpoints. The initial time has been set to correspond to the initiation of percussive activation.

5.3.1 Elastic model

Figure 5.1 shows the time series of bit motion and of the bit/rock interaction force over one period of the limit cycle. Following the percussive activation, the bit experiences a sequence of drilling cycles and then converges to the standstill mode. In this phase, the bit/rock interaction force converges to the static load on the bit, $\phi_R \to \omega_{21}(1+\varphi_S)\varpi \simeq 9 \cdot 10^{-3}$. The motion experienced by the bit is, in qualitative terms, similar to the one of the drifting oscillator. The use of the descriptors introduced in Chapter 2 is possible but less convenient. Indeed, given the compliance of the bit, wave propagation affects the overall response at the bit/rock interface and drilling cycles can be interrupted due to a velocity reversal of the contact node. Such an effect is visible on the force/displacement response, close to the peak penetration reached after the percussive activation. The characterization of the solution from the behavior of the bit/rock interaction law is thus insufficient and graphical representations are preferably used.

Several other differences follow from the compliant behavior of the bit. For instance, percussive activation is not instantaneous; the bit average velocity $\langle \boldsymbol{\mathcal{V}}_b \rangle_\xi$ evolves continuously at its occurrence. Also, there is a phase lag between the average bit displacement $\langle \boldsymbol{\mathcal{U}}_b \rangle_\xi$ and the motion of the contact node that is at the bit/rock interface $\mathcal{U}_b(\omega_{21}, \tau) \simeq \mathbf{w}_R^T \boldsymbol{\mathcal{U}}$. Consequently, the bit is seen to evolve in forward contact mode

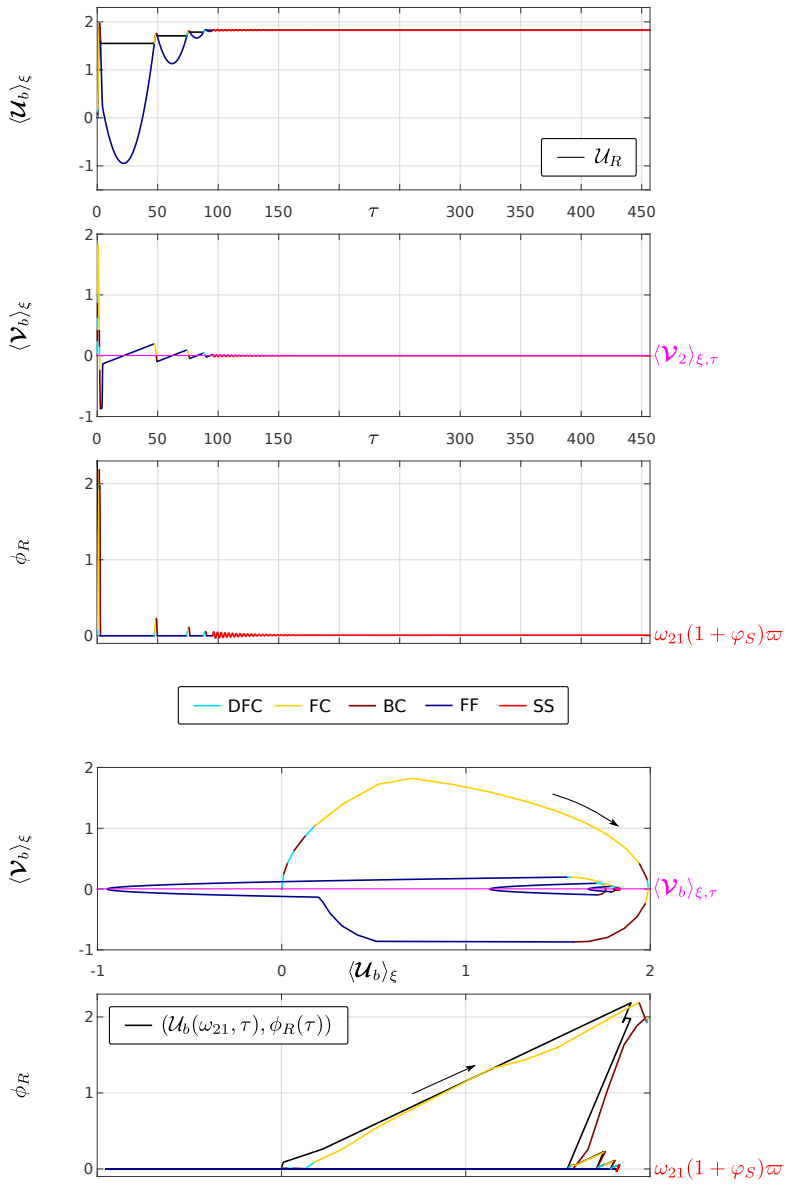

Figure 5.1: Elastic model – Period-1 solution corresponding to the reference configuration. Time series of the bit average motion and projections into the phase plane as well as into the interaction force space.

(backward contact mode) even though its average velocity is negative (positive). This phase lag is also visible on the force/displacement response of the bit/rock interaction force. When the interaction force is plotted versus the average bit displacement, fluctuations are visible around the bilinear backbone curve that is enforced at the contact node (black curve).

The multiscale nature of the model is clearly revealed by the time series of the bit average velocity and of the bit/rock interaction force. Interaction phases at the bit/rock and piston/bit interfaces are seen to have a short duration as compared to the period of the limit cycle that corresponds to the period of percussive activation ($\langle\omega_{34}\rangle_\tau \simeq 450$); see for instance the peaks of the bit/rock interaction force ϕ_R in its time series.

An interesting behavioral feature is revealed by the phase portrait of the bit average motion and further illustrated in the time series of Figure 5.2. It is the occurrence of two successive contact phases at the piston/bit interface. Following the percussive activation, the bit penetrates into the rock medium but bounces off after completion of the drilling cycle; this is in line with the analysis of the drilling cycle, conducted in Section 2.5. As, in this case, the normal gap velocity at the piston/bit interface is negative, $\dot{\mathcal{G}} < 0$, a second impact takes place. During that second contact phase, the bit acts as the collision driver and returns momentum to the piston, thereby accelerating it. This phenomenon, which is known to occur in physical devices, is in fact desired, for it enables the increase of the percussive activation frequency and, *in fine*, that of the overall drilling performance [109]. It also shows the need to include the piston dynamics in the model, for capturing such double impact percussive activations with the drifting oscillator model would be very much of a challenge.

In addition to the time series, Figure 5.2 shows the relative average motion of the system. The overall response is similar to the approximation that was derived in the definition of the pressure law, on the basis of a fixed bit; see Section 3.1. The change of relative acceleration coincides with the relative displacement crossing the pressure switch point, $\langle\boldsymbol{\mathcal{U}}_p\rangle_\xi - \langle\boldsymbol{\mathcal{U}}_b\rangle_\xi = -\delta_1 + \mathcal{G}_0$, and the two impacts are identified as the zones of abrupt velocity variations near zero relative displacement in the relative phase portrait. Positive relative displacements above the initial gap, $\langle\boldsymbol{\mathcal{U}}_p\rangle_\xi - \langle\boldsymbol{\mathcal{U}}_b\rangle_\xi > \mathcal{G}_0$, mainly result from the compliance of both bodies and, to a lesser extent, from the use of the penalty method to enforce the contact interaction; indeed, from the unit order of

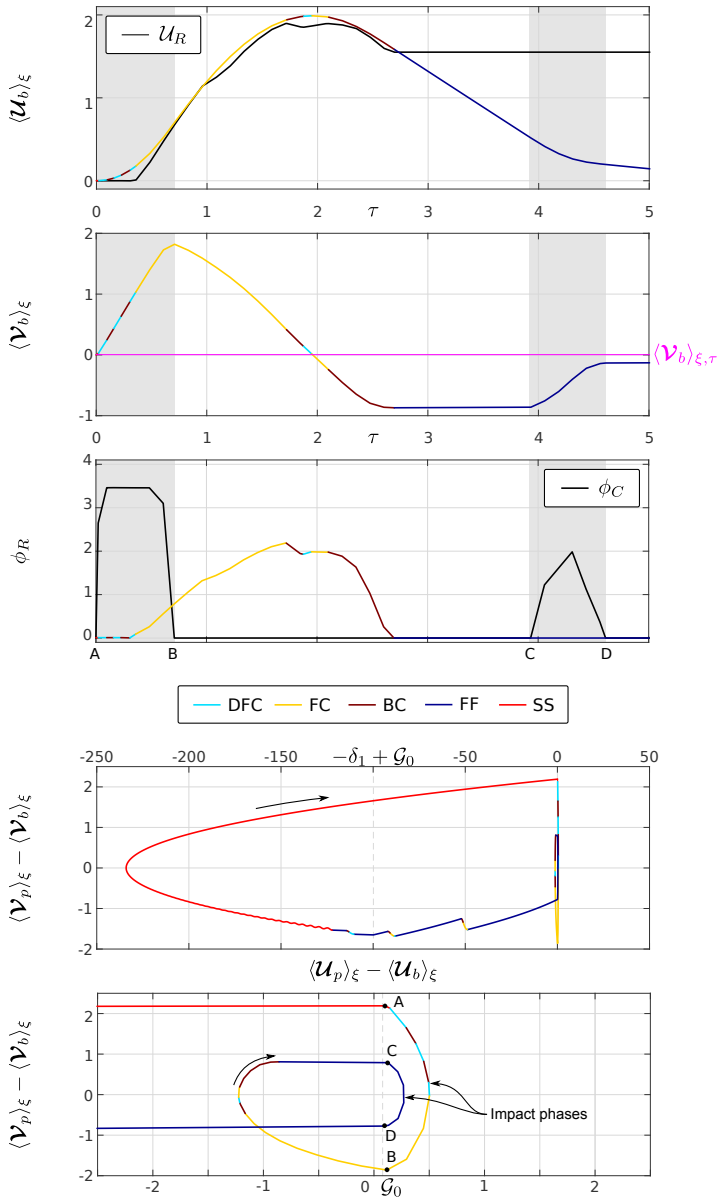

Figure 5.2: Elastic model – Period-1 solution corresponding to the reference configuration. Time series in the post-activation time range and phase portrait of the relative average motion. The gray shadings correspond to periods of closed contact at the piston/bit interface. Notation $\mathcal{U}_R$ indicates the displacement of the rock surface.

magnitude of the contact force and the magnitude of the contact stiffness, that of the interpenetration is readily evaluated as $\mathcal{G} = \mathcal{O}(10^{-2})$.

In Figure 5.3, the contributions to the energetic behavior of the system along the trajectory are analyzed. The energetic stability of the integration procedure is confirmed by the limited relative drift of the system total mechanical energy TE that expresses the balance of energy

$$\mathsf{TE} := \underbrace{(\mathsf{KE} + \mathsf{SE} + \mathsf{CE} + \mathsf{KBRI} + \mathsf{CBRI} + \mathsf{PD} + \mathsf{ND})}_{\text{Sinks}} - \underbrace{(\mathsf{GRAV} + \mathsf{FF} + \mathsf{PF})}_{\text{Sources}} = 0. \quad (5.1)$$

It is of order 10^{-9} and confirms that the event-detection tolerances are sufficiently tight. The evolution of the system kinetic (KE) and strain energies (SE) must be read in parallel with the motion of the system. After completion of the double impact percussive activation phase, the main contributor to the system kinetic energy is the piston. Therefore, the kinetic energy drop around $\tau = 250$ corresponds to the piston starting its descent towards the bit for the next percussive activation. The interactions of the bit with the piston and the rock generate waves that propagate in the mechanical system. The strain energy is seen to increase at the onset of interaction phases and decrease exponentially in-between them as a result of the proportional damping (PD) and the numerical damping introduced by the time integration scheme (ND). Along the limit cycle, the numerical dissipation introduced by the integration scheme and via proportional damping is limited to about 10% of the initial kinetic energy. Most dissipation takes place after the percussive activation. Four external forces act on the system: the weights due to gravity, the feed force, the pressure force, and the bit/rock interaction force that can be decomposed into its stiffness and viscous components. The works they do are respectively denoted by GRAV, FF, PF, KBRI, CBRI. As expected, the pressure force is the main driver to the penetration process as it is the principal source of energy in the system. Most of the consumed energy is by the stiffness component of the interaction force which concurs with our assumption of small energy barrier as compared to the energy delivered by the pressure force, *i.e.*, $\varrho \ll 1$. During persistent contact phases at the piston/bit interface, part of the system energy is stored in the numerical spring at the contact interface. This defines the contact energy (CE) that is totally reinjected in the system at the end of the contact phase, up to a quantity proportional to `qTol`; it is not represented in the figure.

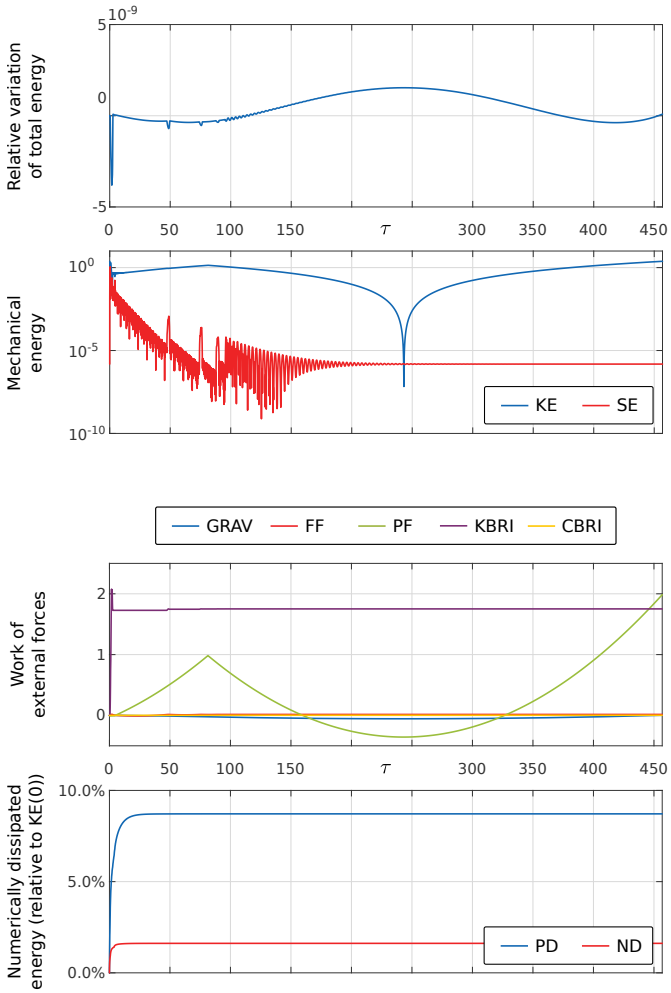

Figure 5.3: Elastic model – Energetic response of the system along the periodic trajectory. Acronyms stand for: kinetic energy (KE), strain energy (SE), works of the gravity force (GRAV), feed force (FF), pressure force (PF), bit/rock interaction force stiffness (KBRI) and viscous (CBRI) components, the energy dissipated by the proportional damping (PD), and the numerical damping (ND).

5.3.2 Rigid model

For the reference configuration, the response of the rigid model is qualitatively similar to that of the elastic model; see Figures 5.4-5.6. Accordingly, our comments focus on the main differences that can be observed between the responses of the two models. Three important ones are to be noted.

First, under the assumption of timescale separation, the percussive activation is instantaneous. This results in velocity jumps that are noticeable in the time series of the bit velocity and in the phase portraits. Also, following that assumption, the contact force between the piston and the bit is proportional to the Dirac delta function.

Second, the assumption of rigid bodies implies multiple differences between the model responses; we note two of them. As the motion of the bit center of gravity coincides with that of its extremity that is in contact with the rock, there is no phase lag between them and the average bit response is in phase with the bit/rock interaction law. Forward (backward) contact phases with negative (positive) bit velocities are thus not observed. In the absence of wave propagation, the large post-activation drilling cycle is not altered by the possible reversal of the contact node velocity; this alteration was indicative of the bit/rock interaction to be governed by a combination of rigid body dynamics and wave propagation in the elastic model, since $\omega_{41} \not\gg 1$.

Third, discontinuities of the piston and bit velocities cause jumps in the kinetic energy of the system. These variations, that occur at closures of the piston/bit contact interface, at the initiation of a new drilling cycle, and at the transition to the standstill mode, must be compensated by the external loads. After one period the instantaneous dissipation is of the order of 25% of the system kinetic energy prior to the percussive activation. Most energy is lost during the percussive activation which induces much larger energy discontinuities than those following the application of the energy barrier. Losses after the percussive activation can be interpreted as the instantaneous dissipation, at the end of the contact phase, of the strain energy remaining in the continuous problem serving the definition of the reset map. As conservative integration is used for the rigid model, these discrete energy variations are the only artificial energy losses in the system. They could thus be given an interpretation of external damping and should be viewed in parallel with the amount of energy dissipated by the numerical and proportional dampings that are introduced in the elastic model. In the present example, the external

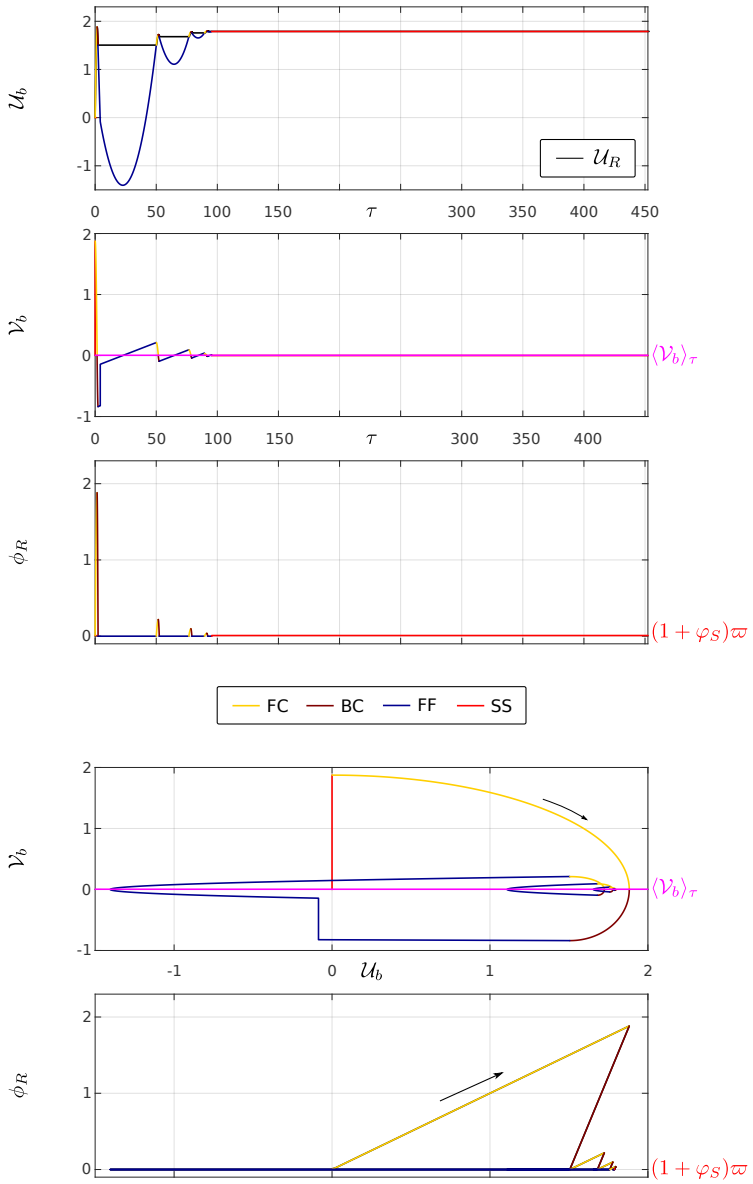

Figure 5.4: Rigid model – Period-1 solution corresponding to the reference configuration. Time series of the bit motion and projections into the phase plane as well as into the interaction force space.

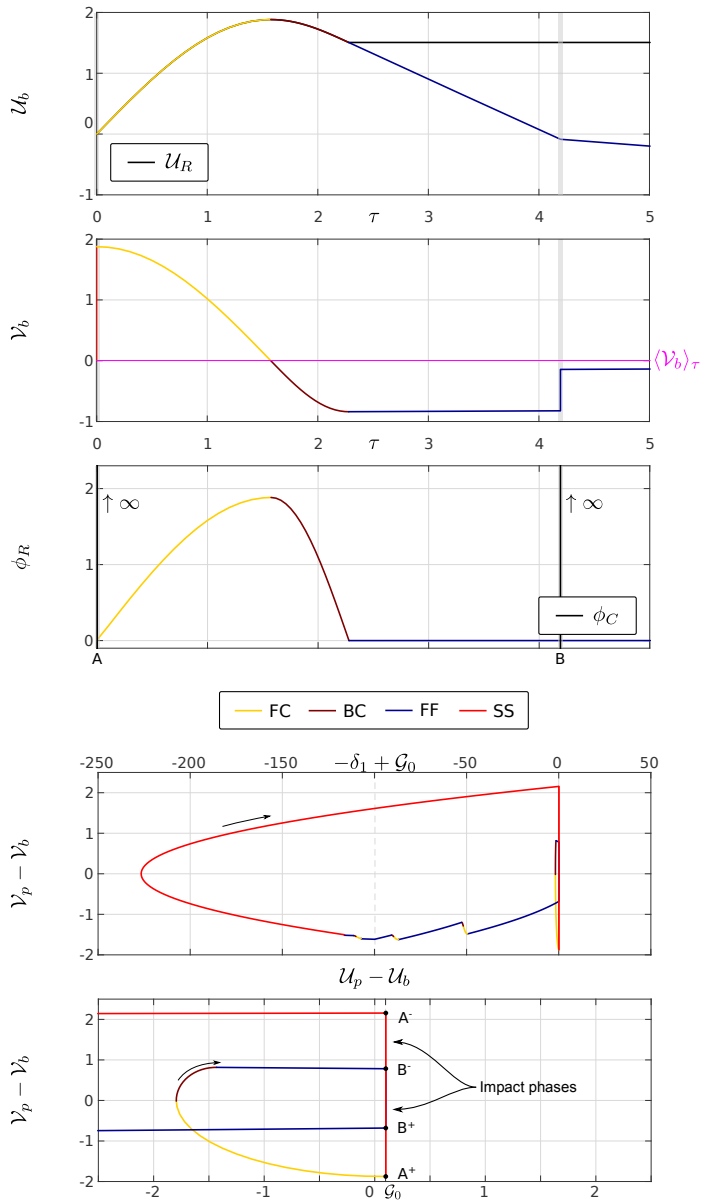

Figure 5.5: Rigid model – Period-1 solution corresponding to the reference configuration. Time series in the post-activation time range and phase portrait of the relative motion. The gray shadings denote the instantaneous occurrence of contact at the piston/bit interface. Notation $\mathcal{U}_R$ indicates the displacement of the rock surface.

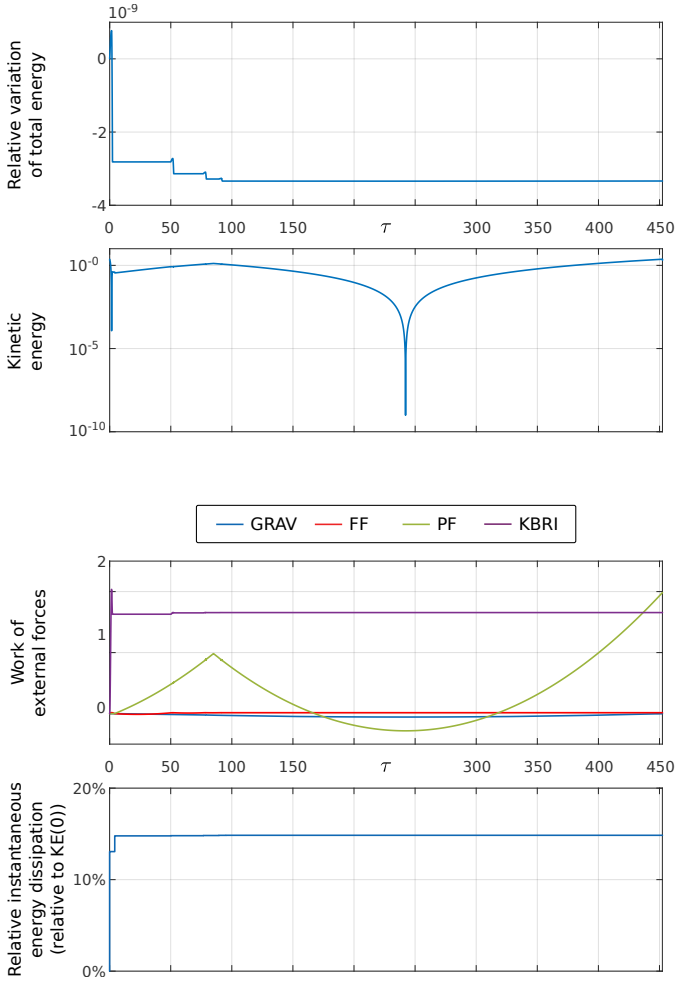

Figure 5.6: Rigid model – Energetic response of the system along the periodic trajectory. Acronyms stand for: works of gravity force (GRAV), feed force (FF), pressure force (PF), bit/rock interaction force stiffness component (KBRI).

dissipation is more important for the rigid model than for the elastic one by a factor 2.5. This additional dissipation goes in the direction of the lower predicted average rate of penetration by the rigid model, with $\langle \mathcal{V}_b \rangle_\tau = 3.95 \cdot 10^{-3}$, versus $\langle \boldsymbol{\mathcal{V}}_b \rangle_{\xi,\tau} = 4.00 \cdot 10^{-3}$ for the elastic.

5.4 Parametric analysis

To assess the influence of the model parameters around the reference configuration, we reproduce the approach used to study the drifting oscillator in Chapter 2 that we complete with additional data. The influences of the feed force φ_S, the unloading parameter γ of the bit/rock interaction, and the pressure law parameters δ_1, φ_0 are investigated. For the latter set of parameters, the constraint $\delta_1 \varphi_0^3 = \delta_1 \varphi_0^3\big|_{\mathsf{Ref}}$ is imposed. As was shown in Chapter 3, this constraint ensures the theoretical constancy of the power delivered by the pressure law.

First, we construct the stroboscopic Poincaré maps of the simulated model response as one model parameter is varied, keeping all others constant. Poincaré maps are built from simulations over $4 \cdot 10^4$ units of time, discarding the first 25% of it to remove transients. For the reference configuration, this approximately corresponds to 100 percussive activations. Snapshots are taken at the left limit of the instants corresponding to the initiation of percussive activation. The color codes of the bit/rock interaction law are used to describe its mode at the moment of the snapshot. As, in the model, bit motion is expressed in terms of displacement rather than penetration, the Poincaré map for the penetration is replaced by the average distance traveled by the bit between two percussive activations, $\langle \boldsymbol{\mathcal{U}}_b \rangle_\xi(\tau_i^-) - \langle \boldsymbol{\mathcal{U}}_b \rangle_\xi(\tau_{i-1}^-)$; this enables the removal from the bit displacement of the drift due to the penetration. For period-1 solutions, this difference indicator provides the penetration achieved over one limit cycle; this does not extend to other types of responses, though. In addition, selected bit trajectories are shown to illustrate the type of responses experienced by the system in specific conditions. The bit trajectories are taken at the end of the simulated time series. The superimposed ring markers indicate the location of the Poincaré snapshots.

Second, average indicators are computed from the simulated time series. For the investigated parametric ranges, we compare the average period of percussive activation

$\langle \omega_{34} \rangle_\tau$, the average rate of penetration for the elastic and the rigid models $\langle \boldsymbol{\mathcal{V}}_b \rangle_{\xi,\tau}, \langle \mathcal{V}_b \rangle_\tau$, and the average power delivered by the pressure force $\langle \dot{\mathsf{PF}} \rangle_\tau$.

Numerical values given in the analysis of the results are to be understood in an approximate sense. They are used to locate the reader on the plots.

5.4.1 Poincaré sections

Figures 5.7-5.8 show the influence of the feed force parameter φ_S on the simulated Poincaré maps for the elastic and rigid models, respectively. It appears that the feed force essentially counteracts the rebound of the bit that follows drilling cycles. Provided it is sufficiently large, $\varphi_S > 4$ for the elastic model and $\varphi_S > 3$ for the rigid one, the interaction law enters the standstill mode prior to the occurrence of the next percussive activation and the bit is driven to rest. In these conditions, the average motion of the bit experiences period-1 motion. For lower values, the bit experiences large amplitude free flight phases during which percussive activation occurs, most of the time; the model response seems aperiodic. As can be noted from the reference trajectories, the feed force also plays a role on the average penetration rate which seems to increase with it, as was suggested by the energetic analysis of the drilling cycle; see Section 2.5.

The influence of parameter γ on the model responses is illustrated in Figures 5.9-5.10. Both models predict that the interaction law is in standstill mode when percussive activation takes place, whatever $\gamma \in [2, 1000]$. At moderate values, both models are seen to behave similarly; starting from $\gamma = 2$, the penetration achieved per activation period increases with γ until some maximum is reached about $\gamma = 40$. Step increases are observed along the curve, these can be related to variations of the average number of drilling cycles m/n. Whereas both models show similar responses for $\gamma < 100$, the predictions differ sensibly beyond this threshold, with an increase of the penetration with γ for the elastic model and a decrease for the rigid model. These opposed trends result from a different response of the bit/rock interaction law for the elastic and the rigid model. With the rigid model, the bit experiences a free flight phase after the post-activation drilling cycle, before recontacting the rock and entering the standstill mode. With the elastic model, the post-activation drilling cycle is followed by a succession of low amplitude drilling cycles that significantly contribute to the achieved penetration before the standstill mode is reached. Whether such behavior is representative of the

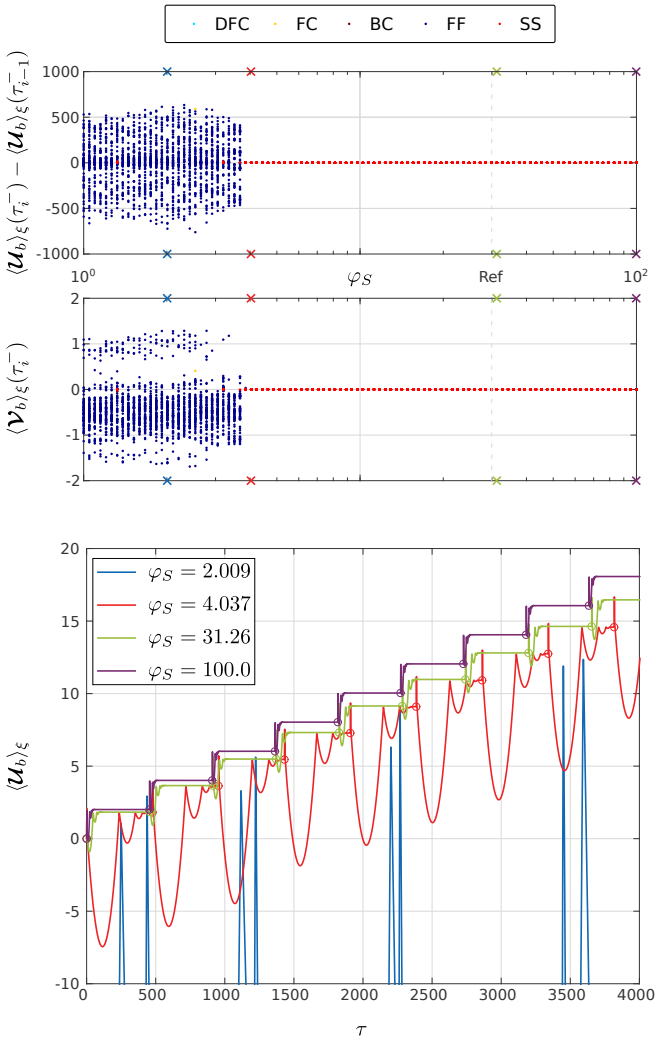

Figure 5.7: Elastic model – Influence of the feed force parameter φ_S on the stroboscopic Poincaré map and on the average bit displacement; ring markers correspond to the Poincaré snapshots. All other parameters correspond to the model reference configuration.

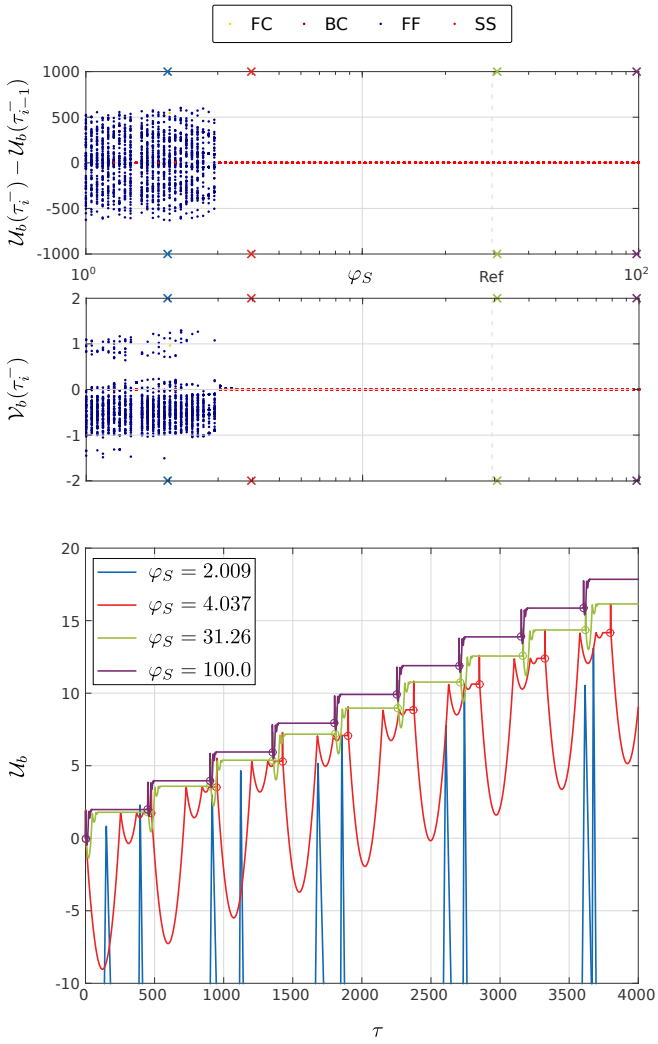

Figure 5.8: Rigid model – Influence of the feed force parameter φ_S on the stroboscopic Poincaré map and on the average bit displacement; ring markers correspond to the Poincaré snapshots. All other parameters correspond to the model reference configuration.

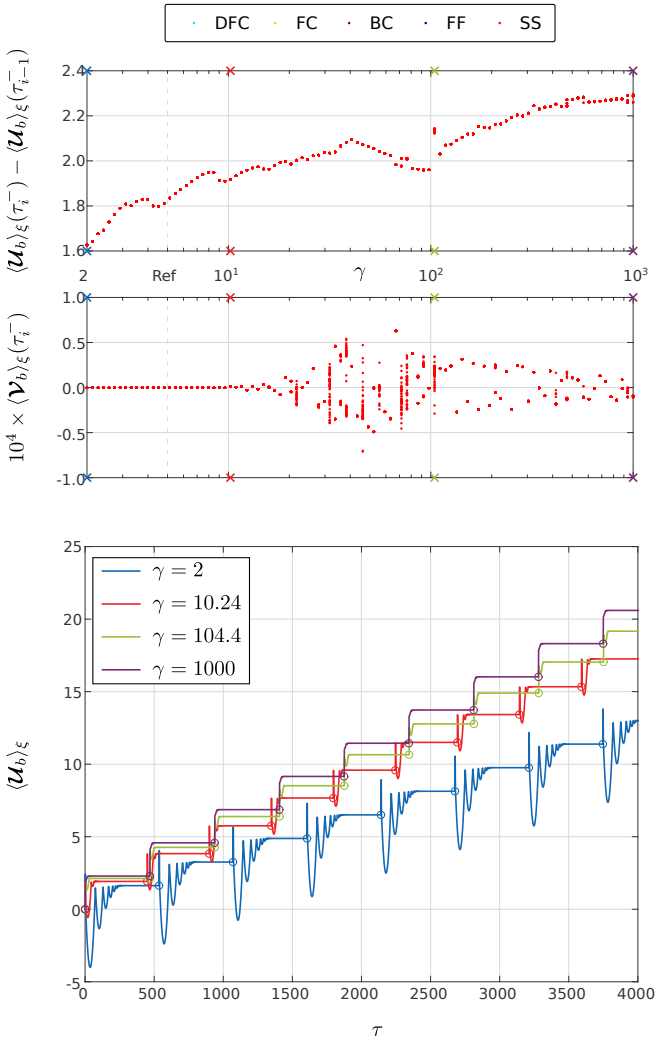

Figure 5.9: Elastic model – Influence of the bit/rock interaction parameter γ on the stroboscopic Poincaré map and on the average bit displacement; ring markers correspond to the Poincaré snapshots. All other parameters correspond to the model reference configuration.

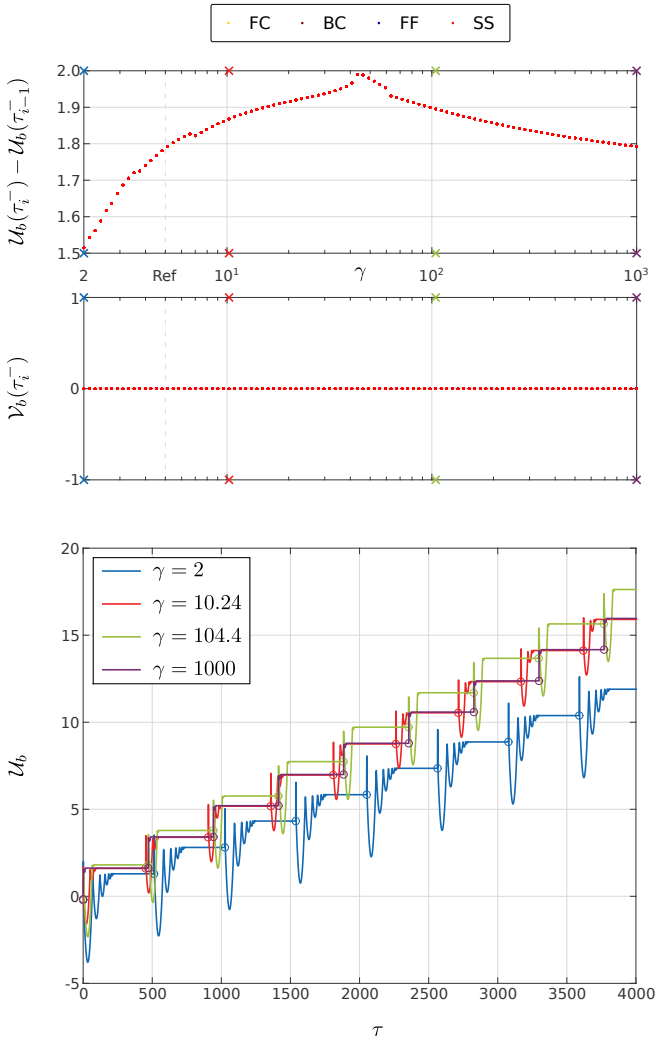

Figure 5.10: Rigid model – Influence of the bit/rock interaction parameter γ on the stroboscopic Poincaré map and on the average bit displacement; ring markers correspond to the Poincaré snapshots. All other parameters correspond to the model reference configuration.

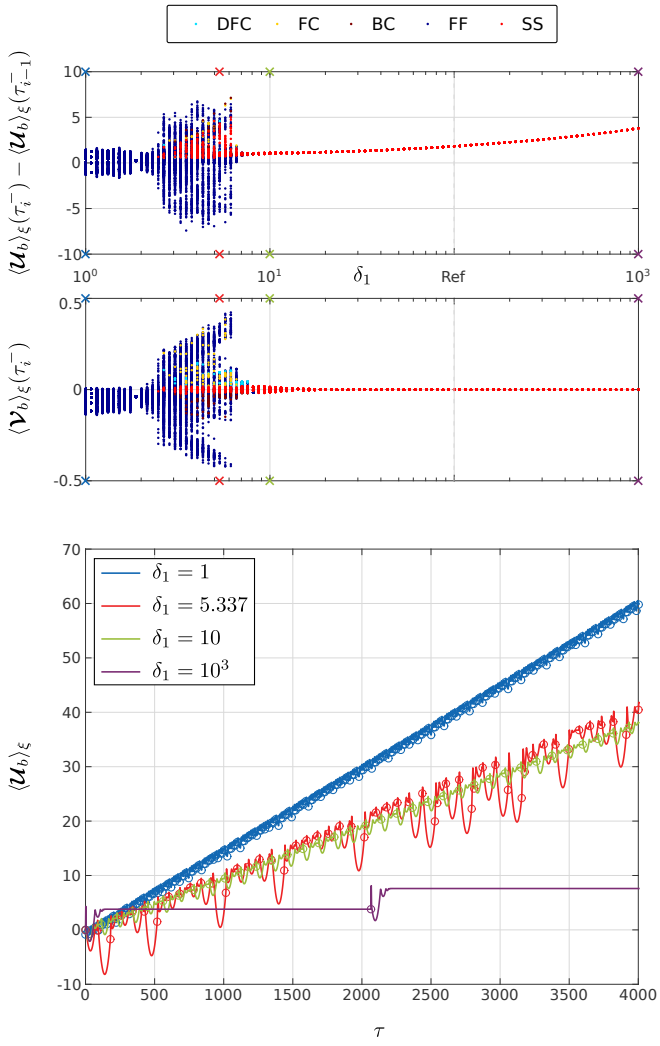

Figure 5.11: Elastic model – Influence of the pressure law parameters δ_1, φ_0 on the stroboscopic Poincaré map and on the average bit displacement; ring markers correspond to the Poincaré snapshots. The constraint $\delta_1 \varphi_0^3 = \delta_1 \varphi_0^3\big|_{\text{Ref}}$ is imposed to enforce the theoretical constancy of the power delivered by the pressure force. All other parameters correspond to the model reference configuration.

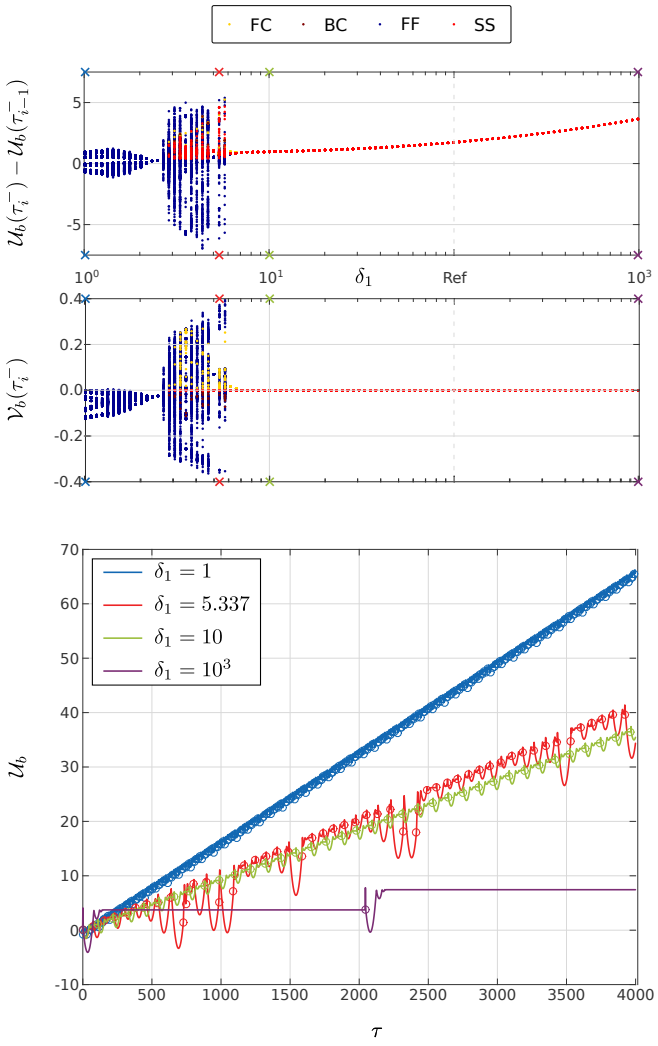

Figure 5.12: Rigid model – Influence of the pressure law parameters δ_1, φ_0 on the stroboscopic Poincaré map and on the average bit displacement; ring markers correspond to the Poincaré snapshots. The constraint $\delta_1\varphi_0^3 = \delta_1\varphi_0^3\big|_{\text{Ref}}$ is imposed to enforce the theoretical constancy of the power delivered by the pressure force. All other parameters correspond to the model reference configuration.

process physics remains unclear; its origin could well be purely numerical chatter.

For rigid models, it is now clear that the standstill mode acts as an absorbant mode for the bit dynamics. For the elastic model, the mechanical energy of the bit is not instantaneously dissipated at the entry in the standstill mode; state variables are continuous across the mode transition and the dissipation of the bit mechanical energy takes a finite time. Consequently, rich dynamical behaviors are unlikely to be observed whenever the interaction law enters the standstill mode. However, were the percussive frequency higher, the phase of independent motion of the two bodies that follows the percussive activation would be reduced and an interplay between the piston and bit dynamics could be expected, possibly, resulting in an optimal drilling configuration. Such an observation has led to the concept of *Resonance Enhanced Drilling* (RED) proposed by the University of Aberdeen to improve the penetration rate achieved by conventional rotary drilling systems [110]. It consists in the addition of a harmonic component to the feed force, whose driving frequency is a resonant one of the subsystem formed by the bit and the rock. Activation forces with frequency up to 1 kHz are delivered by a piezoelectric actuator located on top of the bit. With the present scaling, this corresponds to $\langle \omega_{34} \rangle_\tau = \mathcal{O}(10)$.

To increase the percussive frequency while keeping constant, in theory, the power delivered by the pressure force, the pressure law parameters δ_1, φ_0 are varied under the constraint $\delta_1 \varphi_0^3 = \delta_1 \varphi_0^3 \big|_{\mathsf{Ref}}$. According to the definition of the pressure force, this constraint ensures the following scaling of the percussive activation period $\langle \omega_{34} \rangle_\tau \sim \delta_1^{2/3}$. Results are given in Figures 5.11-5.12 for $\delta_1 \in [1, 10^3]$. As witnessed by the representative trajectories, the decrease of δ_1 does indeed reduce the percussive activation period that is given by the horizontal distance between two snapshots; it is also observed that the achieved penetration increases with the decrease of δ_1. The period-1 stationary solution vanishes to the benefit of seemingly aperiodic trajectories below $\delta_1 = 7$ for both models. Below these thresholds and above $\delta_1 = 2$, percussive activation takes place during any drilling mode. Below $\delta_1 < 2$, percussive activation only takes place during free flight. For both models, windows of periodic motion are observed in between the more complex patterns displayed on the Poincaré maps.

5.4.2 Average indicators

In Figures 5.13-5.15, the influence of the model parameters on the process response is observed in terms of the average period of percussive activation, $\langle \omega_{34} \rangle_\tau$, the average rate of penetration, $\langle \boldsymbol{\mathcal{V}}_b \rangle_{\xi,\tau}, \langle \mathcal{V}_b \rangle_\tau$, and the average power actually delivered by the pressure force, $\langle \dot{\mathsf{PF}} \rangle_\tau$. Predictions of the elastic and rigid models are superimposed for a better comparison.

Well-defined trends are observed when the simulated motion evolves towards a periodic attractor that structures the motion. To the contrary, when the bit experiences more complex trajectories, the average indicators are affected by the nature of the motion. A fair match is obtained between the predictions of the two models when the long-term motion is periodic. Significant discrepancies can be observed when the bit motion is erratic.

As a general trend, the increase of the feed force φ_S implies an increase of the rate of penetration $\langle \boldsymbol{\mathcal{V}}_b \rangle_{\xi,\tau}, \langle \mathcal{V}_b \rangle_\tau$ when the model predicts standstill-ending period-1 long-term motion. Two mechanisms contribute to that increase. First, post-activation drilling cycles reach a deeper penetration and, second, the period of percussive activation decreases as well. The first mechanism dominates for $\varphi_S > 10$. The trend does not apply to the zone of low feed forces, in which the bit experiences non-stationary motion.

Predictions of the alteration of the average rate of penetration by parameter γ shows important differences, even though a good correlation is observed between the predictions of the delivered pressure force power and the period of percussive activation. Given this correlation, the observed discrepancies are a reflection of those observed on the Poincaré maps for the displacement variation between two activations. Accordingly, local maxima of the penetration rate are observed at steps of the Poincaré map and at the local maximum around $\gamma = 40$. The constancy of the period of percussive activation for $\gamma > 40$ is due to the absence of a second impact at the piston/bit interface after the percussive activation; for such single impact activations, the piston rebound velocity is mainly driven by the system geometry. This is in line with the analysis of the drilling cycle, see Section 2.5, which shows that, for a rigid bit, the rebound velocity scales with $\gamma^{-1/2}$.

For the range of period-1 stationary solutions, the scaling of the percussive activation period with δ_1 proves correct, as indicated by the 2/3 slope in its log-log representation

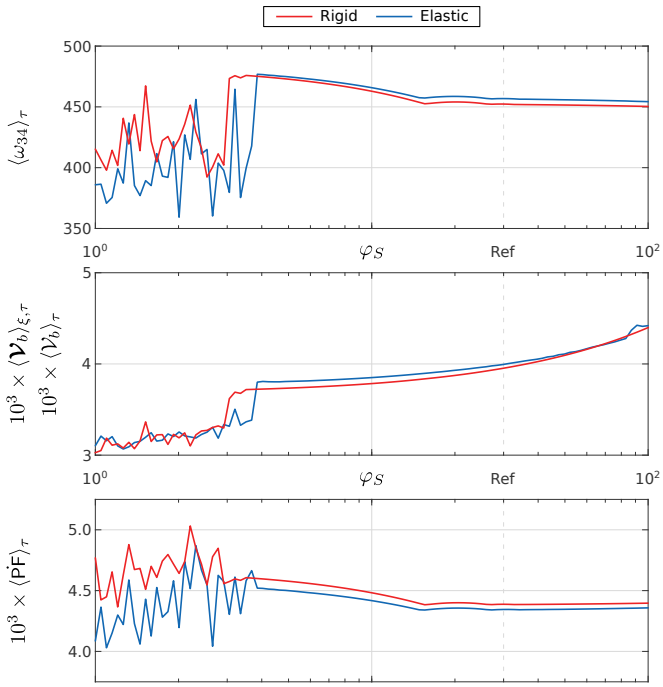

Figure 5.13: Influence of the feed force parameter φ_S on the average period of percussive activation $\langle\omega_{34}\rangle_\tau$, on the bit average rate of penetration $\langle \boldsymbol{\mathcal{V}}_b \rangle_{\xi,\tau}, \langle \mathcal{V}_b \rangle_{,\tau}$, and on the average power delivered by the pressure force $\langle \dot{\mathsf{PF}} \rangle_\tau$. All other parameters correspond to the model reference configuration.

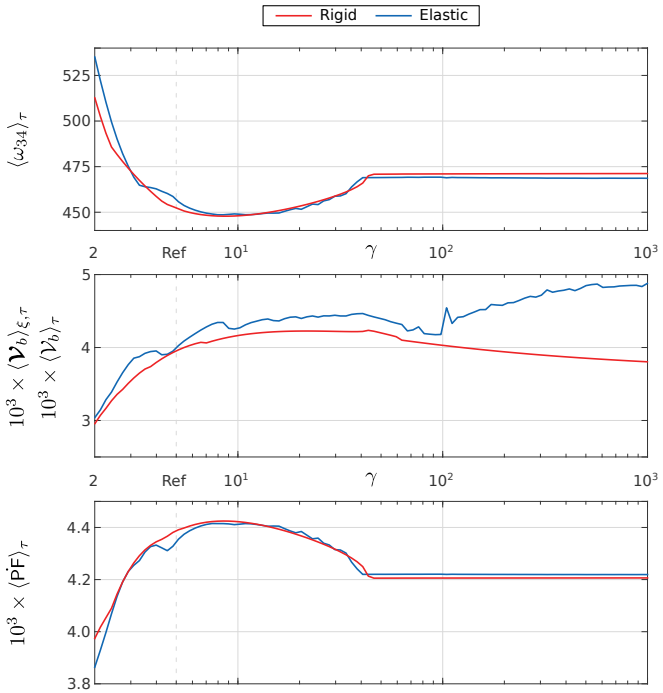

Figure 5.14: Influence of the bit/rock interaction parameter γ on the average period of percussive activation $\langle\omega_{34}\rangle_\tau$, on the bit average rate of penetration $\langle \boldsymbol{\mathcal{V}}_b \rangle_{\xi,\tau}, \langle \mathcal{V}_b \rangle_{,\tau}$, and on the average power delivered by the pressure force $\langle \dot{\mathsf{PF}} \rangle_\tau$. All other parameters correspond to the model reference configuration.

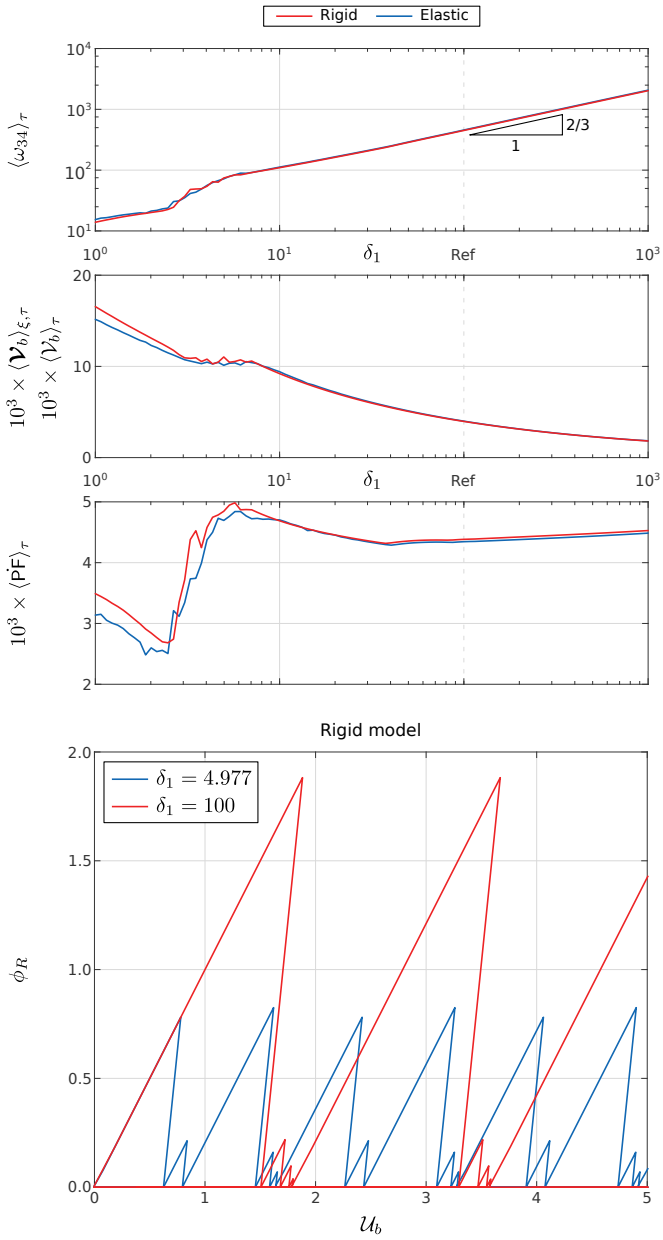

Figure 5.15: Influence of the pressure law parameters δ_1, φ_0 on the average period of percussive activation $\langle\omega_{34}\rangle_\tau$, on the bit average rate of penetration $\langle \boldsymbol{\mathcal{V}}_b \rangle_{\xi,\tau}, \langle \mathcal{V}_b \rangle_{,\tau}$, and on the average power delivered by the pressure force $\langle \dot{\mathsf{PF}} \rangle_\tau$. The constraint $\delta_1 \varphi_0^3 = \delta_1 \varphi_0^3\big|_{\mathsf{Ref}}$ is imposed. All other parameters correspond to the model reference configuration. The bottom plot shows the force/displacement response for $\delta_1 \in \{4.977; 100\}$ as predicted by the rigid model; period-2 and period-1 stationary motions are observed for these two configurations.

versus δ_1. An interesting result brought up by this investigation is the quasi-monotonic increase of the average penetration rate with the decrease of the activation period. Even though the pressure law no longer represents a pneumatic activation in the high-frequency range, this shows that, under the assumption of the bit/rock interaction law remaining valid, if one were to design an activation technology capable of delivering high loads at high frequencies, drilling performances could be dramatically increased; a factor of about 2 is achieved by reducing $\delta_1 = 100$ for the reference configuration to $\delta_1 = 10$. More surprising is the opposite evolution of the rate of penetration and of the average power delivered by the pressure force, below $\delta_1 < 6$, when the standstill-ending period-1 stationary solution vanishes. The explanation to this trend lies in the nature of the interaction law and the reduced post-activation bit velocities achieved at low δ_1. Indeed, neglecting the dissipation associated with the energy barrier and invoking the decomposition of the area enclosed by the bilinear law in n similar triangles, it is evident that the energy required to reach a given penetration scales as

$$\mathsf{KBRI}(n) = \frac{1}{n}\mathsf{KBRI}(1), \quad n > 1, \tag{5.2}$$

where $\mathsf{KBRI}(1)$ is the energy required to reach that penetration in one drilling cycle and $\mathsf{KBRI}(n)$ the energy required if the penetration is achieved through n identical drilling cycles. As the penetration achieved over a drilling cycle scales positively with the bit velocity, low post-activation bit velocities lead to a lower energy consumption by the drilling process to achieve a given penetration. In the present circumstances, this leads to a decreased power requirement from the pressure force while at the same time an increased penetration rate is achieved. These results thus indicate that high-frequency percussive drilling could not only improve rates of penetration but also reduce the energy consumption of the drilling process. The difference in the energy required to achieve a given penetration is well illustrated in the bottom plot of Figure 5.15 that shows the force/displacement response of the interaction law for $\delta_1 = 4.977$ and $\delta_1 = 100$ (reference configuration); neglecting the dissipation related to the energy barrier, the consumed energy is represented by the area enclosed between the curves and the $\mathcal{U}_b$-axis.

5.5 Concluding remarks

Assumptions of timescale separation typically require a separation by two orders of magnitude to exhibit limited errors. Such a separation is not achieved for the reference configuration, for $\omega_{41} = \sqrt{10}$ and $\omega_{42} = \sqrt{10}/1.15$. Notwithstanding the lack of separation and the different origins of energy dissipation in the two models, the conducted parametric analyses have shown that the rigid model qualitatively captures the response of the reference elastic model over most of the investigated parametric ranges for which the elastic model converges to a period-1 stationary response. Even quantitatively, the predicted average rate of penetration and period of percussive activation lie within a 10-percent error band of that predicted by the elastic model.

Two important factors favor this correlation between the model responses.

- The introduction of artificial damping in the elastic model, via the integration scheme and the stiffness-proportional viscous damping, confers a dissipative character to the originally conservative governing equations. This dissipation alters the waves propagating in the system and tends to their annihilation. As is witnessed in Figure 5.3 by the exponential decrease of the strain energy during free flight phases, the piston and the bit behave as rigid bodies at the onset of an interaction phase (impact at the piston/bit interface or transition to the DFC or the SS drilling mode) if it follows a free flight phase of a sufficient duration; sufficient must be interpreted with respect to the problem time constants and the reference level of strain energy.

- The use of a configuration-dependent reset map based on considerations of wave propagation in the mechanical system enables the proper representation of the piston/bit interaction, for the reference configuration.

Consequently, inasmuch as there are uncertainties concerning the validity of the model and the appropriate calibration of the numerical method to integrate the elastic model, we reasonably advise the use of the rigid model for the purposes of preliminary and exploratory analyses, even in situations where timescale separation is not verified *stricto sensu*. The lower complexity of the rigid model not only greatly simplifies the process analysis; it also positively impacts simulation performance as the number of

degrees of freedom is limited to two plus the history variables related to the bit/rock interaction law. Additionally, further performance improvement could be obtained by implementing a semi-analytical event-driven integration procedure as was done for the drifting oscillator; that is, a procedure that exploits analytical time parameterizations of the bit and piston trajectories.

Chapter 6

Conclusion

"In our reasonings concerning matter of fact, there are all imaginable degrees of assurance, from the highest certainty to the lowest species of moral evidence. A wise man, therefore, proportions his belief to the evidence."

D. Hume, *An Enquiry Concerning Human Understanding*

6.1 Contributions

The research works presented in this doctoral thesis constitute a first step toward the integrated modeling of down-the-hole percussive drilling, which is believed to significantly contribute to advancing the process knowledge and the understanding of the causes of the observed optimal drilling configurations in the parameter space. Following this approach, which distances itself from the existing literature, the drilling process is modeled as the resulting interaction between its underlying (sub)processes and its performance is assessed on the basis of its long-term dynamical response. In the present work, the interacting (sub)processes have been restricted to the dynamics of the mechanical system, the bit/rock interaction, and the pneumatic activation of the piston. The rotation of the system and the cleaning of the borehole are neglected by assumption.

On this basis, we have proposed three models of the process. Each of them is based on the representation by a force/penetration of the interaction between the bit and the rock, to avoid the explicit modeling of the penetration process. In the absence

of an experimental characterization of the force/penetration response for successive drilling cycles, we have arbitrarily generalized the bilinear law observed in single impact tests by introducing the notion of penetration while drilling and appending an energy barrier to its definition, to differentiate static and dynamic interactions. This results in a piecewise linear definition of the interaction law, which requires an event-driven integration strategy to solve the model governing equations.

Following the assumptions of (*i*) periodic activation, (*ii*) timescale separation between the percussive activation and the bit motion, and (*iii*) negligible bit compliance with respect to that of the bit/rock interaction, a single degree of freedom drifting oscillator excited by a periodic impulsive loading has been proposed. This first model, which is the simplest representation of the drilling process, has been studied using semi-analytical tools for a reference configuration and around it. Also, an energetic analysis of the drilling cycle has been conducted to provide analytical insights into the expected response of the oscillator; it shows the need for an energy barrier and substantiates why a typical drilling cycle is followed by a rebound of the bit. The existence of complex motion patterns has been revealed, *e.g.*, aperiodic motion or the coexistence of periodic attractors. However, around the reference configuration, no maxima of the average rate of penetration have been observed, but for variations of the bit/rock interaction parameter, which are affected by bit design but mostly driven by the nature of the rock being drilled.

To relax the assumption of independent activation dynamics, two two-body models have been proposed: one elastic and one rigid. These account for the dynamics of the piston, whose repeated impacts provide the bit with the energy required to penetrate into the rock. The pressure force driving the piston, which physically results from the fluid flow in the hammer, is approximated by a 2-parameter piecewise constant law. Estimations of the percussive activation period and the impact velocity are given so that the law can be adjusted to reproduce actual reference values. The rigid model assumes a separation between the timescales of bit motion and wave propagation; piston/bit impact interactions are modeled by a reset map giving the exact post-contact velocities of two elastic rods experiencing a collinear longitudinal impact on an elastic support. To the contrary, wave propagation is accounted for in the elastic model. Linear finite elements combined with the penalty method, to handle contact interactions, are used

to transform the governing partial differential equations into second-order equations of motion. Viscous damping proportional to the stiffness matrix is added to control the Gibbs oscillations arising from the piston/bit impacts, as we show that it plays a role equivalent to that of the numerical damping associated with state-of-the-art upwind-based finite difference schemes.

To numerically solve the equations governing the dynamics of these models has required the development of adapted tools. Notably, we have derived a two-level high-order unconditionally stable integration scheme dedicated to the integration of the equations of linear structural dynamics; we have dubbed it the DE^3 scheme by reference to the root common to the author's name and his advisers'. Parallel to this development, we have proposed a framework for the accuracy analysis of dynamics-oriented two-level schemes; it accounts for both linear viscous damping and external forcing in the evaluation of the scheme order of accuracy. Additionally, a root-solving module for coupling with time integration schemes has been developed. By enforcing event occurrence at the localization stage, the module facilitates mode switching and prevents issues such as numerical grazing and discontinuity sticking.

Using the developed numerical tools, a comparative analysis of the dynamical responses of the two-body models was conducted, again, at a reference configuration and around it; the reference configuration is representative of a 3-in hammer (low size). The average period of percussive activation, the average rate of penetration, and the average power delivered by the pressure force were monitored. Interestingly, for periodic long-term responses, the predictions of the elastic and rigid two-body models are in good agreement; discrepancies are, nevertheless, observed when the bit experiences complex motion. Simulations do not reveal the existence of optimal drilling configurations but with respect to the interface unloading parameter; the experimental observations of Amjad [5] are not reproduced by the proposed models, at least in the explored parametric range. Both the static force applied to the bit or the frequency of the percussive activation have, on average, a monotonic influence on the rate of penetration. Increasing them, in particular the percussive activation frequency, does contribute to increasing the penetration rate. Surprisingly, the increase of the penetration rate is accompanied by a decrease of the power delivered by the pressure force once the period of the percussive activation compares with the timescale associated with the bit/rock interaction;

this could be interpreted as a form of resonance. Assuming the model predictions valid, the analysis indicates that significant improvements of the penetration rate are likely to come from an increase of the frequency of percussive activation.

One of the difficulties inherent to the definition of the drifting oscillator parameters is the evaluation of the effective impulse delivered to the bit at each percussive activation. For percussive activations comprising a single impact, a partial answer is given by the scaling of the pressure law. For percussive activations comprising two impacts, a situation observed at the reference configuration, the identification of such a parameter seems illusive without a calibration procedure.

6.2 Directions for future works

An invalid model is worth nothing. The arbitrary choices that we have made in the model formulation may cast doubts on their predictions. Works shedding light on these question marks should come next. The presented models and results should definitely be used to guide the design of appropriate validation experiments.

Although based on the evident approach of integrated dynamics, the models proposed in this thesis nonetheless rest upon an arbitrary and, therefore, questionable generalization to successive drilling cycles of the bit/rock interaction law. As the model predictions entirely depend on its definition, its validation, be it numerical or experimental, is of utter importance. In particular, the identification of an adequate level for the energy barrier should be investigated; as it controls the end of the penetration mechanism, it plays an essential influence on the predicted rate of penetration.

Also, as the model predictions have not revealed the existence of optimal drilling configurations, we may wonder whether the sole justification of the process dynamics is behind them or if account of an enriched bit/rock interaction should be taken. It could, for instance, account for the maximal penetration set by the bit button size or the influence of the drilling parameters on the hole cleaning. Investigations in this direction should definitely be carried out.

The dynamic finite element approach that has been used to solve the elastic model is known to generate spurious oscillations in the presence of high gradients or discontinuities of the discretized field. The introduction of artificial damping enables the reduction

of these numerical foes but does not eliminate them. It also attenuates the waves propagating in the mechanical parts whose motion is eventually reduced to that of their center of gravity. The numerical resolution of the elastic model with alternative numerical methods, *e.g.*, the wave finite element method [111] or methods based on adaptive meshing [112, 113], is definitely of interest if they can alleviate the general numerical trouble.

Notwithstanding these reserves, exploring further the parameter range of the proposed model is a task of importance. If possible, it should be conducted under the guidance of an industrial partner that would provide the appropriate parameter combinations and the critical eye of field engineers. For these investigations, the dimensional model might be of easier use, in particular for the assessment of the interaction stiffness influence.

The rigid two-body model exploits wave propagation results to define the post-activation velocities. This definition leads to an instantaneous loss of mechanical energy when the bit is elastically supported. Investigations as to the influence of this dissipation on the predicted results should be conducted and the scope of validity of this reset map refined.

Bibliography

[1] A. Stenuick. Apparatus for dry drilling of bore holes, February 11 1958. US Patent 2,823,013.

[2] W.A. Hustrulid and C.E. Fairhurst. Theoretical and Experimental Study of Percussive Drilling of Rock. Part I: Theory of Percussive Drilling. *International Journal of Rock Mechanics and Mining Sciences & Geomechanics Abstracts*, 8(4):311–333, July 1971.

[3] S. Beasley. A legacy from Belgium lives on. *GeoDrilling International*, pages 32–33, January/February 2006.

[4] G. Han, M. Bruno, and K. Lao. Percussion Drilling in Oil Industry: Review and Rock Failure Modeling. In *AADE 2005 National Technical Conference and Exhibition*, number AADE-05-NTCE-59, pages 1–10, Houston, Texas, U.S.A., April 2005.

[5] M. Amjad. *Control of ITH Percussive Longhole Driling in Hard Rock*. Ph.D. thesis, McGill University, Montreal, Quebec, Canada, 1996.

[6] M. Bruno. Fundamental research on percussion drilling: Improved rock mechanics analysis, advanced simulation technology, and full-scale laboratory investigations. Technical Report DE-FC26-03NT41999, Terralog Technologies Inc, February 2005.

[7] W.A. Hustrulid and C.E. Fairhurst. Theoretical and Experimental Study of Percussive Drilling of Rock. Part II: Force-Penetration and Specific Energy Determinations. *International Journal of Rock Mechanics and Mining Sciences & Geomechanics Abstracts*, 8(4):335–356, July 1971.

[8] B.R. Stephenson. *Measurement of Dynamic Force-Penetration Characteristics in Indiana Limestone*. Master's thesis, University of Minnesota, 1963.

[9] B. Haimson. *High Velocity, Low Velocity and Static Penetration Characteristics in Tennessee Marble*. Master's thesis, University of Minnesota, 1965.

[10] L.G. Karlsson, B. Lundberg, and K.G. Sundin. Experimental study of a percussive process for rock fragmentation. *International Journal of Rock Mechanics and Mining Sciences & Geomechanics Abstracts*, 26(1):45–50, January 1989.

[11] W.A. Hustrulid and C.E. Fairhurst. A theoretical and experimental study of the percussive drilling of rock. Part III: Experimental verification of the mathematical theory. *International Journal of Rock Mechanics and Mining Sciences & Geomechanics Abstracts*, 9(3):417–418, May 1972.

[12] T. Saksala, D. Gomon, M. Hokka, and V.-T. Kuokkala. Numerical and experimental study of percussive drilling with a triple-button bit on Kuru granite. *International Journal of Impact Engineering*, 72:56–66, October 2014.

[13] H. Liu, S. Kou, and P. Lindqvist. Numerical studies on bit-rock fragmentation mechanisms. *International Journal of Geomechanics*, 8(1):45–67, January 2008.

[14] S. Y. Wang, S. W. Sloan, H. Y. Liu, and C. A. Tang. Numerical simulation of the rock fragmentation process induced by two drill bits subjected to static and dynamic (impact) loading. *Rock Mechanichs and Rock Engineering*, 44(3):317–332, November 2011.

[15] T. Saksala. Numerical modelling of bit-rock fracture mechanisms in percussive drilling with a continuum approach. *International Journal for Numerical and Analytical Methods in Geomechanics*, 35(13):1483–1505, September 2011.

[16] T. Saksala. 3D numerical modelling of bit-rock fracture mechanisms in percussive drilling with a multiple-button bit. *International Journal for Numerical and Analytical Methods in Geomechanics*, 37(3):309–324, February 2013.

[17] B. Lundberg. Energy transfer in percussive rock destruction – I: Comparison of percussive methods. *International Journal of Rock Mechanics and Mining Sciences*, 10(5):381–399, September 1973.

[18] B. Lundberg. Energy-Transfer in Percussive Rock Destruction – II: Supplement on Hammer Drilling. *International Journal of Rock Mechanics and Mining Sciences*, 10(5):401–419, September 1973.

[19] R. Simon. Transfer of the stress wave energy in the drill steel of a percussive drill to the rock. *International Journal of Rock Mechanics and Mining Sciences & Geomechanics Abstracts*, 1(3):397–411, May 1964.

[20] B. Lundberg. Microcomputer simulation of percussive drilling. *International Journal of Rock Mechanics and Mining Sciences*, 22(4):237–249, August 1985.

[21] B. Lundberg. Computer modelling and simulation of percussive drilling of rock. In J.A. Hudson, editor, *Comprehensive rock engineering*. Pergamon, 1993.

[22] L.E. Chiang and D.A. Elias. Modeling impact in down-the-hole rock drilling. *International Journal of Rock Mechanics and Mining Sciences*, 37(4):599–613, June 2000.

[23] B. Lundberg and M. Okrouhlik. Influence of 3D effects on the efficiency of percussive rock drilling. *International Journal of Impact Engineering*, 25(4):345–360, April 2001.

[24] B. Lundberg and M. Okrouhlik. Efficiency of a percussive rock drilling process with consideration of wave energy radiation into the rock. *International Journal of Impact Engineering*, 32(10):1573–1583, October 2006.

[25] L.E. Chiang and D.A. Elías. A 3D FEM methodology for simulating the impact in rock-drilling hammers. *International Journal of Rock Mechanics and Mining Sciences*, 45(5):701–711, July 2008.

[26] E. Pavlovskaia and M. Wiercigroch. Periodic solution finder for an impact oscillator with a drift. *Journal of Sound and Vibration*, 267(4):893–911, October 2003.

[27] A.M. Krivtsov and M. Wiercigroch. Dry friction model of percussive drilling. *Meccanica*, 34(6):425–435, December 1999.

[28] E. Pavlovskaia, M. Wiercigroch, and C. Grebogi. Modeling of an impact system with a drift. *Physical Review E*, 64:56224–56229, November 2001.

[29] O.K. Ajibose, M. Wiercigroch, E. Pavlovskaia, and A.K. Akisnaya. Global and local dynamics of drifting oscillator for different contact force models. *International Jounal of Non-Linear Mechanics*, 45(9):850–858, November 2010.

[30] E. Pavlovskaia, D.C. Hendry, and M. Wiercigroch. Modelling of high frequency vibro-impact drilling. *International Journal of Mechanical Sciences*, 2013. In press.

[31] O.K. Ajibose, M. Wiercigroch, E. Pavlovskaia, A.R. Akisanya, and G. Karolyi. Drifting Impact Oscillator With a New Model of the Progression Phase. *Journal of Applied Mechanics - Transactions of the ASME*, 79(6), November 2012.

[32] A. Depouhon, V. Denoël, and E. Detournay. A drifting impact oscillator with periodic impulsive loading: Application to percussive drilling. *Physica D: Nonlinear Phenomena*, 258(0):1–10, September 2013.

[33] L.E. Chiang and E.B. Stamm. Design optimization of valveless DTH pneumatic hammers by a weighted pseudo-gradient search method. *Journal of Mechanical Design*, 120(4):687–694, December 1998.

[34] A. Depouhon, V. Denoël and E. Detournay. Numerical simulation of percussive drilling. *International Journal for Numerical and Analytical Methods in Geomechanics*. Accepted.

[35] A. Depouhon, V. Denoël and E. Detournay. A dynamical model for down-the-hole percussive drilling. *International Journal of Rock Mechanics and Mining Sciences*. In preparation.

[36] A. Depouhon, E. Detournay, and V. Denoël. Limit cycling behavior of a hybrid system: Application to percussive drilling. In *Proceedings of the 2nd International Colloquium on Non-Linear Dynamics and Control of Deep Drilling Systems*, Eindhoven, May 2012.

[37] A. Depouhon, E. Detournay, and V. Denoël. Accuracy of one-step integration schemes for damped/forced linear structural dynamics. *International Journal for Numerical Methods in Engineering*, 2014. In press.

[38] A. Depouhon, E. Detournay, and V. Denoël. Event-driven integration of linear structural dynamics models under unilateral elastic constraints. *Computer Methods in Applied Mechanics and Engineering*, 276(0):312–340, July 2014.

[39] R.I. Leine and H. Nijmeijer. *Dynamics and Bifurcations of Non-Smooth Mechanical Systems*. Springer-Verlag Berlin Heidelberg, 2004.

[40] R. Goebel, R.G. Sanfelice, and A.R. Teel. Hybrid dynamical systems. *Control Systems, IEEE*, 29(2):28–93, April 2009.

[41] V. Acary and B. Brogliato. *Numerical Methods for Nonsmooth Dynamical Systems. Applications in Mechanics and Electronics.* Springer-Verlag Berlin Heidelberg, 2008.

[42] A.H. Nayfeh and B. Balachandran. *Applied Nonlinear Dynamics: Analytical, Computational and Experimental Methods*. Wiley-VCH Verlag GmbH and Co. KGaA, Weinheim, 1995.

[43] R. Seydel. *Practical bifurcation and stability analysis*. Springer Science+Business Media, LLC, New York, USA, 2010.

[44] A.M.P. Valli, R.N. Elias, G.F. Carey, and A.L.G.A. Coutinho. PID adaptive control of incremental and arclength continuation in nonlinear applications. *International Journal for Numerical Methods in Fluids*, 61(10):1181–1200, January 2009.

[45] J. Awrejcewicz and C.-H. Lamarque. *Bifurcation And Chaos In Nonsmooth Mechanical Systems*. World Scientific Publishing Co., 2003.

[46] M. di Bernardo, C.J. Budd, A.R. Champneys, and P. Kowalczyk. *Piecewise-smooth Dynamical Systems – Theory and Applications*, volume 163. Springer-Verlag London Ltd., 2008.

[47] F. Peterka and J. Vacik. Transition to chaotic motion in mechanical systems with impacts. *Journal of Sound and Vibration*, 154(1):95–115, April 1992.

[48] F. Peterka. Dynamics of Double Impact Oscillators. *Facta Universitatis. Series Mechanics, Automatic Control and Robotics*, 2(10):1177–1190, May 2000.

[49] R.I. Leine and N. van de Wouw. *Stability and convergence of mechanical systems with unilateral constraints*. Lecture notes in applied and computational mechanics. Springer-Verlag Berlin Heidelberg, 2008.

[50] J.A. Aros. Pressurized fluid flow system for a normal circulation hammer and hammer thereof, September 1, 2011. US 2011/0209919 A1.

[51] `http://www.slb.com/services/drilling/tools_services/drill_bits.aspx`.

[52] L.E. Izquierdo and L.E. Chiang. A methodology for estimation of the specific rock energy index using corrected down-the-hole drill monitoring data. *Mining Technology*, 113(4):225–236, 2004.

[53] K.F. Graff. *Wave Motion in Elastic Solids*. Dover Books on Engineering Series. Dover Publications, 1975.

[54] M. Géradin and D. Rixen. *Mechanical Vibrations: Theory and Application to Structural Dynamics*. Wiley, 1997.

[55] D. Doyen, A. Ern, and S. Piperno. Time-integration schemes for the finite element dynamic Signorini problem. *SIAM Journal on Scientific Computing*, 33(1):223–249, 2011.

[56] G.I. Barenblatt. *Scaling*. Cambridge Texts in Applied Mathematics. Cambridge University Press, 2003.

[57] J.P. Boyd. *Chebyshev and Fourier spectral methods*. Dover Publications, Inc., New York, 2000.

[58] D. Gottlieb and J.S. Hesthaven. Spectral methods for hyperbolic problems. *Journal of Computational and Applied Mathematics*, 128(1-2):83–131, March 2001. Numerical Analysis 2000. Vol. VII: Partial Differential Equations.

[59] C. Canuto, Y. Hussaini, A. Quarteroni, and T.A. Zang. *Spectral Methods: Fundamentals in Single Domains*. Scientific Computation. Springer-Verlag Berlin Heidelberg, 2006.

[60] A. Quarteroni, R. Sacco, and F. Saleri. *Numerical Mathematics*. Texts in Applied Mathematics. Springer-Verlag New York, Inc., 2010.

[61] D.R. Lynch. *Numerical Partial Differential Equations for Environmental Scientists and Engineers: A First Practical Course*. Springer Science+Business Media, Inc., New York, 2005.

[62] B. Cockburn. Discontinuous Galerkin methods. *ZAMM - Journal of Applied Mathematics and Mechanics / Zeitschrift für Angewandte Mathematik und Mechanik*, 83(11):731–754, 2003.

[63] E. Burman, A. Quarteroni, and B. Stamm. Interior penalty continuous and discontinuous finite element approximations of hyperbolic equations. *Journal of Scientific Computing*, 43(3):293–312, 2010.

[64] J.E. Flaherty, L. Krivodonova, J.-F. Remacle, and M.S. Shephard. Aspects of discontinuous Galerkin methods for hyperbolic conservation laws. *Finite Elements in Analysis and Design*, 38(10):889 – 908, August 2002. 2001 Robert J. Melosh Medal Competition.

[65] T.J.R. Hughes. *The finite element method: linear static and dynamic finite element analysis*. Dover, 1987.

[66] T. Belytschko, W.K. Liu, and B. Moran. *Nonlinear finite elements for continua and structures*. J. Wiley & Sons, Ltd, Chichester, New York, Weinheim, 2000.

[67] S. Krenk. State-space time integration with energy control and fourth-order accuracy for linear dynamic systems. *International Journal for Numerical Methods in Engineering*, 65:595–619, January 2006.

[68] T. Belytschko and M.O. Neal. Contact-impact by the pinball algorithm with penalty and lagrangian methods. *International Journal for Numerical Methods in Engineering*, 31(3):547–572, March 1991.

[69] P. Wriggers. *Computational contact mechanics*. John Wiley and Sons, Ltd, 2006.

[70] H.M. Hilber and T.J.R. Hughes. Collocation, dissipation and overshoot for time integration schemes in structural dynamics. *Earthquake Engineering & Structural Dynamics*, 6(1):99–117, 1978.

[71] C.L. Bottasso and L. Trainelli. An Attempt at the Classification of Energy Decaying Schemes for Structural and Multibody Dynamics. *Multibody System Dynamics*, 12:173–185, 2004.

[72] G.M. Hulbert. Time finite element methods for structural dynamics. *International Journal for Numerical Methods in Engineering*, 33(2):307–331, 1992.

[73] X.D. Li and N.-E. Wiberg. Structural Dynamic Analysis by a Time-Discontinuous Galerkin Finite Element Method. *International Journal for Numerical Methods in Engineering*, 39(12):2131–2152, 1996.

[74] G. M. Hulbert. *Computational Structural Dynamics*, chapter 5. John Wiley & Sons, Ltd, 2004.

[75] T.J.R. Hughes and T. Belytschko. A Précis of Developments in Computational Methods for Transient Analysis. *Journal of Applied Mechanics-transactions of The Asme*, 50:1033–1041, 1983.

[76] A. Muğan and G.M. Hulbert. Frequency-domain analysis of time-integration methods for semidiscrete finite element equations. Part II: Hyperbolic and parabolic-hyperbolic problems. *International Journal for Numerical Methods in Engineering*, 51(3):351–376, 2001.

[77] F. Armero and I. Romero. On the formulation of high-frequency dissipative time-stepping algorithms for nonlinear dynamics. Part II: second-order methods. *Computer Methods in Applied Mechanics and Engineering*, 190(51):6783–6824, 2001.

[78] C.L. Bottasso, M. Borri, and L. Trainelli. Integration of elastic multibody systems by invariant conserving/dissipating algorithms. II. Numerical schemes and applications. *Computer Methods in Applied Mechanics and Engineering*, 190:3701–3733, 2001.

[79] J.C. Simo and N. Tarnow. The discrete energy-momentum method. Conserving algorithms for nonlinear elastodynamics. *Zeitschrift für angewandte Mathematik und Physik ZAMP*, 43(5):757–792, 1992.

[80] S. Krenk. Energy conservation in newmark based time integration algorithms. *Computer Methods in Applied Mechanics and Engineering*, 195(44-47):6110–6124, 2006.

[81] W.L. Wood. Numerical integration of structural dynamics equations including natural damping and periodic forcing terms. *International Journal for Numerical Methods in Engineering*, 17(2):281–289, February 1981.

[82] W.L. Wood. On the effect of natural damping on the stability of a time-stepping scheme. *Communications in Applied Numerical Methods*, 3(2):141–144, March/April 1987.

[83] I. Romero. On the stability and convergence of fully discrete solutions in linear elastodynamics. *Computer Methods in Applied Mechanics and Engineering*, 191(35):3857–3882, 2002.

[84] L.F. Shampine and M.W. Reichelt. The MATLAB ODE Suite. *SIAM Journal on Scientific Computing*, 18, 1997.

[85] M.B. Carver. Efficient integration over discontinuities in ordinary differential equation simulations. *Mathematics and Computers in Simulation*, 20:190–196, 1978.

[86] D. Ellison. Efficient automatic integration of ordinary differential equations with discontinuities. *Mathematics and Computers in Simulation*, 23:12–20, 1981.

[87] J.M. Esposito and V. Kumar. A state event detection algorithm for numerically simulating hybrid systems with model singularities. *ACM Transactions on Modeling and Computer Simulation*, 17(1), 2007.

[88] L.F. Shampine, I. Gladwell, and R.W. Brankin. Reliable Solution of Special Event Location-Problems for ODEs. *ACM Transactions on Mathematical Software*, 17(1):11–25, MAR 1991.

[89] T. Park and P.I. Barton. State Event Location in Differential-Algebraic Models. *ACM Transactions on Modeling and Computer Simulation*, 6(2):137–165, 1996.

[90] J.C.F. Sturm. Mémoire sur la résolution des équations numériques. *Bulletin des Sciences de Férussac*, 11:419–425, 1829.

[91] F. Boulier. Systèmes polynomiaux : que signifie "résoudre"? Online lecture notes – Consulted on 14-oct-13, 2010.

[92] M. Suzuki and T. Sasaki. On sturm sequence with floating-point number coefficients. *RIMS Kokyuroku*, 685:1–14, 1989.

[93] J. Kopp. Efficient numerical diagonalization of hermitian 3x3 matrices. *International Journal of Modern Physics C*, 19:523–548, 2008.

[94] R.M. Corless, A. Shakoori, D.A. Aruliah, and L. Gonzalez-Vega. Barycentric Hermite Interpolants for Event Location in Initial-Value Problems. *Journal of Numerical Analysis, Industrial and Applied Mathematics*, 1:1–14, 2007.

[95] Peter Strobach. Solving cubics by polynomial fitting. *Journal of Computational and Applied Mathematics*, 235(9):3033–3052, 2011.

[96] L.G. Birta, T.I. Oren, and D.L. Kettenis. A robust procedure for discontinuity handling in continuous system simulation. *Transactions of The Society for Computer Simulation International*, 2(3):189–205, September 1985.

[97] V. Bahl and A.A. Linninger. Modeling of continuous-discrete processes. In M.D. Benedetto and A. Sangiovanni-Vincentelli, editors, *Hybrid Systems: Computation and Control*, volume 2034 of *Lecture Notes in Computer Science*, pages 387–402. Springer-Verlag Berlin Heidelberg, 2001.

[98] M. Payr. *An Experimental and Theoretical Study of Perfect Multiple Contact Collisions in Bodies*. PhD thesis, ETH Zürich, 2008.

[99] F. Armero and E. Petőcz. Formulation and analysis of conserving algorithms for frictionless dynamic contact/impact problems. *Computer Methods in Applied Mechanics and Engineering*, 158(3-4):269–300, 1998.

[100] L. Noels. *Contributions aux algorithmes d'intégration temporelle conservant l'énergie en dynamique non-linéaire des structures*. Ph.D. thesis, Université de Liège, 2004.

[101] G.M. Hulbert. Discontinuity-capturing operators for elastodynamics. *Computer Methods in Applied Mechanics and Engineering*, 96(3):409–426, 1992.

[102] E. Gomes Dutra Do Carmo, C. Da Silva Garcia Monteiro, and W. João Mansur. A finite element method based on capturing operator applied to wave propagation modeling. *Computer Methods in Applied Mechanics and Engineering*, 201-204(0):127–138, January 2012.

[103] C.-W. Shu and S. Osher. Efficient implementation of essentially non-oscillatory shock-capturing schemes. *Journal of Computational Physics*, 77(2):439–471, August 1988.

[104] G.-S. Jiang and C.-W. Shu. Efficient implementation of weighted ENO schemes. *Journal of Computational Physics*, 126(1):202–228, June 1996.

[105] J.W. Banks and W.D. Henshaw. Upwind schemes for the wave equation in second-order form. *Journal of Computational Physics*, 231(17):5854–5889, July 2012.

[106] J.C. Strikwerda. *Finite Difference Schemes and Partial Differential Equations*. Society for Industrial and Applied Mathematics, Philadelphia, PA, USA, 2004.

[107] R. LeVeque. *Finite Difference Methods for Ordinary and Partial Differential Equations: Steady-State and Time-Dependent Problems*. Society for Industrial and Applied Mathematics, Philadelphia, PA, USA, 2007.

[108] R.F. Warming and B.J. Hyett. The modified equation approach to the stability and accuracy analysis of finite-difference methods. *Journal of Computational Physics*, 14(2):159 – 179, February 1974.

[109] Personal communications with J. Aros, R&D Manager, DrillCo Tools S.A.

[110] M. Wiercigroch. Resonance enhanced drilling: method and apparatus, August 11 2010. European Patent 2 041 389 B1.

[111] B.F. Schorr. *The wave finite element method*. Springer-Verlag Berlin Heidelberg, 2004.

[112] S. Thite. Adaptive spacetime meshing for discontinuous Galerkin methods. *Computational Geometry*, 42(1):20–44, January 2009.

[113] W. Bangerth, M. Gelger, and R. Rannacher. Adaptive Galerkin Finite Element Methods for the Wave Equation. *Computer Methods in Applied Mathematics*, 10(1):3–48, January 2010.

[114] S.J. Farlow. *An Introduction to Differential Equations and Their Applications*. Dover Books on Mathematics. Dover Publications, 2012.

[115] K. Lust. *Numerical bifurcation analysis of periodic solutions of partial differential equations*. Ph.D. thesis, Katholieke Universiteit Leuven, 1997.

[116] W.L. Brogan. Modern control theory, 3$^{\text{rd}}$ edition, 1991.

[117] E.J. Doedel. AUTO: A program for the automatic bifurcation analysis of autonomous systems. *Congressis Numerantium*, 30:265–284, April 1981.

[118] W.J.F. Govaerts. *Numerical Methods for Bifurcations of Dynamical Equilibria*. Society for Industrial and Applied Mathematics, 2000.

[119] H.B. Keller. Numerical solution of bifurcation and nonlinear eigenvalue problems. *Applications of bifurcation theory*, pages 359–384, 1977.

[120] E. Riks. An incremental approach to the solution of snapping and buckling problems. *International Journal of Solids and Structures*, 15(7):529–551, 1979.

[121] *ABAQUS Documentation*. Dassault Systèmes, Providence, RI, USA, 2011.

[122] S.H. Strogatz. *Nonlinear dynamics and chaos (with applications to physics, biology, chemistry)*. Perseus Publishing, 2006.

[123] O.A. Bauchau, C.L. Bottasso, and L. Trainelli. Robust integration schemes for flexible multibody systems. *Computer Methods in Applied Mechanics and Engineering*, 192:395–420, 2003.

[124] G.M. Hulbert and I. Jang. Automatic time step control algorithms for structural dynamics. *Computer Methods in Applied Mechanics and Engineering*, 126(1-2):155–178, September 1995.

Appendix A

Drifting oscillator: numerical aspects

Through its hybrid definition, the drifting oscillator model requires specific tools for its analysis. Among them, we find a semi-analytical event-driven integration procedure that serves as the basis to further analysis tools to compute periodic solutions in the space of model parameters and assess their stability.

This appendix aims at providing the key steps behind the development of these tools. References are provided whenever possible, so that the text can remain as high-level as possible, the purpose of this thesis not being the development of numerical methods for the analysis of hybrid systems.

A.1 Semi-analytical event-driven integration

The concept of event-driven integration has been reviewed in Chapter 2. In essence, it is described by: integrate the governing equations of the model from given initial conditions until something happens (occurrence of an event), do the appropriate model update (state and vector field) and restart the procedure. Two ingredients are necessary: (i) an integration procedure to compute the system trajectory and (ii) an event-detection module. In the case of the drifting oscillator model, the integration can be performed analytically as well as the event-detection, on the basis of the analytical parametrization of the bit trajectory. These elements are developed below. Their use not only ensures

the robustness of the scheme but also its computational efficiency. The decrease of the computational burden ranges between one to two orders of magnitude as compared to a fully numerical procedure (integration and event-detection).

Between percussive activations, the equation of motion of the drifting oscillator has the generic form

$$\ddot{\mathcal{P}} + \beta_R \mathcal{P} = \phi_R. \tag{A.1}$$

Parameters β_R, ϕ_R vary with the drilling mode as follows

$$\beta_R = \begin{cases} 0 & \mathsf{FF}, \\ 1 & \mathsf{FC}, \\ \gamma & \mathsf{BC}, \end{cases} \qquad \phi_R = \phi_S + \begin{cases} 0 & \mathsf{FF}, \\ 0 & \mathsf{FC}, \\ \gamma \mathcal{P}_u & \mathsf{BC}. \end{cases} \tag{A.2}$$

The trivial dynamics following the occurrence of the SS mode does not require any attention, as it suffices to enforce rest conditions on the penetration and velocity variables. The range of consistent initial conditions is also dependent on the drilling mode. It is given by

$$\begin{aligned} \mathsf{FF}: &\quad \mathcal{P}_0 \in (-\infty, \mathcal{P}_u], \quad \dot{\mathcal{P}}_0 \in \mathbb{R}, \\ \mathsf{FC}: &\quad \mathcal{P}_0 \in [0, +\infty), \quad \dot{\mathcal{P}}_0 \in \mathbb{R}^+ \backslash \{0\}, \\ \mathsf{BC}: &\quad \mathcal{P}_0 \in (\mathcal{P}_u, \mathcal{P}_p], \quad \dot{\mathcal{P}}_0 \in \mathbb{R}^-. \end{aligned} \tag{A.3}$$

History variables $\mathcal{P}_u > 0$ or $\mathcal{P}_p > 0$ must also be provided to initialize the event functions defining the conditions of mode transition, if the initial mode is FF or FC, respectively.

In the case of FF motion, the time parametrization of the bit trajectory is merely obtained by double integration of the equation of motion, yielding

$$\begin{aligned} \mathcal{P}(\tau) &= \mathcal{P}_0 + \dot{\mathcal{P}}_0 \tau + \phi_S \frac{\tau^2}{2}, \\ \dot{\mathcal{P}}(\tau) &= \dot{\mathcal{P}}_0 + \phi_S \tau, \end{aligned} \tag{A.4}$$

upon setting the initial time to zero. For FC or BC motion, the equation of motion is a linear ordinary differential equation with constant coefficients [114]. Its solution is readily obtained and the trajectory parametrization reads

$$\begin{aligned} \mathcal{P}(\tau) &= \left(\mathcal{P}_0 - \frac{\phi_R}{\beta_R} \right) \cos \sqrt{\beta_R} \tau + \frac{\dot{\mathcal{P}}_0}{\sqrt{\beta_R}} \sin \sqrt{\beta_R} \tau + \frac{\phi_R}{\beta_R}, \\ \dot{\mathcal{P}}(\tau) &= \left(\frac{\phi_R}{\beta_R} - \mathcal{P}_0 \right) \sin \sqrt{\beta_R} \tau + \dot{\mathcal{P}}_0 \cos \sqrt{\beta_R} \tau, \end{aligned} \tag{A.5}$$

under the same assumption of zero initial time. Beyond the description of the bit trajectory, these analytical solutions can be used to calculate the time of occurrence of drilling mode transitions.

The $\mathsf{FF} \rightarrow \{\mathsf{FC}; \mathsf{SS}\}$ transitions take place at the closure of the bit/rock interface; that is, when

$$\mathcal{P}_u = \mathcal{P}_0 + \dot{\mathcal{P}}_0 \bar{\tau} + \phi_S \frac{\bar{\tau}^2}{2}, \tag{A.6}$$

where $\bar{\tau}$ is the generic notation for the transition occurrence time. The transition is thus expected to take place at

$$\bar{\tau} = \sqrt{\left(\frac{\dot{\mathcal{P}}_0}{\phi_S}\right)^2 + 2\frac{\mathcal{P}_u - \mathcal{P}_0}{\phi_S}} - \frac{\dot{\mathcal{P}}_0}{\phi_S}; \tag{A.7}$$

the argument of the square root is always positive given the restriction on the initial penetration, $\mathcal{P}_0 < \mathcal{P}_u$.

The $\mathsf{FC} \rightarrow \mathsf{BC}$ transition takes place when the bit velocity vanishes. The event occurrence time is given by

$$0 = (\phi_S - \mathcal{P}_0) \sin \bar{\tau} + \dot{\mathcal{P}}_0 \cos \bar{\tau}. \tag{A.8}$$

A closed-form solution can be obtained by reducing the sum of trigonometric functions to a single trigonometric function. Given the admissible domain of initial conditions, it reads

$$\bar{\tau} = \pi - \operatorname{acos} \frac{\phi_S - \mathcal{P}_0}{\sqrt{(\phi_S - \mathcal{P}_0)^2 + \dot{\mathcal{P}}_0^2}}. \tag{A.9}$$

When the system is in the BC mode, two transitions can take place with the bit entering either the FF mode if it bounces off the rock or the SS mode if its velocity vanishes during the BC mode. As was demonstrated in the energetic analysis of the drilling cycle, see Section 2.5, the latter condition is not expected during regular motion; it can only result from the initialization of the system in the BC mode with a specific choice of initial conditions. The former transition is defined by the condition $\mathcal{P}(\bar{\tau}) = \mathcal{P}_u$. It takes place at the smallest $\bar{\tau} > 0$ verifying

$$\sin\left(\sqrt{\gamma}\bar{\tau} + \tau_\phi\right) = -\frac{\phi_S}{\sqrt{\left(\gamma\left(\mathcal{P}_0 - \mathcal{P}_u\right) - \phi_S\right)^2 + \gamma \dot{\mathcal{P}}_0^2}}, \tag{A.10}$$

where τ_ϕ is defined by

$$\sin\tau_\phi = \frac{\gamma\left(\mathcal{P}_0 - \mathcal{P}_u\right) - \phi_S}{\sqrt{\left(\gamma\left(\mathcal{P}_0 - \mathcal{P}_u\right) - \phi_S\right)^2 + \gamma\dot{\mathcal{P}}_0^2}}, \quad \cos\tau_\phi = \frac{\sqrt{\gamma}\dot{\mathcal{P}}_0}{\sqrt{\left(\gamma\left(\mathcal{P}_0 - \mathcal{P}_u\right) - \phi_S\right)^2 + \gamma\dot{\mathcal{P}}_0^2}}. \tag{A.11}$$

Given the restriction on the initial velocity, $\dot{\mathcal{P}}_0 < 0$, τ_ϕ belongs to the second or third quadrant of the trigonometric circle. The occurrence of the transition is obviously contingent on the right-hand side of equation (A.10) having less than unit magnitude. The occurrence time of the transition to the SS mode can be derived following the same procedure by imposing a zero velocity at the event time. It is given by

$$\bar{\tau} = \frac{3\pi}{2} - \tau_\phi. \tag{A.12}$$

With the possibility of calculating the time of event occurrences, the event-driven scheme reduces to, for a given mode and initial conditions, identifying which event occurs first along the time axis (this includes percussive activation that is an event depending on the time variable only) and which drilling mode comes next. Looping on this procedure provides the required time integration procedure.

A.2 Shooting method

A variety of methods are available to compute periodic solutions of ordinary differential equations. Indeed, these are nothing else but a particular class of boundary value problems along the time axis with equal initial and final state vectors. The entire panoply of tools, *e.g.*, finite elements, finite differences, collocation or the (multiple) shooting methods [43, 115], are thus applicable. However, given the nonsmooth nature of the drifting oscillator trajectory and the availability of an efficient integration procedure, the shooting method imposes itself as the method of choice to compute periodic orbits. Some of the important aspects of its implementation for the drifting oscillator model are given below.

Let $\boldsymbol{\Phi}(\tau, \tau_0)$ denote the state-transition matrix that expresses the state of the system $\boldsymbol{\mathcal{P}}$ at time τ from its state at time τ_0 [116],

$$\boldsymbol{\mathcal{P}}(\tau) = \boldsymbol{\Phi}(\tau, \tau_0)\boldsymbol{\mathcal{P}}(\tau_0), \tag{A.13}$$

where $\boldsymbol{\mathcal{P}}$ is the vertical (column) concatenation of the bit penetration and velocity, $\mathcal{P}, \dot{\mathcal{P}}$, possibly augmented by the history variable associated with the initial drilling mode. The shooting method is based on finding initial conditions $\boldsymbol{\mathcal{P}}(\tau_0)$ (the zeros of the shooting function) that ensure the trajectory verifies a periodicity condition on the state variables, *i.e.*,

$$\mathbf{s}(\boldsymbol{\mathcal{P}}_0) := (\boldsymbol{\Phi}(n\tau_a, \tau_0) - \mathbf{I})\, \boldsymbol{\mathcal{P}}(\tau_0), \tag{A.14}$$

where the final state is evaluated by integrating the system dynamics from the set of given initial conditions. The existence of these zeros is conditioned by the existence of a periodic solution for the preset period $n\tau_a$ of the limit cycle (n must be arbitrarily chosen as the system is non-autonomous and periodic solutions necessarily have a period that is an integer multiple of the external forcing period [39]) and the considered initial point. For obvious versatility reasons, the initial point must therefore be chosen in such a way that it belongs to all (periodic) trajectories. One such point is the peak penetration point. Under this arbitrary choice that corresponds to zero velocity, the unknowns $\boldsymbol{\mathcal{P}}_0$ of the shooting function are the initial (peak) penetration $\mathcal{P}_0$ and the time shift associated with the percussive activation τ_s. However, as this point coincides with a switch of the vector field, instabilities due to a discontinuous Jacobian matrix might render difficult the numerical finding of these zeros by a Newton-based iterative procedure. Indeed, the required Jacobian matrix

$$\mathbf{J} := \frac{\partial \mathbf{s}}{\partial \boldsymbol{\mathcal{P}}_0} = \frac{\partial \boldsymbol{\Phi}}{\partial \boldsymbol{\mathcal{P}}_0} - \mathbf{I} \tag{A.15}$$

involves the derivative of the state-transition matrix, *i.e.*, the fundamental solution matrix of the variational equivalent to the original model, that typically experiences discontinuities at points of nonsmoothness along a trajectory. These discontinuities are quantified by the so-called saltation matrix [39, 45, 46] that can be evaluated analytically in this simple model. Augmenting the state vector with the peak penetration, $\boldsymbol{\mathcal{P}} = \left[\mathcal{P}\,;\,\dot{\mathcal{P}}\,;\,\mathcal{P}_p\right]$, the vector fields in the FC and BC modes are respectively given by

$$\mathbf{f}_{\mathsf{FC}}(\boldsymbol{\mathcal{P}}) := \begin{pmatrix} \dot{\mathcal{P}} \\ \phi_S - \mathcal{P} \\ 0 \end{pmatrix}, \qquad \mathbf{f}_{\mathsf{BC}}(\boldsymbol{\mathcal{P}}) := \begin{pmatrix} \dot{\mathcal{P}} \\ \phi_S + (\gamma - 1)\mathcal{P}_p - \gamma \mathcal{P} \\ 0 \end{pmatrix}, \tag{A.16}$$

and the update of the peak penetration can be incorporated in a linear reset map, so that at peak penetration $\boldsymbol{\mathcal{P}}_p^+ = \mathbf{r}_{,\boldsymbol{\mathcal{P}}}\boldsymbol{\mathcal{P}}_p^-$ with

$$\mathbf{r}_{,\boldsymbol{\mathcal{P}}} := \begin{pmatrix} 1 & 0 & 0 \\ 0 & 1 & 0 \\ 1 & 0 & 0 \end{pmatrix}. \tag{A.17}$$

The occurrence of peak penetration being given by the condition of vanishing bit velocity, $q(\boldsymbol{\mathcal{P}}) := \dot{\mathcal{P}}$, application of the saltation matrix definition

$$\mathbf{S} := \mathbf{r}_{,\boldsymbol{\mathcal{P}}} + \frac{\mathbf{f}_{\mathsf{BC}}(\mathbf{r}_{,\boldsymbol{\mathcal{P}}}\boldsymbol{\mathcal{P}}_*) - \mathbf{r}_{,\boldsymbol{\mathcal{P}}}\mathbf{f}_{\mathsf{FC}}(\boldsymbol{\mathcal{P}}_*)}{q_{,\boldsymbol{\mathcal{P}}}^T(\boldsymbol{\mathcal{P}}_*)\mathbf{f}_{\mathsf{FC}}(\boldsymbol{\mathcal{P}}_*)} q_{,\boldsymbol{\mathcal{P}}}^T(\boldsymbol{\mathcal{P}}_*), \tag{A.18}$$

where $q_{,\boldsymbol{\mathcal{P}}} := \partial q/\partial \boldsymbol{\mathcal{P}}$, leads to

$$\mathbf{S} = \mathbf{r}_{,\boldsymbol{\mathcal{P}}} \neq \mathbf{I}. \tag{A.19}$$

Thus, $\partial \boldsymbol{\Phi}/\partial \boldsymbol{\mathcal{P}}_0$ and, *a fortiori*, $\mathbf{J}$ are continuous at peak penetration but for their third row. The use of a Jacobian-based solver in cunjunction with the initial point corresponding to peak penetration is then only possible if the periodicity on the history variable $\mathcal{P}_p$ is verified *a posteriori*. This is not much of a problem since if periodicity on $\mathcal{P}$ is achieved, periodicity on $\mathcal{P}_p$ is automatically achieved as well. As such, the shooting function reads

$$\mathbf{s}(\mathcal{P}_0, \tau_s) := \begin{pmatrix} \mathcal{P}(n\tau_a, \mathcal{P}_0, \tau_s) - \mathcal{P}_0 \\ \dot{\mathcal{P}}(n\tau_a, \mathcal{P}_0, \tau_s) \end{pmatrix}. \tag{A.20}$$

A.3 Continuation procedure

It is a known fact that the shooting method can prove sensitive to the choice of initial conditions ($\mathcal{P}_0, \tau_s$ in the present case) and exhibit a rather small basin of attraction [115]. To limit robustness issues in bifurcation analyses, the shooting procedure can be embedded in a so-called path-following or continuation procedure [43, 117, 118].

A common approach is based on the pseudo-arclength parametrization of the manifold to be continued (here the set of initial conditions) in the parameter space [119]; this method is also known as the Riks procedure in the finite element community [120]. This reparametrization of the path to follow enables the robust handling of turning points. Following this approach, the bifurcation parameter (we only consider co-dimension one

continuation) is declared as an unknown to the continuation problem and superseded by the independent arclength coordinate s; a constraint is then appended to the shooting function to close the problem which becomes equivalent to finding the zeros of the augmented shooting function

$$\left| \begin{array}{l} \mathbf{s}(\mathcal{P}_0, \tau_s) = 0, \\ \Delta\mathcal{P}_0^2 + \Delta\tau_s^2 = \Delta s^2, \end{array} \right. \tag{A.21}$$

where the operator Δ, when appended to a variable, denotes the difference between its values at the current point and at the previously computed one. With the knowledge of a single point along the path, a predictor-corrector root-solving procedure can be set up for the efficient numerical solving of the continuation problem. Several procedures have been developed, based on various combinations of predictor and corrector formulations [43].

Control of the arclength step Δs as a function of the branch curvature and of the number of iterations to convergence is required to accurately capture the followed path. A strategy similar to that in place in the commercial finite element software ABAQUS [121] was implemented.

A.4 Stability of periodic orbits

Similarly to the stability of fixed points of nonlinear dynamical systems, the stability of periodic orbits can be studied by the analysis of the eigenvalues of a matrix associated with a variational equivalent to the original system. This matrix characterizes the flow and, in particular, the growth of perturbations along the limit cycle. It is usually referred to as the monodromy matrix and, in fact, is nothing else than the Jacobian matrix of the Poincaré map of the limit cycle at the considered initial point of the limit cycle. The periodic orbit is asymptotically stable if all its eigenvalues, known as the Floquet multipliers, are within the unit circle, stable in the sense of Lyapunov if all eigenvalues are within the unit circle and the ones with unit magnitude have single multiplicity, and unstable otherwise [39, 43, 122].

In theory, the monodromy matrix can be constructed for piecewise systems by composition of the fundamental solution and saltation matrices of the associated variational problem, following the mode sequence and transitions along the periodic orbit. The

presence of history variables in the drifting oscillator model, however, severely impedes the tractability of the theoretical approach, for their derivatives with respect to the state variables enter the definition of the saltation matrix [36] and closed-form expressions are not always available. Instead, a numerical procedure, based on a finite difference approximation of the monodromy matrix, has been implemented.

Let $\mathbf{M}_{n\tau_a}$ denote the 2×2 monodromy matrix associated with a period-n limit cycle of the drifting oscillator model. If $\delta\boldsymbol{\mathcal{P}}_0$ denotes a vector of perturbations on the initial penetration and velocity corresponding to this periodic orbit (at peak penetration), then the perturbation after one limit cycle period has become

$$\delta\boldsymbol{\mathcal{P}}_{n\tau_a} = \mathbf{M}_{n\tau_a}\delta\boldsymbol{\mathcal{P}}_0; \tag{A.22}$$

see the illustration in Figure A.1. Therefore, the components of the monodromy matrix can be identified via numerical integration over a single limit cycle period, starting from perturbed initial conditions, on the basis of two linearly independent perturbation vectors. Nevertheless, to ensure a correct evaluation of the monodromy matrix, an initialization of history variable $\mathcal{P}_p$, consistent with the system dynamics, must be achieved when the system is initialized in the BC mode. Assuming that no percussive penetration takes place between the point of peak penetration and the perturbed initial condition in BC mode, the consistent peak penetration can be expressed as

$$\mathcal{P}_p(\mathcal{P}_0, \dot{\mathcal{P}}_0) = \begin{cases} \frac{(\gamma-1)\mathcal{P}_0 - \phi_S - \sqrt{(\mathcal{P}_0-\phi_S)^2 - (\gamma-2)\dot{\mathcal{P}}_0^2}}{\gamma-2}, & \text{if } \gamma \neq 2, \\ \mathcal{P}_0 - \frac{\dot{\mathcal{P}}_0^2}{2(\phi_S - \mathcal{P}_0)}, & \text{if } \gamma = 2. \end{cases}$$

This result follows from energetic considerations. In case a percussive activation does take place, velocity perturbations can be chosen positive so as to avoid the redefinition of $\mathcal{P}_p$. In such situation, it is, nonetheless, likely that the shooting procedure will fail to capture the periodic solution, as the presence of a state discontinuity in the close vicinity of the initial limit cycle point can lead to a discontinuous dependence on initial conditions that might perturb the iterative solver.

A.5 Example of bifurcation analysis

Using the tools briefly described in this appendix, a bifurcation analysis was conducted and reported in [32]. The reference configuration, $(\gamma, \tau_a, \phi_s, \dot{\mathcal{P}}_{\mathsf{SS}}) = (10, 10, 0.1, 0.09)$,

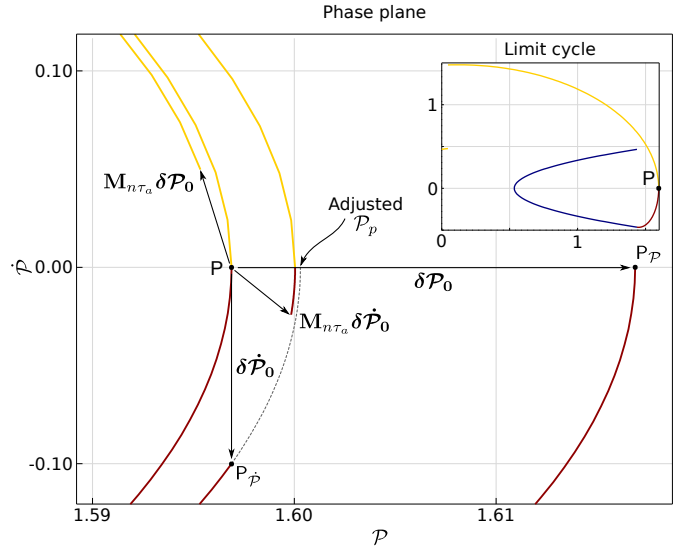

Figure A.1: Example of a 1/1 reference limit cycle and perturbed trajectories for the numerical computation of the monodromy matrix.

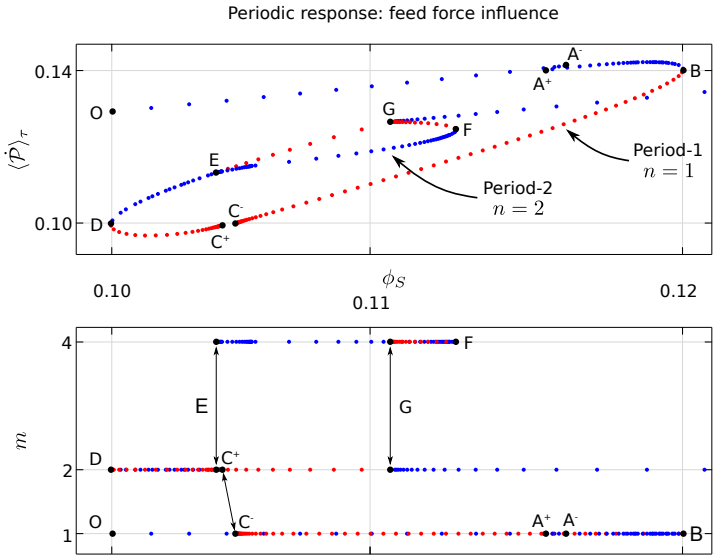

Figure A.2: Bifurcation analysis around $(\gamma, \tau_a, \dot{\mathcal{P}}_{\mathsf{SS}}) = (10, 10, 0.09)$, $\phi_S \in [0.10, 0.12]$. Blue (red) dots correspond to (un)stable limit cycles.

being quite different from the one studied in Section 2.6 that is of interest in this thesis, we only report some of these results in this appendix, to illustrate the power of the implemented numerical tools.

Figure A.2 shows the evolution of the average rate of penetration with the feed force, including the stability of the periodic response (red dots correspond to unstable periodic solutions and blue ones to stable orbits), its periodicity n and the number of drilling cycles completed over one limit cycle m. Interestingly, the analysis reveals the possible coexistence of stable attractors and shows clues of optimal drilling configurations, thereby sustaining the dynamics justification to their existence. Periodic solutions are seen to coexist in this range of parameters; these differ by their average number of drilling cycles or their stability. The diagram also shows the discontinuous characteristic certain bifurcations present. This feature is to be related to the non-commutativity of the percussive activation and the instantaneous dissipation. Following the period-1 response from its leftmost point, point O, we see that the solution undergoes bifurcations of different kinds. At point A, the bifurcation diagram is discontinuous. It corresponds to the transition between periodic sequence $(\mathsf{FC} \to \mathsf{BC} \to \mathsf{FF} \to [\![\dot{\mathcal{P}}_i]\!] \to \mathsf{FF})_{\circlearrowleft}$ at point A^- and $(\mathsf{FC} \to \mathsf{BC} \to \mathsf{FF} \to \mathsf{FC} \to [\![\dot{\mathcal{P}}_i]\!])_{\circlearrowleft}$ at point A^+, when the percussive activation takes place at the moment the bit contacts the rock at the transition $\mathsf{FF} \to \mathsf{FC}$. Point B corresponds to a loss of stability of the 1/1 limit cycle through a fold bifurcation. Another discontinuity occurs at point C with the apparition of a second drilling cycle within the periodic solution. This unstable 2/1 limit cycle then regains stability at point D via a second fold bifurcation and loses it again at point E, consequently to a flip bifurcation. Point E thus also corresponds to the origin of a branch of period-2 orbits. They have an average number of drilling cycles 4/2, are stable on branch EF and unstable along FG. A fold bifurcation at point F is responsible for the change of stability. The 2/1 solution is again stable from point G on to larger values of the dead load ϕ_S. Jumps from one attractor to another may thus be expected in this region, if the system is subjected to external perturbations, likely engendering complex dynamics.

Appendix B

Collinear longitudinal impact

Under the assumption of timescale separation that justifies the two-body rigid model, see Section 3.3, the waves generated by percussive activations, which propagate in the piston and the bit, are not resolved. These, however, play a critical role on the duration of the contact between the piston and the bit during interaction phases as well as on their post-interaction average velocities. To account for this influence in the rigid model, the reset map that defines the post-contact velocities of the piston and the bit as a function of their pre-contact velocities and the drilling mode at the bit/rock interface is defined as the average velocities of the elastic bodies at the end of the contact phase, as given by the exact wave propagation solution to the problem of collinear longitudinal impact of two cylinders, one of them being constrained by an elastic support.

B.1 Problem statement

The model problem illustrated in Figure B.1 is considered. Both cylinders are elastic and have identical properties but their length, whose ratio is given by $\omega_{21} \in (1, 2)$; it reflects the typical bit/piston length ratios of physical devices. The leftmost bar is assumed free at both ends whereas the rightmost one is constrained by an elastic support of stiffness η at its right end. The gap function measuring the distance between the two cylinders is set to zero initially and the cylinders are given uniform initial velocities, denoted by $\mathcal{V}_1^-$ (the left bar is referred to by index 1) and $\mathcal{V}_2^-$ (the right bar is referred to by index 2),

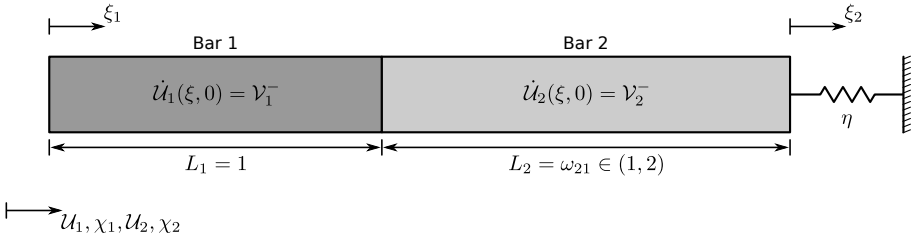

Figure B.1: Collinear longitudinal impact of similar bars with an elastic boundary condition at the rightmost bar end, scaled model problem.

that are constrained by

$$\mathcal{V}_1^- > \mathcal{V}_2^-, \tag{B.1}$$

in algebraic value, to ensure the start of the contact phase at time $\tau = 0$. No external loading is considered as, under the assumption of timescale separation underlying the rigid two-body model, the impulse of external loads is negligible in front of the percussive activation, over the duration of the contact phase. We further consider that the model problem is normalized, so that traveling waves have unit propagation speed.

In the absence of external forcing, the wave equation ruling the motion of the bars simplifies to

$$\ddot{\mathcal{U}}_i(\xi_i,\tau) = \mathcal{U}_i''(\xi_i,\tau), \quad i \in \{1,2\}, \tag{B.2}$$

on domains $(\xi_1,\tau) \in [0,1]\times\mathbb{R}^+$ and $(\xi_2,\tau) \in [-\omega_{21},0]\times\mathbb{R}^+$ for rods 1 and 2, respectively. Again, $\mathcal{U}_i(\xi_i,\tau)$ represents the displacement of a slice of material located at coordinate ξ_i, at time τ. It is measured in the global axes and relates the material coordinate of a point ξ_i to its position χ_i. The overhead dots denote time differentiation whereas prime symbols refer to space differentiation. The initial and boundary conditions read

$$\mathcal{U}_1(\xi_1,0) = 0, \qquad \mathcal{U}_2(\xi_2,0) = 0, \tag{B.3}$$

$$\dot{\mathcal{U}}_1(\xi_1,0) = \mathcal{V}_1^-, \qquad \dot{\mathcal{U}}_2(\xi_2,0) = \mathcal{V}_2^-, \tag{B.4}$$

and

$$\frac{\partial \mathcal{U}_1}{\partial \xi_1}(0,\tau) = 0, \tag{B.5}$$

$$0 \leq -\frac{\partial \mathcal{U}_1}{\partial \xi_1}(1,t) \perp \mathcal{N}_C(\tau) \geq 0, \tag{B.6}$$

$$0 \leq \mathcal{N}_C(\tau) \perp -\frac{\partial \mathcal{U}_2}{\partial \xi_2}(-\omega_{21},\tau) \geq 0, \tag{B.7}$$

$$\frac{\partial \mathcal{U}_2}{\partial \xi_2}(0,\tau) + \eta \mathcal{U}_2(0,\tau) = 0. \tag{B.8}$$

The complementarity conditions (B.6)-(B.7) express the unilateral nature of the contact constraint. Either the interface is open, with a positive gap and a vanishing contact strain

$$\mathcal{N}_C(\tau) := \mathcal{U}_2(-\omega_{21},\tau) - \mathcal{U}_1(1,\tau) > 0, \tag{B.9}$$

$$\mathcal{U}'_C(\tau) := \frac{\partial \mathcal{U}_1}{\partial \xi_1}(1,\tau) = \frac{\partial \mathcal{U}_2}{\partial \xi_2}(-\omega_{21},\tau) = 0, \tag{B.10}$$

and the boundary surfaces behave as free surfaces. Or it is closed with a zero gap and a negative contact strain

$$\mathcal{N}_C(\tau) = 0, \tag{B.11}$$

$$\mathcal{U}'_C(\tau) \leq 0; \tag{B.12}$$

the two rods then behave as one unique continuum since they have equal impedance [53]. Given the initial closure of the contact interface and the restriction on the initial velocities (B.1), the contact interface remains closed until time τ_C at which either the compressive strain vanishes at the contact interface

$$\mathcal{U}'_C(\tau_C) = 0, \tag{B.13}$$

or the gap velocity becomes positive

$$\dot{\mathcal{N}}_C(\tau_C) > 0. \tag{B.14}$$

As the origin of time coincides with the closure of the contact interface, time instant τ_C also corresponds to the duration of closed contact between the two rods.

B.2 d'Alembert's solution to the wave equation

The scalar wave equation (B.2) can be solved by introducing d'Alembert's Einsatz that dissociates the leftward and rightward traveling components of the problem solution

$$\mathcal{U}_i(\xi_i, \tau) = \mathcal{F}_i(\tau - \xi_i) + \mathcal{G}_i(\tau + \xi_i), \quad i \in \{1, 2\}. \tag{B.15}$$

The displacement field in a rod is expressed as the sum of two wave functions whose argument combines the spatial and temporal variables. This combination indicates that wave function $\mathcal{F}_i$ is propagated rightwards without alteration of the wave form and that wave function $\mathcal{G}_i$ is propagated leftwards, unaltered as well.

B.3 Boundary conditions as input/output conditions

Given the specific structure of the d'Alembert solution (B.15), each boundary surface can be interpreted as an input/output system with $\mathcal{F}_i$ or $\mathcal{G}_i$ alternatively playing the role of input or output, depending on the boundary location.

At a free boundary surface, the stress is zero, at all times, and so is the axial strain on the leftmost rod at $\xi_1 = 0$

$$\frac{\partial \mathcal{U}_1}{\partial \xi_1}(0, \tau) = -\mathcal{F}_1'(\tau) + \mathcal{G}_1'(\tau) = 0; \tag{B.16}$$

the prime symbol denotes differentiation with respect to the wave function argument. The free end boundary condition is thus equivalent to the static input/output condition

$$\mathcal{F}_1'(\tau) = \mathcal{G}_1'(\tau); \tag{B.17}$$

the derivative of the outgoing wave function is equal to the derivative of the ingoing wave function.

At the elastically supported boundary, the incoming wave function is $\mathcal{F}_2(\tau)$ and $\mathcal{G}_2(\tau)$ is the outgoing one. The input/output equation takes the form

$$\mathcal{G}_2'(\tau) + \eta \mathcal{G}_2(\tau) = \mathcal{F}_2'(\tau) - \eta \mathcal{F}_2(\tau). \tag{B.18}$$

It can be solved by use of the unilateral Laplace transform to yield

$$\mathcal{G}_2(\tau) = \mathcal{F}_2(t) - 2\eta \int_0^\tau \mathrm{e}^{-\eta(\tau - \tau')} \mathcal{F}_2(\tau') \, \mathrm{d}\tau'; \tag{B.19}$$

the outgoing wave function is equal to the incoming one, altered by its convolution with an exponential kernel.

The boundary conditions at the contact interface need not be considered prior to the opening of the contact interface at $\tau = \tau_C$.

B.4 Reflected wave at elastically supported end

In light of the above elements, the solution to the wave propagation problem can be worked out by identifying the wave functions defined by the initial conditions and propagating them in time. Given that both rods are initially stress free, a condition similar to that described in equation (B.16) is verified on the entire spatial domain at $t = 0$. Noting that the velocity reads

$$\dot{\mathcal{U}}_i(\xi_i, \tau) = \frac{\partial \mathcal{U}_i}{\partial \tau}(\xi_i, \tau) = \mathcal{F}_i'(\tau - \xi_i) + \mathcal{G}_i'(\tau + \xi_i), \tag{B.20}$$

it readily follows that

$$\mathcal{F}_1'(\xi_1, 0) = \mathcal{G}_1'(\xi_1, 0) = \frac{\mathcal{V}_1^-}{2}, \tag{B.21}$$

$$\mathcal{F}_2'(\xi_2, 0) = \mathcal{G}_2'(\xi_2, 0) = \frac{\mathcal{V}_2^-}{2}. \tag{B.22}$$

This initial configuration corresponds to the scenario depicted at the top of Figure B.2.

To propagate the solution in time, the reflected wave at the elastically supported end must be calculated. By integrating the initial condition, we obtain

$$\mathcal{F}_2(\tau) = \frac{\mathcal{V}_2^-}{2}\tau. \tag{B.23}$$

This input signal is valid for $\tau \in [0, \omega_{21}]$. At $\tau = \omega_{21}$, the wave function $\mathcal{F}_1$ originating in rod 1 arrives at the elastically supported boundary and the input function must be redefined as

$$\mathcal{F}_2(\tau) = \frac{\mathcal{V}_2^-}{2} + \frac{\mathcal{V}_1^-}{2}(\tau - 1). \tag{B.24}$$

This expression is valid for $\tau \in (1, \tau_C + \omega_{21}]$. Further definition in time is thus not required.

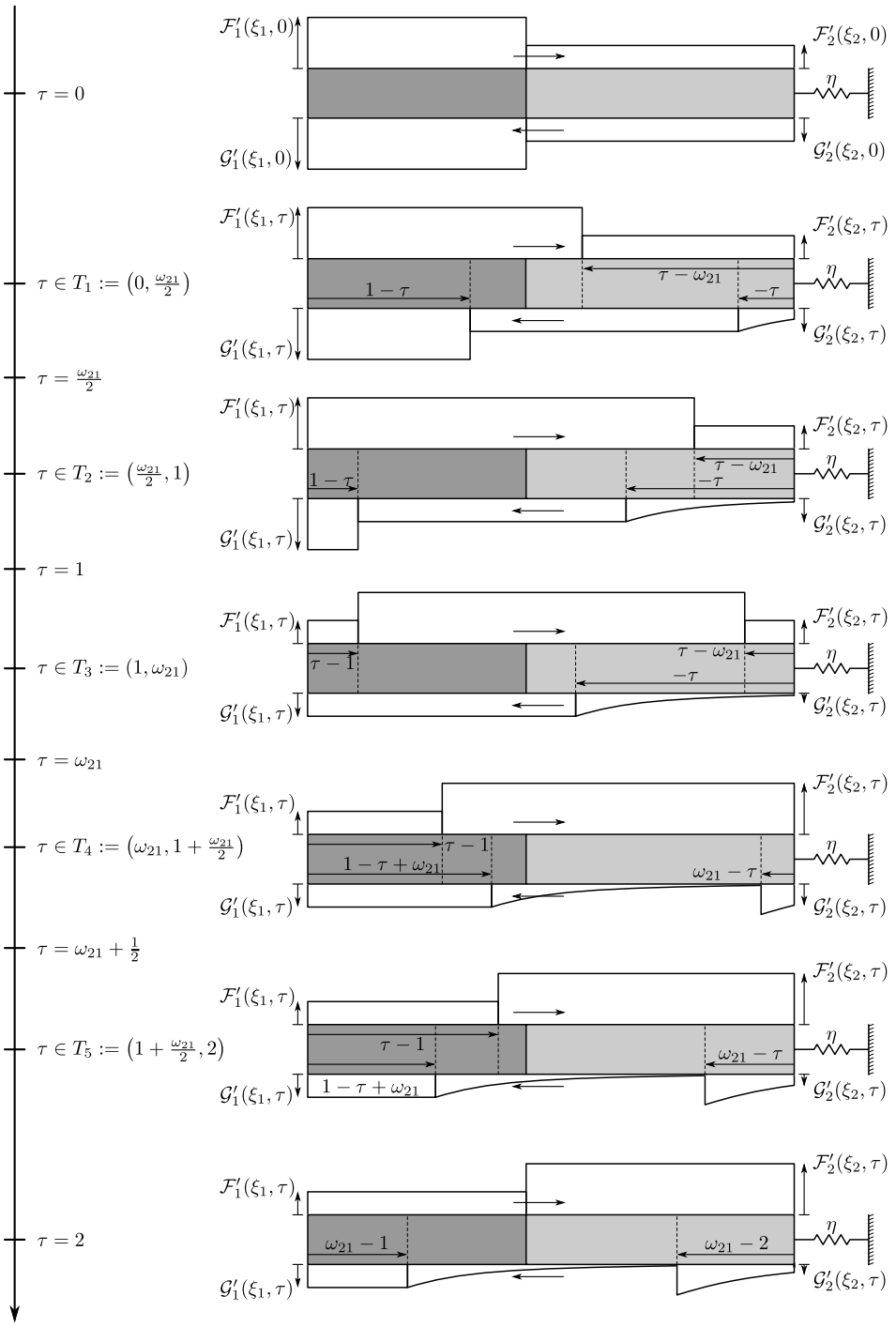

Figure B.2: Evolution of the wave functions and localization of the wave fronts for each motion phase in the time interval $T = [0, 2]$, assuming $\tau_C = 2$.

Following this piecewise definition, the wave function of the reflected wave can be calculated via (B.19). It is obviously a piecewise-defined function as well

$$\mathcal{G}_2(\tau) = \mathcal{V}_2^- \left(\frac{1 - \mathrm{e}^{-\eta\tau}}{\eta} - \frac{\tau}{2} \right) \tag{B.25}$$

for $\tau \in [0, \omega_{21}]$, and

$$\mathcal{G}_2(\tau) = \mathcal{V}_2^- \left(\frac{\mathrm{e}^{-\eta(\tau-\omega_{21})} - \mathrm{e}^{-\eta\tau}}{\eta} - \frac{\omega_{21}}{2} \right) + \mathcal{V}_1^- \left(\frac{\omega_{21} - \tau}{2} + \frac{1 - \mathrm{e}^{-\eta(\tau-\omega_{21})}}{\eta} \right), \tag{B.26}$$

for $t \in [\omega_{21}, \tau_C]$; its derivative reads

$$\mathcal{G}_2'(\tau) = \begin{cases} \mathcal{V}_2^- \left(\mathrm{e}^{-\eta\tau} - \frac{1}{2} \right) & \tau \in [0, \omega_{21}], \\ \mathcal{V}_2^- \left(\mathrm{e}^{-\eta t} - \mathrm{e}^{-\eta(\tau-\omega_{21})} \right) + \mathcal{V}_1^- \left(\mathrm{e}^{-\eta(\tau-\omega_{21})} - \frac{1}{2} \right) & \tau \in (\omega_{21}, \tau_c]. \end{cases} \tag{B.27}$$

The wave function is continuous but has a discontinuous derivative at $\tau = \omega_{21}$, as shown by the limiting behaviors

$$\lim_{\tau \to \omega_{21}^-} \mathcal{G}_2'(\tau) = \mathcal{V}_2^- \left(\mathrm{e}^{-\eta\omega_{21}} - \frac{1}{2} \right), \tag{B.28}$$

$$\lim_{\tau \to \omega_{21}^+} \mathcal{G}_2'(\tau) = \mathcal{V}_2^- \left(\mathrm{e}^{-\eta\omega_{21}} - 1 \right) + \frac{\mathcal{V}_1^-}{2}. \tag{B.29}$$

Interestingly, the stiffness parameter η plays an important role on these limits. The asymptotic cases $\eta \ll 1$ and $\eta \gg 1$ yield completely different behaviors, with the limits at $t \to 1^{\pm}$ reading

$$\eta \to 0 \qquad \lim_{\tau \to \omega_{21}^-} \mathcal{G}_2'(\tau) = \frac{\mathcal{V}_2^-}{2}, \qquad \lim_{\tau \to \omega_{21}^+} \mathcal{G}_2'(\tau) = \frac{\mathcal{V}_1^-}{2}, \tag{B.30}$$

$$\eta \to \infty \qquad \lim_{\xi \to \omega_{21}^-} \mathcal{G}_2'(\tau) = -\frac{\mathcal{V}_2^-}{2}, \qquad \lim_{\tau \to \omega_{21}^+} \mathcal{G}_2'(\tau) = \frac{\mathcal{V}_1^-}{2} - \mathcal{V}_2^-. \tag{B.31}$$

B.5 Duration of the contact phase

With the knowledge of the reflected waves at the boundary surfaces, propagating the solution is a mere graphical exercise, which is carried out in Figure B.2. The reported solution assumes that contact is persistent until $\tau_C = 2$. At that instant, the gap velocity $\dot{\mathcal{N}}_C(\tau)$ becomes positive due to the arrival of a wave front at the contact interface across

which a positive velocity jump exists, thereby leading to the opening of the contact interface.

The loss of contact can occur earlier for specific configurations, however. To circumscribe these conditions, let us track the evolution of the contact strain $\mathcal{U}'_C(\tau)$. From the d'Alembert solution, it is given by

$$\mathcal{U}'_C(\tau) = -\mathcal{F}'_1(\tau - 1) + \mathcal{G}'_1(\tau + 1) = -\mathcal{F}'_2(\tau + \omega_{21}) + \mathcal{G}'_2(\tau - \omega_{21}). \tag{B.32}$$

According to the graphical composition, two cases must be studied.

The first one corresponds to $\tau \in [0, \omega_{21}]$. During that time interval, the contact strain is given by

$$\mathcal{U}'_C(\tau) = \frac{\mathcal{V}_2^- - \mathcal{V}_1^-}{2}. \tag{B.33}$$

A compressive strain is thus observed whenever $\mathcal{V}_2^- < \mathcal{V}_1^-$ is verified, which is nothing else than the condition (B.1) for impact at initial time. Accordingly, the opening of the contact interface cannot take place during this time interval.

The second case to study corresponds to the time interval $\tau \in (\omega_{21}, 2)$. During that time lapse, the contact strain is given by

$$\mathcal{U}'_C(\tau) = \left(\mathrm{e}^{-\eta(\tau - \omega_{21})} - \frac{1}{2}\right)\mathcal{V}_2^- - \frac{\mathcal{V}_1^-}{2}. \tag{B.34}$$

Separation of the contacting surfaces is possible if the strain vanishes in the given time interval; that is, the contact duration τ_C is equal to

$$\tau_C^* = \omega_{21} - \frac{1}{\eta}\ln\left(\frac{v_1^-}{2v_2^-} + \frac{1}{2}\right) \tag{B.35}$$

if $\tau_C^* \in (\omega_{21}, 2)$. The condition $\tau_C^* > \omega_{21}$ is verified only if the initial velocities verify the constraint

$$\frac{\mathcal{V}_1^-}{\mathcal{V}_2^-} < 1. \tag{B.36}$$

Under the restriction on the initial velocities that guarantee the impact (B.1), this condition can only be met if the initial velocity of the rightmost rod is negative. Thus, for positive initial velocities $\mathcal{V}_2^- > 0$, the contact phase always lasts $\tau_C = 2$. The condition $\tau_C^* < 2$ translates into

$$\frac{\mathcal{V}_1^-}{\mathcal{V}_2^-} > 2\mathrm{e}^{\eta(\omega_{21} - 2)} - 1. \tag{B.37}$$

Again, this condition leads to sensible results for negative initial velocities of rod 2 only. The contact duration is given by τ_C^* if, for a given initial velocity $\mathcal{V}_2^- < 0$, the initial velocity of rod 1, $\mathcal{V}_1^-$, belongs to

$$\mathcal{V}_2^- < \mathcal{V}_1^- < \mathcal{V}_2^- \left(2\mathrm{e}^{\eta(\omega_{21}-2)} - 1\right). \tag{B.38}$$

Given the restriction on the values of the length ratio $\omega_{21} \in (1, 2)$, the argument of the exponential term in the rightmost member is negative, leading to this member being either positive or negative. The critical stiffness parameter

$$\eta^* = \frac{\ln 2}{2 - \omega_{21}} \tag{B.39}$$

sets the limit between positive ($\eta < \eta^*$) and negative ($\eta > \eta^*$) members. Also, from equation (B.38), the asymptotic behaviors $\eta \ll 1$ and $\eta \gg 1$ can be assessed. In the former case, the term in parentheses is close to 1 and the sector in which $\tau_C = \tau_C^*$ tends to vanish. In the latter case, the term in parentheses is close to -1 and the sector in which $\tau_C = \tau_C^*$ is a quarter of the $(\mathcal{V}_2^-, \mathcal{V}_1^-)$-plane. Figure B.3 shows the influence of the initial velocities on the contact duration, for $\eta \in \{10^{-1}, 10^0, 10^1\}$. The asymptotic behaviors are well observable.

B.6 Velocity field

From the knowledge of the wave function derivatives, the velocity field on both rods can be constructed by use of (B.20). Table B.1 lists their evolution as a function of time and space, and parameters η, ω_{21}.

B.7 Reset map

We define the reset map relating the post-contact velocities to the pre-contact ones as the average velocity of each bar, at the end of the contact phase

$$\mathcal{V}_1^+ = \frac{1}{L_1} \int_0^{L_1} \mathcal{V}_1(\xi_1, \tau_C)\, \mathrm{d}\xi_1, \tag{B.40}$$

$$\mathcal{V}_2^+ = \frac{1}{L_2} \int_{-L_2}^{0} \mathcal{V}_2(\xi_2, \tau_C)\, \mathrm{d}\xi_2. \tag{B.41}$$

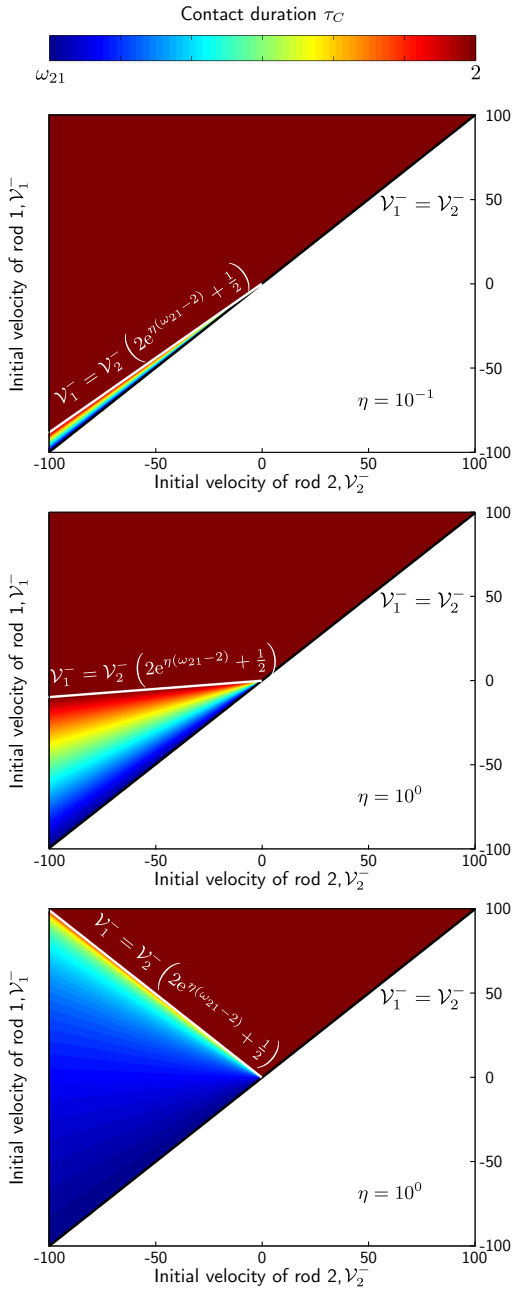

Figure B.3: Contact duration τ_C as a function of stiffness parameter η. The length ratio is set to $\omega_{21} = 1.25$ in the above illustrations.

$\tau \in (0, \omega_{21}/2]$				
Bar 1	ξ_1	$[0, 1-\tau]$	$[1-\tau, 1]$	
	$\dot{u}_1$	$\mathcal{V}_1^-$	$\frac{\mathcal{V}_1^- + \mathcal{V}_2^-}{2}$	
Bar 2	ξ_2	$[-\omega_{21}, \tau-\omega_{21}]$	$[\tau-\omega_{21}, -\tau]$	$[-\tau, 0]$
	$\dot{u}_2$	$\frac{\mathcal{V}_1^- + \mathcal{V}_2^-}{2}$	$\mathcal{V}_2^-$	$\mathcal{V}_2^- \mathrm{e}^{-\eta(\tau+\xi_2)}$
$\tau \in (\omega_{21}/2, 1]$				
Bar 1	ξ_1	$[0, 1-\tau]$	$[1-\tau, 1]$	
	$\dot{u}_1$	$\mathcal{V}_1^-$	$\frac{\mathcal{V}_1^- + \mathcal{V}_2^-}{2}$	
Bar 2	ξ_2	$[-\omega_{21}, -\tau]$	$[-\tau, \tau-\omega_{21}]$	$[\tau-\omega_{21}, 0]$
	$\dot{u}_2$	$\frac{\mathcal{V}_1^- + \mathcal{V}_2^-}{2}$	$\frac{1}{2}\mathcal{V}_1^- + \mathcal{V}_2^- \left(\mathrm{e}^{-\eta(\tau+\xi_2)} - \frac{1}{2}\right)$	$\mathcal{V}_2^- \mathrm{e}^{-\eta(\tau+\xi_2)}$
$\tau \in (1, \omega_{21}]$				
Bar 1	ξ_1	$[0, \tau-1]$	$[\tau-1, 1]$	
	$\dot{u}_1$	$\mathcal{V}_2^-$	$\frac{\mathcal{V}_1^- + \mathcal{V}_2^-}{2}$	
Bar 2	ξ_2	$[-\omega_{21}, -\tau]$	$[-\tau, \tau-\omega_{21}]$	$[\tau-\omega_{21}, 0]$
	$\dot{u}_2$	$\frac{\mathcal{V}_1^- + \mathcal{V}_2^-}{2}$	$\frac{\mathcal{V}_1^- - \mathcal{V}_2^-}{2} + \mathcal{V}_2^- \mathrm{e}^{-\eta(\tau+\xi_2)}$	$\mathcal{V}_2^- \mathrm{e}^{-\eta(\tau+\xi_2)}$
$t \in (\omega_{21}, \omega_{21}/2+1]$				
Bar 1	ξ_1	$[0, \tau-1]$	$[\tau-1, 1-\tau+\omega_{21}]$	$[1-\tau+\omega_{21}, 1]$
	$\dot{u}_1$	$\mathcal{V}_2^-$	$\frac{\mathcal{V}_1^- + \mathcal{V}_2^-}{2}$	$\frac{\mathcal{V}_1^- - \mathcal{V}_2^-}{2} + \mathcal{V}_2^- \mathrm{e}^{-\eta(\tau-\omega_{21}+\xi_1-1)}$
Bar 2	ξ_2	$[-\omega_{21}, \omega_{21}-\tau]$	$[\omega_{21}-\tau, 0]$	
	$\dot{u}_2$	$\frac{\mathcal{V}_1^- - \mathcal{V}_2^-}{2} + \mathcal{V}_2^- \mathrm{e}^{-\eta(\tau+\xi_2)}$	$\mathcal{V}_2^- \mathrm{e}^{-\eta(\tau+\xi_2)} + (\mathcal{V}_1^- - \mathcal{V}_2^-)\mathrm{e}^{-\eta(\tau-\omega_{21}+\xi_2)}$	
$t \in (\omega_{21}/2+1, 2]$				
Bar 1	ξ_1	$[0, 1-\tau+\omega_{21}]$	$[1-\tau+\omega_{21}, \tau-1]$	$[\tau-1, 1]$
	$\dot{u}_1$	$\mathcal{V}_2^-$	$\mathcal{V}_2^- \mathrm{e}^{-\eta(\tau-\omega_{21}+\xi_1-1)}$	$\frac{\mathcal{V}_1^- - \mathcal{V}_2^-}{2} + \mathcal{V}_2^- \mathrm{e}^{-\eta(\tau-\omega_{21}+\xi_1-1)}$
Bar 2	ξ_2	$[-\omega_{21}, \omega_{21}-\tau]$	$[\omega_{21}-\tau, 0]$	
	$\dot{u}_2$	$\frac{\mathcal{V}_1^- - \mathcal{V}_2^-}{2} + \mathcal{V}_2^- \mathrm{e}^{-\eta(\tau+\xi_2)}$	$\mathcal{V}_2^- \mathrm{e}^{-\eta(\tau+\xi_2)} + (\mathcal{V}_1^- - \mathcal{V}_2^-)\mathrm{e}^{-\eta(\tau-\omega_{21}+\xi_2)}$	

Table B.1: Velocity fields for $\tau \in (0, 2]$, assuming $\tau_C = 2$.

It reads

$$\mathcal{V}_1^+ = \mathcal{V}_1^- \left(1 - \frac{\tau_C}{2}\right) + \mathcal{V}_2^- \left(\omega_{21} - \frac{\tau_C}{2} + \frac{1 - \mathrm{e}^{-\eta(\tau_C - \omega_{21})}}{\eta}\right), \tag{B.42}$$

$$\begin{aligned}\mathcal{V}_2^+ = {} & \frac{\mathcal{V}_1^-}{\omega_{21}} \left(\omega_{21} - \frac{\tau_C}{2} + \frac{1 - \mathrm{e}^{-\eta(\tau_C - \omega_{21})}}{\eta}\right) \\ & + \frac{\mathcal{V}_2^-}{\omega_{21}} \left(\frac{\tau_C}{2} - \omega_{21} + \frac{2e^{-\eta(\tau_C - \omega_{21})} - e^{-\eta\tau_C} - 1}{\eta}\right).\end{aligned} \tag{B.43}$$

The post-contact velocities depend on (i) the pre-contact velocities, (ii) the bar length ratio, and (iii) the stiffness parameter η.

The proposed reset map is dissipative and alters the linear momentum of the rigid body piston/bit system. The former results from the averaging procedure. The dissipative property can be formally proved by an argument similar to that showing the positiveness of the variance of a random variable; indeed, for a single bar, the difference between the kinetic energy calculated from the velocity field and that calculated from the averaged velocity field is given by

$$\begin{aligned}\frac{1}{2}\int_0^L \dot{\mathcal{U}}^2(\xi,\tau)\,\mathrm{d}\xi - \frac{1}{2L}\left(\int_0^L \dot{\mathcal{U}}(\xi,\tau)\,\mathrm{d}x\right)^2 & \\ = \frac{1}{2}\int_0^L \left(\dot{\mathcal{U}}(\xi,\tau) - \frac{1}{L}\int_0^L \dot{\mathcal{U}}(\sigma,\tau)\,\mathrm{d}\sigma\right)^2 \mathrm{d}\xi & \\ \geq 0 & \end{aligned} \tag{B.44}$$

and positive; the same reasoning extends to the piston/bit system that comprises two bars by addition. The application of the reset map thus dissipates a finite amount of energy instantaneously; this can be interpreted as the instantaneous dissipation of the strain and kinetic energies associated with the oscillatory modes of the rods, considered free, at the opening of the contact interface. The alteration of the system linear momentum is equal to the opposite of the impulse realized by the elastic support force

$$\begin{aligned}I_\eta &= \eta \int_0^{\tau_C} \mathcal{U}_2(0,\tau)\,\mathrm{d}\tau, \\ &= \mathcal{V}_1^- \left(\tau_C - \omega_{21} + \frac{\mathrm{e}^{-\eta(\tau_C - \omega_{21})} - 1}{\eta}\right) + \mathcal{V}_2^- \left(\omega_{21} + \frac{\mathrm{e}^{-\eta\tau_C}\left(1 - \mathrm{e}^{\eta\omega_{21}}\right)}{\eta}\right).\end{aligned} \tag{B.45}$$

Contrary to the loss of kinetic energy, which can be shown to include a term independent of η, the impulse of the support force vanishes linearly with η. Thus, the linear momentum of the piston/bit system is conserved by the reset map for $\eta = 0$ and is negligibly affected when $\eta \ll 1$. Figures B.4 and B.5 illustrate the relative variation of kinetic energy

$$\Delta_r \mathsf{KE} = \frac{\left(\mathcal{V}_1^+\right)^2 + \omega_{21}\left(\mathcal{V}_2^+\right)^2}{\left(\mathcal{V}_1^-\right)^2 + \omega_{21}\left(\mathcal{V}_2^-\right)^2} - 1, \tag{B.46}$$

and the impulse of the support force, associated with the representation of the contact phase by the reset map, for $\eta = 0$ and $\eta = 10^{-1}$. They confirm the dissipative character of the reset map, as well as the possibility of a limited positive or negative alteration of the system momentum.

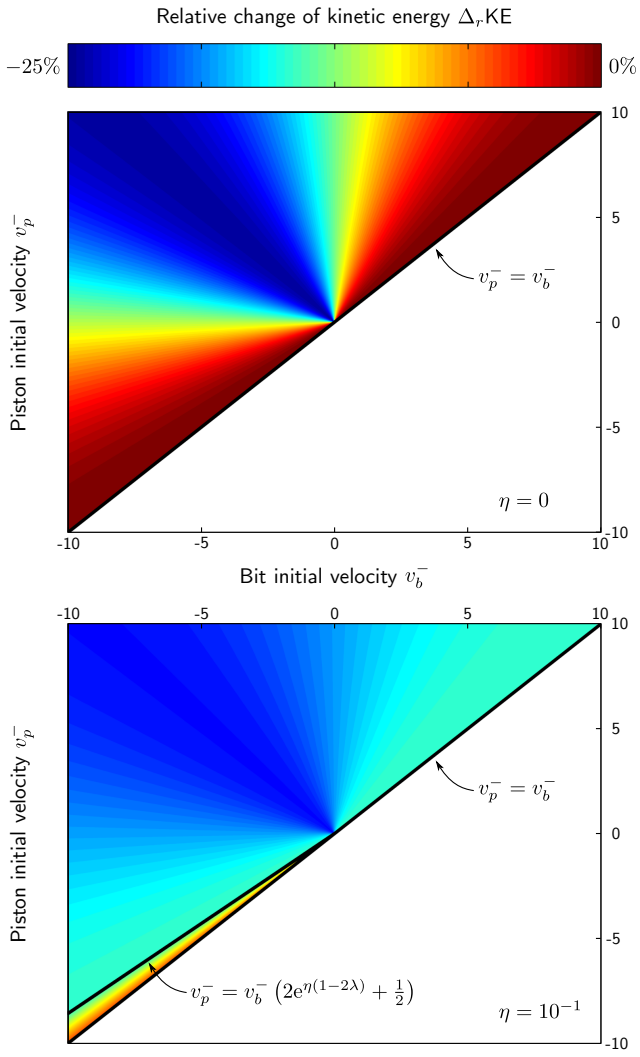

Figure B.4: Relative variation of kinetic energy over the contact phase Δ_rKE, for $\eta = 0$ (top) and $\eta = 10^{-1}$ (bottom).

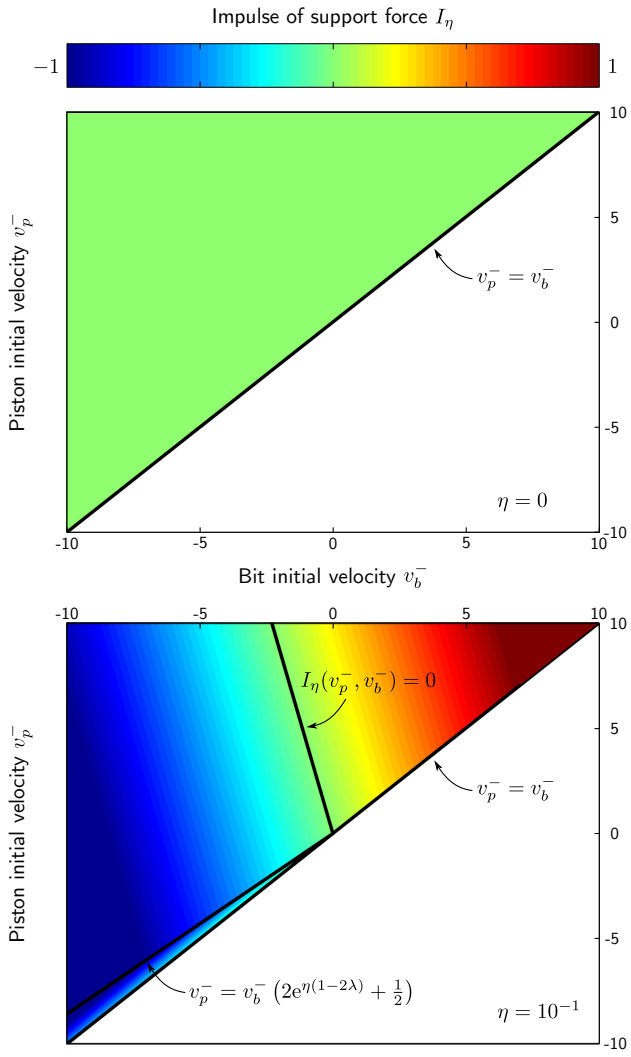

Figure B.5: Impulse of the elastic support force I_η, for $\eta = 0$ (top) and $\eta = 10^{-1}$ (bottom).

Appendix C

Derivation of the DE^3 scheme

The BoTr scheme was originally proposed as a nonlinear formulation for flexible multibody problems [78, 123]. When applied to the model problem of linear structural dynamics

$$\mathbf{M}\dot{\mathbf{v}} + \mathbf{C}\mathbf{v} + \mathbf{K}\mathbf{u} = \mathbf{f}, \qquad\qquad \dot{\mathbf{u}} = \mathbf{v}, \tag{C.1}$$

with the usual notation and positiveness assumptions on the mass, damping and stiffness matrices, it takes the form of a four-level scheme [37, 71]. It reads

$$\begin{aligned}
&\begin{pmatrix} \frac{1}{2}\mathbf{K} & \frac{1}{h}\mathbf{M}+\frac{1}{2}\mathbf{C} & \frac{1}{2}\mathbf{K} & \frac{1}{2}\mathbf{C} \\ \mathbf{I} & -\frac{h}{2}\mathbf{I} & \mathbf{0} & -\frac{h}{2}\mathbf{I} \\ \mathbf{0} & \frac{h}{6}\mathbf{I} & \mathbf{I} & -\chi\frac{h}{6}\mathbf{I} \\ -\frac{1}{6}\mathbf{K} & -\frac{1}{6}\mathbf{C} & \frac{1}{6}\chi\mathbf{K} & \frac{1}{h}\mathbf{M}+\frac{1}{6}\chi\mathbf{C} \end{pmatrix} \begin{pmatrix} \mathbf{u}_{n+1} \\ \mathbf{v}_{n+1} \\ \mathbf{u}_{n^+} \\ \mathbf{v}_{n^+} \end{pmatrix} \\
&\qquad = \begin{pmatrix} \mathbf{0} & \frac{1}{h}\mathbf{M} \\ \mathbf{I} & \mathbf{0} \\ \mathbf{I} & (1-\chi)\frac{h}{6}\mathbf{I} \\ \frac{\chi-1}{6}\mathbf{K} & \frac{1}{h}\mathbf{M}+\frac{\chi-1}{6}\mathbf{C} \end{pmatrix} \begin{pmatrix} \mathbf{u}_n \\ \mathbf{v}_n \end{pmatrix} + \begin{pmatrix} \frac{1}{h}\mathbf{f}_1 \\ \mathbf{0} \\ \mathbf{0} \\ \frac{2}{h^2}\left(t_{n+1/2}\mathbf{f}_1 - \mathbf{f}_2\right) \end{pmatrix},
\end{aligned} \tag{C.2}$$

where subscripts $n, n+1$ indicate that the variables are evaluated at times t_n, t_{n+1}, and subscripts n^+ indicate variables evaluated at $t_n^+ := \lim_{\epsilon\downarrow 0} t_n + \epsilon$. Thus, in the spirit of discontinuous Galerkin methods, discontinuities of the state variables are allowed at each timestep. Matrices $\mathbf{0}, \mathbf{I} \in \mathbb{R}^{d\times d}$ represent the zero and identity matrices and $\mathbf{f}_1 := \int_{t_n}^{t_{n+1}} \mathbf{f}(t)\,\mathrm{d}t$, $\mathbf{f}_2 := \int_{t_n}^{t_{n+1}} t\mathbf{f}(t)\,\mathrm{d}t$ are the first- and second-order time-force moments;

these are to be evaluated with a minimum of third degree exactness to ensure the minimum third-order accuracy of the scheme. Time $t_{n+1/2} := (t_n + t_{n+1})/2$ corresponds to the midstep time and parameter $\chi \in [0, 1]$ can be related to ρ_∞, the spectral radius of the amplification matrix at infinite frequency for an undamped scalar oscillator, via

$$\chi = \frac{1 - \rho_\infty}{1 + \rho_\infty}. \tag{C.3}$$

Following algebraic manipulations of the scheme update equation (C.2), the variation of the mechanical energy over a timestep can be established. Defining the operators of variation and averaging over a timestep as $\Delta x := x_{n+1} - x_n$ and $\bar{x} := (x_{n+1} + x_n)/2$, and the jump discontinuity operator as $[\![x_n]\!] := x_{n^+} - x_n$, it is given by

$$\begin{aligned} \Delta E &:= \Delta \mathbf{v}^T \mathbf{M} \bar{\mathbf{v}} + \Delta \mathbf{u}^T \mathbf{K} \bar{\mathbf{u}}, \\ &= \frac{1}{h} \Delta \mathbf{u}^T \mathbf{f}_1 + \frac{6}{h^2} [\![\mathbf{u}_n]\!]^T \left(t_{n+1/2} \mathbf{f}_1 - \mathbf{f}_2 \right) - \frac{1}{h} \Delta \mathbf{u}^T \mathbf{C} \Delta \mathbf{u} \\ &- \frac{\chi}{2h} [\![\mathbf{u}_n]\!]^T \mathbf{K} [\![\mathbf{u}_n]\!] - \frac{3}{h} [\![\mathbf{u}_n]\!]^T \mathbf{C} [\![\mathbf{u}_n]\!] - \frac{\chi}{2h} [\![\mathbf{v}_n]\!]^T \mathbf{M} [\![\mathbf{v}_n]\!]. \end{aligned} \tag{C.4}$$

When the algorithmic parameter is set to zero, $\chi = 0$, the variation of mechanical energy over a timestep reduces to

$$\Delta E := \Delta \mathbf{u}^T \mathbf{f}_1 - \frac{1}{h} \Delta \mathbf{v}^T (t_{n+1/2} \mathbf{f}_1 - \mathbf{f}_2) - \frac{1}{h} \Delta \mathbf{u}^T \mathbf{C} \Delta \mathbf{u} - \frac{h}{12} \Delta \mathbf{v}^T \mathbf{C} \Delta \mathbf{v}. \tag{C.5}$$

This balance equation expresses the algorithmic conservation of the system mechanical energy and, thus, the integration scheme is numerically conservative for $\chi = 0$.

State variables at t_{n^+} are of little interest in structural dynamics applications. As they appear as variables internal to the update formulas, they can be eliminated and the scheme reduced to a two-level formulation. Not only does this reduce the dimension of the discrete problem by a factor two but it also transforms a non-symmetric formulation into a symmetric one. This can be expected to contribute to a reduction of the computational burden required to solve the update equation, even though the sparsity of the algebraic system is decreased by the reduction.

The first step towards the reduction of the scheme to its two-level equivalent form is the rewriting of the update equation in the partitioned form

$$\begin{pmatrix} \mathbf{H}_0^A & \mathbf{H}_0^B \\ \mathbf{H}_0^C & \mathbf{H}_0^D \end{pmatrix} \begin{pmatrix} \mathbf{x}_{n+1} \\ \mathbf{x}_{n^+} \end{pmatrix} = \begin{pmatrix} \mathbf{H}_1^A \\ \mathbf{H}_1^C \end{pmatrix} \mathbf{x}_n + \begin{pmatrix} \boldsymbol{\ell}_n^{n+1,A} \\ \boldsymbol{\ell}_n^{n+1,C} \end{pmatrix}, \tag{C.6}$$

with state (column) vector $\mathbf{x}_n := [\mathbf{u}_n\,;\,\mathbf{v}_n]$. By static condensation, it is readily established that

$$\begin{aligned}\left(\mathbf{H}_0^A - \mathbf{H}_0^B\left(\mathbf{H}_0^D\right)^{-1}\mathbf{H}_0^C\right)\mathbf{x}_{n+1} = \left(\mathbf{H}_1^A - \mathbf{H}_0^B\left(\mathbf{H}_0^D\right)^{-1}\mathbf{H}_1^C\right)\mathbf{x}_n \\ + \boldsymbol{\ell}_n^{n+1,A} - \mathbf{H}_0^B\left(\mathbf{H}_0^D\right)^{-1}\boldsymbol{\ell}_n^{n+1,C}.\end{aligned} \tag{C.7}$$

Given the assumptions on the system matrices $\mathbf{M}, \mathbf{C}, \mathbf{K}$, matrix $\mathbf{H}_0^D$ is regular ($\left|\mathbf{H}_0^D\right| \neq 0$), and the condensed system is well defined. The condensed iteration matrices and vector are then identified as

$$\begin{aligned}\widehat{\mathbf{H}}_0 &= \mathbf{H}_0^A - \mathbf{H}_0^B\left(\mathbf{H}_0^D\right)^{-1}\mathbf{H}_0^C,\\ \widehat{\mathbf{H}}_1 &= \mathbf{H}_1^A - \mathbf{H}_0^B\left(\mathbf{H}_0^D\right)^{-1}\mathbf{H}_1^C,\\ \widehat{\boldsymbol{\ell}}_n^{n+1} &= \boldsymbol{\ell}_n^{n+1,A} - \mathbf{H}_0^B\left(\mathbf{H}_0^D\right)^{-1}\boldsymbol{\ell}_n^{n+1,C}.\end{aligned} \tag{C.8}$$

The second step towards the reformulation is the calculation of $\left(\mathbf{H}_0^D\right)^{-1}$ and the definition of the condensed iteration matrices and vector. To that end, we use the matrix block inversion formula

$$\mathbf{S}^{-1} = \begin{pmatrix}\mathbf{A} & \mathbf{B}\\ \mathbf{C} & \mathbf{D}\end{pmatrix}^{-1} = \begin{pmatrix}\mathbf{A}^{-1} + \mathbf{A}^{-1}\mathbf{B}\left(\mathbf{S}\backslash\mathbf{A}\right)\mathbf{C}\mathbf{A}^{-1} & -\mathbf{A}^{-1}\mathbf{B}\left(\mathbf{S}\backslash\mathbf{A}\right)\\ -\left(\mathbf{S}\backslash\mathbf{A}\right)^{-1}\mathbf{C}\mathbf{A}^{-1} & \left(\mathbf{S}\backslash\mathbf{A}\right)^{-1}\end{pmatrix}, \tag{C.9}$$

where $\left(\mathbf{S}\backslash\mathbf{A}\right) = \mathbf{D} - \mathbf{C}\mathbf{A}^{-1}\mathbf{B}$ denotes the Schur complement of the partitioned matrix $\mathbf{S}$ with respect to $\mathbf{A}$. Writing the two-level update equation under the partitioned form

$$\begin{pmatrix}\widehat{\mathbf{H}}_0^{\mathbf{uu}} & \widehat{\mathbf{H}}_0^{\mathbf{uv}}\\ \widehat{\mathbf{H}}_0^{\mathbf{vu}} & \widehat{\mathbf{H}}_0^{\mathbf{vv}}\end{pmatrix}\begin{pmatrix}\mathbf{u}_{n+1}\\ \mathbf{v}_{n+1}\end{pmatrix} = \begin{pmatrix}\widehat{\mathbf{H}}_1^{\mathbf{uu}} & \widehat{\mathbf{H}}_1^{\mathbf{uv}}\\ \widehat{\mathbf{H}}_1^{\mathbf{vu}} & \widehat{\mathbf{H}}_1^{\mathbf{vv}}\end{pmatrix}\begin{pmatrix}\mathbf{u}_n\\ \mathbf{v}_n\end{pmatrix} + \begin{pmatrix}\widehat{\boldsymbol{\ell}}_n^{n+1,\mathbf{u}}\\ \widehat{\boldsymbol{\ell}}_n^{n+1,\mathbf{v}}\end{pmatrix}, \tag{C.10}$$

its entries can be expressed as

$$\begin{aligned}\widehat{\mathbf{H}}_0^{\mathbf{uu}} &= \frac{1}{2}\mathbf{K} + \left(\frac{\chi h}{72}\mathbf{K} + \frac{1}{12}\mathbf{C}\right)\left(\mathbf{S}\backslash\mathbf{A}\right)^{-1}\mathbf{K},\\ \widehat{\mathbf{H}}_0^{\mathbf{uv}} &= \frac{1}{h}\mathbf{M} + \frac{1}{2}\mathbf{C} - \frac{h}{12}\mathbf{K} + \frac{\chi^2 h^2}{432}\mathbf{K}\left(\mathbf{S}\backslash\mathbf{A}\right)^{-1}\mathbf{K}\\ &\quad + \frac{\chi h}{72}\left(\mathbf{C}\left(\mathbf{S}\backslash\mathbf{A}\right)^{-1}\mathbf{K} + \mathbf{K}\left(\mathbf{S}\backslash\mathbf{A}\right)^{-1}\mathbf{C}\right) + \frac{1}{12}\mathbf{C}\left(\mathbf{S}\backslash\mathbf{A}\right)^{-1}\mathbf{C},\\ \widehat{\mathbf{H}}_0^{\mathbf{vu}} &= \mathbf{I} - \frac{h}{12}\left(\mathbf{S}\backslash\mathbf{A}\right)^{-1}\mathbf{K},\\ \widehat{\mathbf{H}}_0^{\mathbf{vv}} &= -\frac{h}{2}\mathbf{I} - \frac{\chi h^2}{72}\left(\mathbf{S}\backslash\mathbf{A}\right)^{-1}\mathbf{K} - \frac{h}{12}\left(\mathbf{S}\backslash\mathbf{A}\right)^{-1}\mathbf{C},\end{aligned} \tag{C.11}$$

$$
\begin{aligned}
\widehat{\mathbf{H}}_1^{\mathbf{uu}} &= -\frac{1}{2}\mathbf{K} + \frac{\chi h}{72}\mathbf{K}\left(\mathbf{S}\backslash\mathbf{A}\right)^{-1}\mathbf{K} + \frac{1}{12}\mathbf{C}\left(\mathbf{S}\backslash\mathbf{A}\right)^{-1}\mathbf{K},\\
\widehat{\mathbf{H}}_1^{\mathbf{uv}} &= \frac{1}{h}\mathbf{M} - \frac{1}{2}\mathbf{C} - \frac{h}{12}\mathbf{K} + \frac{\chi^2 h^2}{432}\mathbf{K}\left(\mathbf{S}\backslash\mathbf{A}\right)^{-1}\mathbf{K}\\
&\quad + \frac{\chi h}{72}\left(\mathbf{C}\left(\mathbf{S}\backslash\mathbf{A}\right)^{-1}\mathbf{K} + \mathbf{K}\left(\mathbf{S}\backslash\mathbf{A}\right)^{-1}\mathbf{C}\right) + \frac{1}{12}\mathbf{C}\left(\mathbf{S}\backslash\mathbf{A}\right)^{-1}\mathbf{C},\\
\widehat{\mathbf{H}}_1^{\mathbf{vu}} &= \mathbf{I} - \frac{h}{12}\left(\mathbf{S}\backslash\mathbf{A}\right)^{-1}\mathbf{K},\\
\widehat{\mathbf{H}}_1^{\mathbf{vv}} &= \frac{h}{2}\mathbf{I} - \left(\mathbf{S}\backslash\mathbf{A}\right)^{-1}\left(\frac{h}{12}\mathbf{C} + \frac{\chi h^2}{72}\mathbf{K}\right),\\
\widehat{\boldsymbol{\ell}}_n^{n+1,\mathbf{u}} &= \frac{1}{h}\mathbf{I}_1 - \left(\frac{\chi}{6h}\mathbf{K} + \frac{1}{h^2}\mathbf{C}\right)\left(\mathbf{S}\backslash\mathbf{A}\right)^{-1}\left(t_{n+1/2}\mathbf{f}_1 - \mathbf{f}_2\right),\\
\widehat{\boldsymbol{\ell}}_n^{n+1,\mathbf{v}} &= \frac{1}{h}\left(\mathbf{S}\backslash\mathbf{A}\right)^{-1}\left(t_{n+1/2}\mathbf{f}_1 - \mathbf{f}_2\right),
\end{aligned}
\tag{C.12}
$$

where the Schur complement of $\mathbf{H}_0^D$ is given by $\mathbf{S}\backslash\mathbf{A} := \frac{1}{h}\mathbf{M} + \frac{\chi}{6}\mathbf{C} + \frac{\chi^2 h}{36}\mathbf{K}$. Simplifications then follow by left-multiplication of equation (C.10) by the conditioning matrix

$$
\mathbf{Q} = \begin{pmatrix} h\mathbf{I} & \frac{\chi h}{6}\mathbf{K} + \mathbf{C} \\ -\frac{\chi h^2}{6}\mathbf{I} & \mathbf{M} \end{pmatrix}. \tag{C.13}
$$

Completing all algebra, the DE^3 scheme that is the equivalent two-level form of the BoTr scheme is obtained. It is defined by iteration matrices and load vector

$$
\begin{aligned}
\mathbf{H}_0 &:= \begin{pmatrix} \mathbf{C} + \frac{\chi+3}{6}h\mathbf{K} & \mathbf{M} - \frac{1+\chi}{12}h^2\mathbf{K} \\ \mathbf{M} - \frac{1+\chi}{12}h^2\mathbf{K} & -\left(\frac{\chi}{6} + \frac{1}{2}\right)h\mathbf{M} - \frac{1+\chi}{12}h^2\mathbf{C} \end{pmatrix},\\
\mathbf{H}_1 &:= \begin{pmatrix} \mathbf{C} + \frac{\chi-3}{6}h\mathbf{K} & \mathbf{M} - \frac{1-\chi}{12}h^2\mathbf{K} \\ \mathbf{M} - \frac{1-\chi}{12}h^2\mathbf{K} & -\left(\frac{\chi}{6} - \frac{1}{2}\right)h\mathbf{M} - \frac{1-\chi}{12}h^2\mathbf{C} \end{pmatrix},\\
\boldsymbol{\ell}_n^{n+1} &:= \begin{pmatrix} \mathbf{f}_1 \\ \left(t_{n+1/2} - \frac{\chi}{6}h\right)\mathbf{f}_1 - \mathbf{f}_2 \end{pmatrix},
\end{aligned}
$$

that correspond to state vector $\mathbf{x}_n := [\mathbf{u}_n\,;\,\mathbf{v}_n]$.

Appendix D

Newton's cradle: analytical solution

Let a local axis system be attached to each bar, as shown in Figure 4.5, and let the displacements be measured with respect to the bar initial positions. Denoting by $\xi_i \in [0,1]$ the abscissa along the bar and by $\tau \in \mathbb{R}^+$ the time variable, the motion of bar i is ruled by

$$\dot{\mathcal{V}}_i(\xi_i,\tau) = \mathcal{U}_i''(\xi_i,\tau), \qquad \mathcal{V}_i(\xi_i,\tau) = \dot{\mathcal{U}}_i(\xi_i,\tau), \tag{D.1}$$

with $i \in \{1;\cdots;N\}$ and N the number of bars. In the above equation, an overhead dot denotes differentiation with respect to the time τ and a prime symbol to the space coordinate ξ_i. The initial conditions read $\mathcal{U}_i(\xi_i,0) = 0$, $i \in \{1;\ldots;N\}$, $\mathcal{V}_1(\xi_1,0) = \mathcal{V}_0$, $\mathcal{V}_i(\xi_i,0) = 0$, $i \in \{2;\ldots;N\}$, and, for each bar, the boundary conditions are given by the complementarity conditions that enforce the contact interactions at the ends of each bar. Given the specifics of the problem, the handling of boundary conditions simplifies to the consideration of three configurations, namely: free flight, bar/bar contact and bar/wall contact.

During free flight, the bar is unconstrained and free to move axially. In the absence of external forces, the bar is thus at rest, in stationary motion or freely vibrating. Given the problem characteristics, the latter possibility can be discarded.

During bar/bar contact, the conjugated ends of the contacting bars are constrained

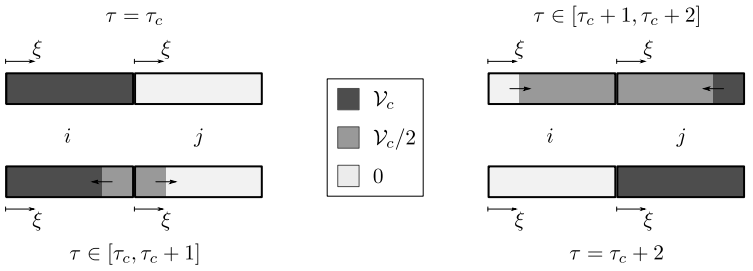

Figure D.1: Velocity distribution during a phase of bar/bar contact. At $\tau = \tau_c$, the left bar impacts with uniform velocity $\mathcal{V}_c$ the right one that is at rest. The persistent contact phase lasts for 2 units of time given the problem normalization; that is, the time taken for the wave front to travel forth and back the bars. After completion of the contact phase, both bars are free of vibrations and behave like rigid bodies; the impacted one has uniform velocity $\mathcal{V}_c$ and the impacting one is at rest.

by force equilibrium and the equality of the velocity at the contacting surfaces (condition of non-interpenetration), and unconstrained at their free ends. Given the identical nature of the bars and the specifics of the initial conditions, we can restrict our consideration to the case of the longitudinal impact of one bar i having uniform velocity $\mathcal{V}_c$ on another one j that is at rest. This impact configuration is treated in detail by Graff [53, Sec. 2.4] by use of d'Alembert's solution to the wave equation. Upon closure of the contact interface, a wave front propagates from the contact surface towards the free ends of the contacting bars. It propagates information as to the bar velocity which is discontinuous across it; see Figure D.1. This propagation lasts for 2 units of time; that is, the time necessary for a round trip of the wave front inside the bars. The contact phase can be split in two. During its first half, $\tau \in [\tau_c, \tau_c + 1]$, the velocity in each bar is given by

$$\mathcal{V}_i(\xi_i, \tau) = \mathcal{V}_c \begin{cases} 1 & \tau - \tau_c < 1 - \xi_i, \\ \frac{1}{2} & \tau - \tau_c \geq 1 - \xi_i, \end{cases} \qquad \mathcal{V}_j(\xi_j, \tau) = \mathcal{V}_c \begin{cases} \frac{1}{2} & \tau - \tau_c > \xi_j, \\ 0 & \tau - \tau_c \leq \xi_j. \end{cases} \tag{D.2}$$

During its second half, $\tau \in [\tau_c + 1, \tau_c + 2]$, it is given by

$$\mathcal{V}_i(\xi_i, \tau) = \mathcal{V}_c \begin{cases} 0 & \tau - \tau_c > 1 + \xi_i, \\ \frac{1}{2} & \tau - \tau_c \leq 1 + \xi_i, \end{cases} \qquad \mathcal{V}_j(\xi_j, \tau) = \mathcal{V}_c \begin{cases} \frac{1}{2} & \tau - \tau_c < 2 - \xi_j, \\ 1 & \tau - \tau_c \geq 2 - \xi_j. \end{cases} \tag{D.3}$$

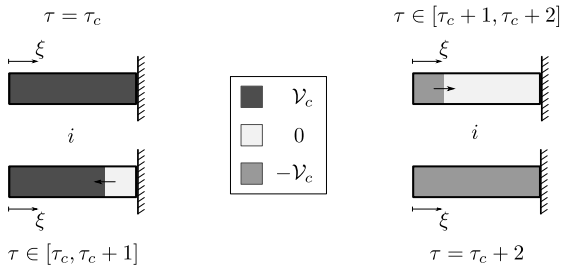

Figure D.2: Velocity distribution during a phase of bar/wall contact. At $\tau = \tau_c$, the bar impacts a rigid wall with uniform velocity $\mathcal{V}_c$. The persistent contact phase lasts for 2 units of time; that is, the time taken for the wave front to travel forth and back the impacting bar. After completion of the contact phase, the impacting bar rebounds off the wall with uniform opposite velocity $-\mathcal{V}_c$.

After completion of the contact phase, the impacting bar is thus at rest and the impacted one has uniform velocity $\mathcal{V}_c$, as a result of perfect momentum transfer. Both are free of vibrations and deformations. Also, each bar has achieved a displacement $\mathcal{V}_C$ over the duration of the contact phase.

During bar/wall contact, the situation is similar to that during bar/bar contact except that the impacting bar experiences a velocity reversal. The four phases of the contact sequence are depicted in Figure D.2. At time $\tau = \tau_c + 1$, the bar is in uniform compression state with strain $\mathcal{U}_i' = -\mathcal{V}_c$. The contact phase completes after 2 units of time. Over the duration of persistent contact, the velocity field is defined by

$$\begin{aligned}
\mathcal{V}_i(\xi_i, \tau) = \quad & \mathcal{V}_c \begin{cases} 1 & \tau - \tau_c < 1 - \xi_i, \\ 0 & \tau - \tau_c \geq 1 - \xi_i, \end{cases} && \tau \in [\tau_c, \tau_c + 1]\,, \\
\mathcal{V}_i(\xi_i, \tau) = & -\mathcal{V}_c \begin{cases} 0 & \tau - \tau_c > 1 + \xi_i, \\ 1 & \tau - \tau_c \leq 1 + \xi_i, \end{cases} && \tau \in [\tau_c + 1, \tau_c + 2]\,.
\end{aligned} \tag{D.4}$$

Given the chain nature of the system, the specificity of the initial conditions, and the system behavior during interaction phases, the system global response corresponds to a sequence of free flight, bar/bar and bar/wall contact phases. Furthermore, motion will be periodic and simultaneous contact phases at different interfaces are not expected for $\mathcal{G}_1, \mathcal{G}_2 > \mathcal{V}_0$, for, in this case, each persistent contact phase completes before the next begins.

The computation of the system motion requires that of contact closure and opening times. These can be established by composition of motion phases. For $N > 2$, bars with $i \in \{2; \ldots; N-1\}$ experience four contact phases with their immediate neighbors over a period of motion, two in the positive direction, two in the negative direction. These occur at times that, modulo the motion period, read

$$\begin{aligned}
&i-1/i : \tau_{c,1} = (i-1)\frac{\mathcal{G}_1}{\mathcal{V}_0} + (i-2),\\
&i/i+1 : \tau_{c,2} = \tau_{c,1} + \frac{\mathcal{G}_1}{\mathcal{V}_0} + 1,\\
&i+1/i : \tau_{c,3} = \tau_{c,2} + 2\left(1 + \frac{\mathcal{G}_2}{\mathcal{V}_0}\right) + 2\left(N-i-1\right)\left(1 + \frac{\mathcal{G}_1}{\mathcal{V}_0}\right),\\
&i/i-1 : \tau_{c,4} = \tau_{c,3} + \frac{\mathcal{G}_1}{\mathcal{V}_0} + 1.
\end{aligned} \tag{D.5}$$

Bars 1 and N experience only three contact phases over a period. Modulo the motion period, these take place at times

$$\begin{aligned}
1/2 : \tau_{c,1} &= \frac{\mathcal{G}_1}{\mathcal{V}_0},\\
2/1 : \tau_{c,2} &= (2N-3)\frac{\mathcal{G}_1}{\mathcal{V}_0} + (2N-2) + 2\frac{\mathcal{G}_2}{\mathcal{V}_0},\\
1/\text{wall} : \tau_{c,3} &= \tau_{c,2} + 2 + \frac{\mathcal{G}_1}{\mathcal{V}_0} + \frac{\mathcal{G}_2}{\mathcal{V}_0},\\
N-1/N : \tau_{c,1} &= (N-1)\frac{\mathcal{G}_1}{\mathcal{V}_0} + (N-2),\\
N/\text{wall} : \tau_{c,2} &= \tau_{c,1} + \frac{\mathcal{G}_2}{\mathcal{V}_0} + 1,\\
N/N-1 : \tau_{c,3} &= \tau_{c,2} + \frac{\mathcal{G}_2}{\mathcal{V}_0} + 2.
\end{aligned} \tag{D.6}$$

The motion period is readily shown to be

$$T = 4\frac{\mathcal{G}_2}{\mathcal{V}_0} + 2(N-1)\frac{\mathcal{G}_1}{\mathcal{V}_0} + 2(N+1). \tag{D.7}$$

It represents the sum of the durations of free flight motion and wave propagation in the system.

With the knowledge of the times of closure of contact interfaces and that of the velocity field during interaction phases, the velocity field of the system can be constructed and the displacement field obtained by its integration. Space integration of these fields

then yields the average motion of the bars, which can also be constructed from the bar average response during interaction phases. For bar/bar and bar/wall interactions, we have for $\tau \in [\tau_c, \tau_c + 2]$

$$\langle \underline{\mathcal{V}}_i \rangle_\xi (\tau) = \mathcal{V}_c \left(1 - \frac{\tau - \tau_c}{2} \right), \qquad \langle \underline{\mathcal{V}}_j \rangle_\xi (t) = \mathcal{V}_c \frac{\tau - \tau_c}{2}, \tag{D.8}$$

and

$$\langle \underline{\mathcal{V}}_i \rangle_\xi (\tau) = \mathcal{V}_c \left(1 - (\tau - \tau_c) \right), \tag{D.9}$$

for $\tau \in [\tau_c, \tau_c + 2]$. The contact velocity depends on the direction of motion at the initiation of contact, $\mathcal{V}_c = \pm \mathcal{V}_0$. The average displacement is then obtained as

$$\langle \underline{\mathcal{U}}_i \rangle_\xi (\tau) = \mathcal{V}_c (\tau - \tau_c) \left(1 - \frac{\tau - \tau_c}{4} \right), \qquad \langle \underline{\mathcal{U}}_i \rangle_\xi (\tau) = \mathcal{V}_c \frac{(\tau - \tau_c)^2}{4}, \tag{D.10}$$

for $\tau \in [\tau_c, \tau_c + 2]$ and

$$\langle \underline{\mathcal{U}}_i \rangle_\xi (\tau) = \mathcal{V}_c (\tau - \tau_c) \left(1 - \frac{\tau - \tau_c}{2} \right), \tag{D.11}$$

for $\tau \in [\tau_c, \tau_c + 2]$. During free flight phases, a single bar moves with uniform average velocity $\pm \mathcal{V}_0$ while the others are at rest.

Appendix E

Sensitivity to discretization parameters

When differential equations are numerically approximated, it is important to assess the influence of the algorithmic and discretization parameters on the computed response. The analyses of Chapter 4 have shown that the contact stiffness κ_C and proportional damping parameter ζ_K can play a significant influence on the numerical results and must be chosen adequately. In this appendix, we investigate the influence of the discretization parameters on the simulated response of the elastic and rigid two-body models.

E.1 Elastic model

To integrate the elastic model, both space and time discretizations are carried out so that the governing partial differential equations can be transformed into algebraic update equations. An important parameter in wave propagation simulations is the CFL number

$$\text{CFL} := h_t c_0 / h_x \tag{E.1}$$

that relates the spatial and temporal element sizes to the wave propagation speed in the medium, h_x, h_t and c_0, respectively. Typically, it is chosen of order one so that wave fronts propagate by approximately one element over one integration step.

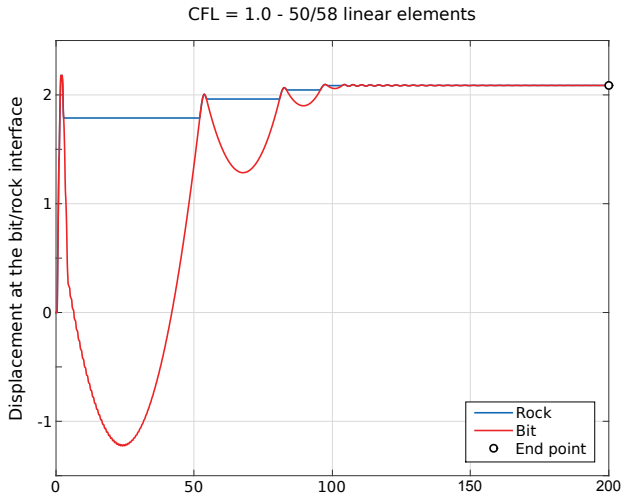

Figure E.1: Displacement response at the bit/rock interface following a percussive activation, for the reference configuration. After several drilling cycles, the bit settles on the rock. The achieved penetration is measured after 200 units of time.

To assess the sensitivity of the numerical simulations, we consider the model response for the reference configuration given in Section 5.1, from generalized free flight initial conditions. The piston initial velocity is set to $\langle {}_1\mathcal{V} \rangle_\xi = 2.5$, which approximately corresponds to 10 m/s. As shown in Figure E.1, after a couple of drilling cycles, the interaction law enters the standstill mode and the bit settles on the rock. After 200 units of time, the bit is close to standing still on the rock. We use the bit penetration at that instant, *i.e.*, the penetration achieved by a single percussive activation, as the reference quantity to assess the mesh sensitivity.

To that end, we consider discretizations corresponding to CFL $\in \{0.5, 1.0, 2.5, 5.0\}$ and $n_p \in \{10, 25, 50, 100, 250\}$, where n_p is the number of linear elements used to uniformly discretize the piston. By the requirement of nearly equal size elements for the piston and bit meshes, the number of elements on the bit is then given by $n_b := \lceil \omega_{21} n_p \rceil$. The contact stiffness and the proportional damping are set in accordance with the results of Section 4.2.4, on the basis of a spatial mesh with $n_p = 50$; that is, $\kappa_C = 100.9$ and $\zeta_K = 0.5$ with $\omega_{cr} = 552.5$. The root-solving tolerances are set to $(\texttt{qTol}, \texttt{tTol}, \texttt{degTol}) = (10^{-6}, 10^{-4}, 10^{-12})$. Given the definition of the CFL number, $h_t \sim h_x^{-1}$ and the timestep decreases as the spatial mesh is refined at constant CFL.

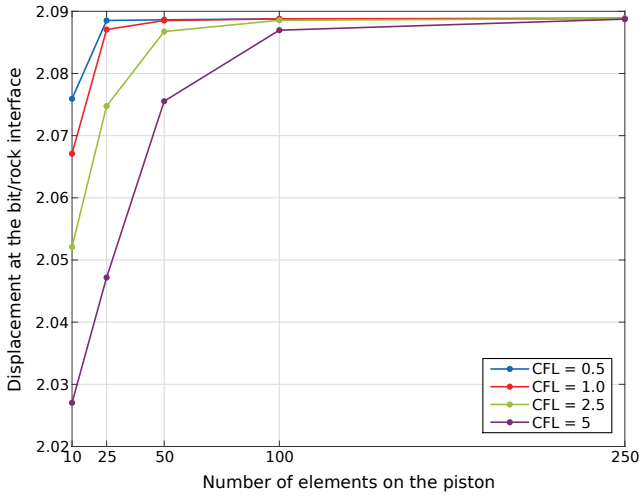

Figure E.2: Influence of the spatial and time discretizations on the penetration resulting from a percussive activation from generalized free flight initial conditions.

The results of the convergence analysis are shown in Figure E.2. It is observed that the smaller the CFL number, the faster the spatial convergence. Also, even for a coarse discretization, the error on the achieved penetration is below 5%. For $n_p = 50$, the error is below 1% at CFL $= 5$. Accordingly, all simulations were performed using CFL $= 5$ and $n_p = 50$.

E.2 Rigid model

In the absence of an error estimate for the DE^3 time integration scheme, the practical approach for timestep selection is to use a constant timestep throughout the simulation [124]. It is common practice in structural dynamics to then select it on the basis of the highest frequency mode to be resolved.

In the rigid model, the piston and the bit experience parabolic motion but during interaction phases where the bit experiences harmonic oscillations. To take advantage of this situation, we set the timestep as a function of the drilling mode. Defining the reference timestep as h_0, the following scaling law is used

$$h_{\{\mathsf{FF},\mathsf{SS}\}} = h_0, \qquad h_{\mathsf{FC}} = \frac{1}{10} h_0, \qquad h_{\mathsf{BC}} = \frac{1}{10\sqrt{\gamma}} h_0. \tag{E.2}$$

It must be noted that, as the motion of the bit and the piston is parabolic during the free flight and standstill modes, the DE^3 scheme exactly integrates their motion; the definition of $h_{\{\mathsf{FF},\mathsf{SS}\}}$ is thus only guided by graphical purposes. Given that the dimensionless formulation has been derived on the basis of timescale T_4, the durations of a forward contact phase and of a backward contact phase are about $\pi/2$ and $\pi/(2\sqrt{\gamma})$ units of time. The above law thus ensures $5\pi/h_0$ computed points along trajectory segments in the forward contact and backward contact modes.

To assess the influence of h_0 on the computed response, we reproduce the analysis conducted for the elastic model. Parameters corresponding to the reference configuration are used, as well as numerically conservative time integration $\rho_\infty = 1$; the root-solving tolerances are set to $(\texttt{qTol}, \texttt{tTol}, \texttt{degTol}) = (10^{-6}, 10^{-4}, 10^{-12})$. The reference trajectory and the results of the convergence analysis are shown in Figure E.3. It is seen that high accuracies are already obtained with $h_0 = 1$. For $h_0 = 10$, the last free flight phase before the bit enters the standstill mode is not represented. This is the consequence of the timestep being larger than the duration of the free flight phase; it is, nonetheless, taken into account in the computation; the error on the achieved penetration is significant. The timestepping strategy is well illustrated by the zoom on the post-activation time range. Given the convergence results, all the simulations of Chapter 5 have been conducted with $h_0 = 1$.

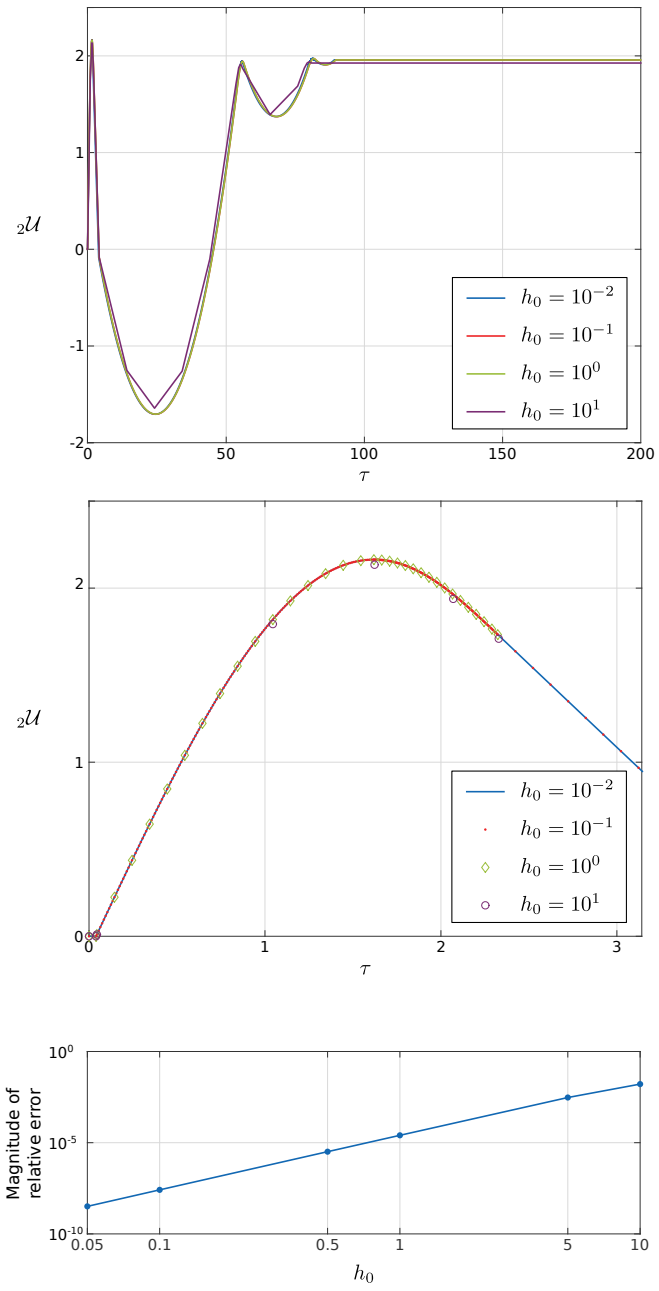

Figure E.3: Influence of timestep scaling h_0 on the bit trajectory and on the achieved end penetration. The error magnitude is calculated with respect to the results obtained for $h_0 = 10^{-2}$.